AN ASSESSMENT OF QUANTIFICATION METHODS IN FATTY TISSUES USING CHEMICAL SHIFT ENCODED MAGNETIC RESONANCE IMAGING

AND

STUDYING PIG BRAIN FUNCTIONAL CONNECTIVITY USING MAGNETIC RESONANCE IMAGING

by

GREGORY ALAN SIMCHICK

(Under the Direction of Qun Zhao)

ABSTRACT

Magnetic resonance imaging (MRI) is a non-invasive medical imaging technique that extends well beyond its visual, qualitative applications. Through the manipulation of quantum mechanical spin, which is the basis for MRI, quantitative information about the intrinsic physical and chemical properties of tissues can be determined. In this dissertation, multiple different MRI techniques are employed in order to estimate various properties of tissues, assess different methodologies of estimation, and discuss practical applications of these techniques. Among the techniques utilized includes: triglyceride composition mapping and quantitative susceptibility mapping (QSM) using chemical shift encoded (CSE-) MRI, functional (f) MRI, and diffusion tensor imaging (DTI). Part 1 of this dissertation focuses on the use of CSE-MRI in fatty tissues to quantify triglyceride composition and liver iron concentration (LIC). Many methodologies for estimating triglyceride composition require an *a priori* fat spectral model; therefore, the effect of using various different fat spectral models on this estimation is explored in Chapter 2. It was observed that the triglyceride composition had a strong dependence on the chosen *a priori* model; however, proton density fat fraction was independent of the chosen model. The primary MR-based methodology for determining LIC is currently the effective transverse spin-spin relaxation time (R2*) mapping, whereas QSM is a newer methodology that may have benefits over R2* mapping. Chapter 3 compares the use of R2* mapping and QSM to quantify LIC in an ex vivo mouse model. QSM proved to be a more robust methodology in this ex vivo study. Part 2 of this dissertation focuses on using fMRI to study pig brain functional connectivity and the disruptions caused by traumatic brain injuries (TBIs). Due to the many similarities between the pig and human brain, the pig serves as a useful large animal model for studying brain connectivity. Chapter 5 establishes six resting-state networks (RSNs) in the pig brain, draws comparisons with the human brain, and uses quantitative DTI measurements to provide support of the validity of these RSNs. Chapter 6 seeks to detect and evaluate disruptions in these RSNs using a TBI pig model. Disruptions were successfully detected in four RSNs and were traced back to affected individual anatomical regions.

INDEX WORDS: Chemical shift encoded MRI, Triglyceride composition, Quantitative susceptibility mapping, Liver iron concentration, Functional MRI, Diffusion tensor imaging, Pig brain, Resting-state networks, Sparse dictionary learning, Independent component analysis, Traumatic brain injury

AN ASSESSMENT OF QUANTIFICATION METHODS IN FATTY TISSUES USING CHEMICAL SHIFT ENCODED MAGNETIC RESONANCE IMAGING

AND

STUDYING PIG BRAIN FUNCTIONAL CONNECTIVITY USING MAGNETIC RESONANCE IMAGING

by

GREGORY ALAN SIMCHICK

BS, University of Pittsburgh, 2014

A Dissertation Submitted to the Graduate Faculty of The University of Georgia in Partial Fulfillment of the Requirements for the Degree

DOCTOR OF PHILOSOPHY

ATHENS, GEORGIA

2020

AN ASSESSMENT OF QUANTIFICATION METHODS IN FATTY TISSUES USING CHEMICAL SHIFT ENCODED MAGNETIC RESONANCE IMAGING

AND

STUDYING PIG BRAIN FUNCTIONAL CONNECTIVITY USING MAGNETIC RESONANCE IMAGING

by

GREGORY ALAN SIMCHICK

Major Professor:	Qun Zhao
Committee:	Heinz-Bernd Schuttler
	Susanne Ullrich
	Jeffrey Urbauer

Electronic Version Approved:

Ron Walcott
Interim Dean of the Graduate School
The University of Georgia
May 2020

ACKNOWLEDGEMENTS

I'd first like to thank my advisor Qun Zhao for always encouraging me to explore new areas in our field, participate in collaborations, and attend scientific conferences. This has helped me develop a diverse and expansive set of skills, learn more than I thought imaginable about the fascinating field of MRI physics, and form countless professional relationships. I'd also like to thank my advisory committee, Heinz-Bernd Schuttler, Susanne Ullrich, and Jeffrey Urbauer, for their continued support throughout my graduate career.

A very special thanks is given to Diego Hernando for his willingness to help improve my understanding of fat-water imaging, as well as provide useful Matlab and C code to assist in many of the estimations performed in this dissertation. The Cornell MRI Research Lab also deserves recognition for their freely available QSM Toolbox, which also assisted in some of the estimations performed in this dissertation.

I also would like to thank all of my collaborators, specifically Amelia Yin, Zhi Liu, and Kelly Scheulin. My work would not be possible if not for their countless hours of animal work. Kim Mason also deserves a multitude of gratitude for helping to develop protocols and collect data, as well as for always making sure the University of Georgia Bio-Imaging Research Center operates smoothly.

Funding for the work presented in this dissertation was provided by NIH grants R01DK099596, R01NS093314, and S10RR023706, and the University of Georgia Office of Research grant GEO00795.

Finally, no amount of appreciation can truly be given to my friends and family for always being there for me through every good and bad moment. Your love means so much.

TABLE OF CONTENTS

CHAPTER

APPENDICES

LIST OF TABLES

Page

LIST OF FIGURES

PART 1

AN ASSESSMENT OF QUANTIFICATION METHODS IN FATTY TISSUES USING CHEMICAL SHIFT ENCODED MAGNETIC RESONANCE IMAGING

Magnetic resonance imaging (MRI) is a non-invasive medical imaging technique that allows for the study of biological tissues at a quantum mechanical level. MRI data provides qualitative, as well as quantitative, information about the intrinsic physical and chemical properties of tissues, such as magnetic susceptibility, the effective spin-spin relaxation rate of interacting proton spins as they return to equilibrium following excitation, and the triglyceride composition of fatty tissues.

Since water is the most abundant molecule in biological lifeforms and tissues, MRI most often focuses on the excitation of protons of hydrogen atoms within water molecules. However, in order to make excitation pulses short to reduce scan times, typical excitation bandwidths cover a wider chemical range and may excite protons in other molecules that have chemical shifts similar to that of water, such as those that make up fatty tissues.

Part 1 of this dissertation will explain how the off-resonance excitations of fat or lipid molecules impact the MR signal, how these effects can be accounted for and utilized, and what quantitative information can be determined within fatty tissues. Chapter 1 provides a brief overview of chemical shift encoded (CSE-) MRI in fatty tissues, as well as a theoretical and mathematical framework for estimating from the CSE-MRI signal the effective spin-spin relaxation rate (R_2^*), triglyceride composition using water-fat separation methods, and magnetic susceptibility using quantitative susceptibility mapping techniques. Chapters 2 and 3 provide evaluation of specific CSE-MRI estimation methods and discuss some practical applications of these methods.

CHAPTER 1

INTRODUCTION AND LITERATURE REVIEW

Chemical Shift Encoded Magnetic Resonance Imaging

Using a MR data collection method known as gradient echo imaging, a typical MR signal containing one chemical species, such as water, will follow an exponential decay governed by

$$S(t) = C\rho e^{-R_2^* t} e^{i2\pi f_B t} \qquad (1.1)$$

where *C* is a scaling factor associated with the magnetization of the system when in equilibrium, ρ is the proton density of the material, R_2^* is the effective spin-spin relaxation rate, f_B is the relative frequency shift from the chosen rotating reference frame that arises due to inhomogeneities in the static magnetic field (typically the rotating reference frame is set to the Larmor frequency of water), and *t* is the time following excitation.

However, in the presence of multiple chemical species, the signal follows a more complex decay governed by

$$S(t) = C(\sum_{m=1}^{M} \rho_m e^{i2\pi f_m t_n} e^{-R_{2,m}^* t}) e^{i2\pi f_B t} \qquad (1.2)$$

where *m* represents a distinct chemical species and $f_m = \gamma B_0 \sigma_m$ is the chemical species' frequency shift relative to the chosen rotating reference frame with γ representing the proton gyromagnetic ratio, B_0 representing the static magnetic field strength, and σ_m representing the relative chemical shift of the *m*th chemical species.

This signal model is a representation of what is known as chemical shift encoded MRI (CSE-MRI). Similar to nuclear magnetic resonance (NMR) spectroscopy, CSE-MRI excites multiple chemical species, opposed to solely exciting the hydrogen atoms found in water, as is the typical case for most biological tissues studied using MRI. The excitation of these additional chemical species, whether intended or not, needs to be considered when attempting to quantify various intrinsic properties related to the tissue, such as R_2^* and magnetic susceptibility. The additional excitation of these chemical species can also be used to study properties related to the chemical species themselves, such as the triglyceride composition in fatty tissues.

In fact, CSE-MRI is most often used for the of study fatty tissues. High field NMR spectroscopy of adipose tissue has shown that the fat spectrum consists of multiple resonance peaks or chemical species [1-3], among which 9 peaks are easily identifiable with their chemical shifts being relatively fixed for all types of fatty tissues (Figure 1.1). Using the Larmor frequency of water as the reference frequency for the rotating reference frame, a signal model for tissues containing both water and fat can be given by

$$S(t) = C(\rho_{\mathrm{W}} e^{-R_{2,\mathrm{W}}^* t} + \rho_{\mathrm{F}} \sum_{m=1}^{M} \alpha_m e^{i2\pi f_m t} e^{-R_{2,m}^* t}) e^{i2\pi f_B t} \qquad (1.3)$$

where ρ_{W} and ρ_{F} are the water and fat proton densities, α_m is the amplitude and f_m is the frequency shift relative to water of the *m*th fat peak, and $\mathrm{R}_{2,\mathrm{W}}^*$ and $\mathrm{R}_{2,m}^*$ are the effective spin-spin relaxation rates of the water resonance peak and *m*th fat resonance peak. Note that this signal model does not include contributions from spin-lattice relaxation (T1-weighting) or initial phase shifts due to eddy currents, both of which may need to be addressed depending on the data acquisition.

However, from this signal model, one may notice that it is possible to estimate multiple different quantities. R_2^* for each chemical species ($R_{2,W}^*$ and $R_{2,m}^*$) can be estimated. Although f_m is fixed, ρ_W, ρ_F, and α_m can all be estimated and relate to the triglyceride composition of the tissue, and it is possible to estimate f_B, which relates to the magnetic susceptibility of the tissue.

Triglyceride Composition Mapping

As discussed above, fatty tissues are composed of 9 different fat resonance peaks or chemical species. Each of these peaks are associated with a specific chemical make-up that was first described by Hamilton et al. [3] (Table 1.1). The relative amplitudes or concentrations of these peaks have been shown to depend upon three intrinsic chemical parameters: 1) the number of double bonds per molecule (*ndb*), 2) the number of methylene-interrupted double bonds per molecule (*nmidb*), and 3) the fatty acid chain length (*cl*). These three chemical parameters, as well as proton density fat fraction (*PDFF*), can all be estimated from the CSE-MRI signal acquired from fatty tissues. Peterson et al. [4] was the first to establish the mathematical model for doing so.

In matrix form, Eq. (1.3) can be written as

$$\boldsymbol{S}_{nx1} = \boldsymbol{D}\boldsymbol{A}\boldsymbol{\rho} \qquad (1.4)$$

where $\boldsymbol{S}$ is the acquired CSE-MRI complex signal at n echo times, $\boldsymbol{D}$ accounts for static field inhomogeneities, $\boldsymbol{A}$ includes the information from Table 1.1 related to the chemical shifts and theoretical amplitudes of the nine fat resonance peaks, as well as accounts for R_2^* decay, and $\boldsymbol{\rho}$ is a density matrix associated with water and fat proton densities and triglyceride parameters. The following mathematical representations of $\boldsymbol{D}$, $\boldsymbol{A}$ and $\boldsymbol{\rho}$ are as follows:

$$\boldsymbol{D}_{nxn} = \begin{bmatrix} e^{i2\pi f_B t_1} & \cdots & 0 \\ \vdots & \ddots & \vdots \\ 0 & \ldots & e^{i2\pi f_B t_n} \end{bmatrix},$$

$$\boldsymbol{A}_{nx5} = \begin{bmatrix} e^{-R_{2,\mathrm{W}}^{*}t_1} & a(t_1) & b(t_1) & c(t_1) & d(t_1) \\ \vdots & \vdots & \vdots & \vdots & \vdots \\ e^{-R_{2,\mathrm{W}}^{*}t_n} & a(t_n) & b(t_n) & c(t_n) & d(t_n) \end{bmatrix},$$

$$\boldsymbol{\rho}_{5x1} = C\begin{bmatrix} \rho_{\mathrm{W}} \\ \rho_{\mathrm{F}} \cdot f \\ \rho_{\mathrm{F}} \cdot f \cdot ndb \\ \rho_{\mathrm{F}} \cdot f \cdot nmidb \\ \rho_{\mathrm{F}} \cdot f \cdot cl \end{bmatrix}$$

where $f = 1/(C\sum_{m=1}^{M}\alpha_m)$ is a normalization factor related to the MRI scaling factor and the sum of the amplitudes of all fat peaks and

$$a = E_2 + 4E_3 + 6E_5 + 6E_6 - 24E_8 + 9E_9,$$

$$b = 2E_1 + 4E_6 - 8E_8,$$

$$c = 2E_4 - 4E_6 + 2E_8,$$

$$d = 6E_8.$$

with $E_m = e^{(i2\pi f_m - R_{2,m}^{*})t}$. Here *a* is associated with the number of single bonded hydrogen atoms, *b* with *ndb*, *c* with *nmidb,* and *d* with *cl*. These equations are derived from the information provided in Table 1.1.

It is also important to define the proton density fat fraction *PDFF* = ρ_{F} / (ρ_{W} + ρ_{F}), which is simply the ratio of the total fat proton density of the tissue to the total overall proton density, including water and fat.

From this mathematical formulation, $\boldsymbol{\rho}$ can be solved for and the triglyceride parameters determined. When performing triglyceride composition estimation, estimates of R_2^* and f_B need to be determined either simultaneously with or prior to estimating the triglyceride composition. A variety of methods have been developed in order to estimate R_2^* and f_B in fatty tissues along with the triglyceride parameters, including: iterative region growing [5], iterative least squares

[6], variable projection [7], and graph cuts [8]. An extensive review of these methods will not be provided here; however, Chapter 2 examines in detail how the variable projection and graph cut methods' dependencies on *a priori* knowledge of the relative amplitudes (α_m) of the fat resonance peaks can effect estimations of triglyceride composition and *PDFF*.

Quantitative Susceptibility Mapping

When placed in an external magnetic field, most materials are either diamagnetic or paramagnetic. Diamagnetic materials generate their own magnetic field or magnetization opposite the direction of the external field and counteract its effects. Paramagnetic materials generate their own magnetization in the same direction of the external field and enhance its effects. Magnetic susceptibility is a measure of the magnitude of the magnetization that is generated by a material in response to the external magnetic field. It is an intrinsic physical property of materials, including biological tissues, and can be measured from 3D multi-gradient echo MR data using a method known as quantitative susceptibility mapping (QSM) [9].

In QSM, the magnetic field at a given location $\boldsymbol{r}$ is defined as

$$\boldsymbol{b}(\boldsymbol{r}) = (\boldsymbol{d} * \boldsymbol{\chi})(\boldsymbol{r}) \qquad (1.5)$$

where $\boldsymbol{d}$ is a dipole kernel associated with the magnetization distribution over the entire imaged volume and χ is the magnetic susceptibility. In the presence of chemical shifts, such as those arising from fat in CSE-MRI, the magnetic field is given by

$$\boldsymbol{b}(\boldsymbol{r}) = (\boldsymbol{d} * \boldsymbol{\chi})(\boldsymbol{r}) - \sum_{m=1}^{M} \alpha_m(\boldsymbol{r})\sigma_m(\boldsymbol{r})B_o \qquad (1.6)$$

where α_m is the amplitude or concentration and σ_m is the relative chemical shift of the *m*th fat resonance peak and B_0 is the static magnetic field strength.

QSM consists of three main steps: 0) estimation of the total magnetic field (b), 1) removal of the background magnetic field (b_b), and 2) calculation of the susceptibility (χ) from the remaining local tissue field (b_t) through dipole inversion. A visual representation of this process for a human brain is shown in Figure 1.2.

As discussed in the previous section, f_B can be estimated using CSE-MRI using a variety of different methods in the presence of fat. Since these methods account for the chemical shifts associated with the fat peaks, the simplified equation for the magnetic field with no chemical shifts (Eq. (1.5)) can be used to solve for χ. In this case, b and f_B are proportional, and therefore, the former can easily be determined from the latter in order to realize step 0.

Removal of the background field from the total field (step 1) is most often achieved by finding a solution to Maxwell's Equation

$$\nabla^2\, \boldsymbol{b}(\boldsymbol{r}) = \mu_o(\nabla^2 \boldsymbol{m}(\boldsymbol{r})/3 - \nabla(\nabla \cdot \boldsymbol{m}(\boldsymbol{r}))) \qquad (1.7)$$

where $\boldsymbol{m}$ is the magnetization. Since the background field has no sources within the tissue volume ($\nabla^2 b_b = 0$), the Laplacian of the total field is equal to the Laplacian of the local tissue field ($\nabla^2 b = \nabla^2 b_t$).

Due to a lack of signal outside the tissue volume, additional *a priori* information is necessary in order to find a unique solution to Eq. (1.7) and remove the background field. The Laplacian boundary value method (LBV) assumes to know the boundary conditions *a priori* [10]. Since the tissue field is typically very weak in comparison to the background field, LBV finds a solution by approximating the values at the boundary to be the total field. If the boundary conditions are not known, then a solution can be determined using regularization to solve the inverse Laplacian, such as with the sophisticated harmonic artifact reduction for phase data (SHARP) method, which uses spectral truncation [11]. Many other methods that use different *a priori* information have also been developed, but they will not be discussed here. More information on the different types of background removal methods can be found in the following references [9, 12].

Once the background field has been removed, χ can be can determined from the remaining local tissue field through dipole inversion (step 2) by finding a solution to Eq. (1.5). However, Eq. (1.5) also lacks a unique solution due to the dipole kernel $\boldsymbol{d}$ going to zero at the magic angle (±54.7° with respect to the main magnetic field B_o). As with f_B estimation and background field removal, many methods have been developed in order to perform the inversion and handle the magic angle issue. Most commonly, dipole inversion is achieved through regularization:

$$\boldsymbol{\chi}(\boldsymbol{r}) = \underset{\boldsymbol{\chi}}{\boldsymbol{argmin}} \, \|\boldsymbol{w}(\boldsymbol{b} - \boldsymbol{d} * \boldsymbol{\chi})\|_2^2 + \boldsymbol{\lambda R}(\boldsymbol{\chi}) \qquad (1.8)$$

where w is a weighting factor, λ is the regularization parameter, and R is the regularization function. Various regularization functions, including piece-wise [13], gradient [14], and wavelet [14, 15] susceptibility functions, as well as functions that include morphological or structural priors [16, 17] have been proposed, and research into new regularization functions is still ongoing.

Since iron is paramagnetic and has a relatively large magnetic susceptibility in comparison to the differences between biological tissues, QSM has mostly been used to detect iron accumulation in the brain due to various diseases, such as Alzheimer’s and multiple sclerosis. More recently QSM of the liver, which contains fat, has been performed in order to study liver iron overload, which is common in patients receiving chronic blood transfusions and patients with diseases such as hereditary hemochromatosis, hepatitis C, alcoholic liver disease, and cirrhosis. Liver iron overload is also associated with heart complications.

Chapter 3 explores the use of QSM to quantify liver iron concentration using an ex vivo mouse model and compares it with other methods that are currently used to evaluate liver iron overload.

References

1. Ren, J., et al., *Composition of adipose tissue and marrow fat in humans by 1H NMR at 7 Tesla.* J Lipid Res, 2008. **49**(9): p. 2055-62.
2. Hamilton, G., et al., *MR properties of brown and white adipose tissues.* J Magn Reson Imaging, 2011. **34**(2): p. 468-73.
3. Hamilton, G., et al., *In vivo characterization of the liver fat (1)H MR spectrum.* NMR Biomed, 2011. **24**(7): p. 784-90.
4. Peterson, P. and S. Mansson, *Simultaneous quantification of fat content and fatty acid composition using MR imaging.* Magn Reson Med, 2013. **69**(3): p. 688-97.
5. Yu, H., et al., *Field map estimation with a region growing scheme for iterative 3-point water-fat decomposition.* Magnetic Resonance in Medicine: An Official Journal of the International Society for Magnetic Resonance in Medicine, 2005. **54**(4): p. 1032-1039.
6. Reeder, S.B., et al., *Iterative decomposition of water and fat with echo asymmetry and least-squares estimation (IDEAL): application with fast spin-echo imaging.* Magn Reson Med, 2005. **54**(3): p. 636-44.
7. Hernando, D., et al., *Joint estimation of water/fat images and field inhomogeneity map.* Magn Reson Med, 2008. **59**(3): p. 571-80.
8. Hernando, D., et al., *Robust water/fat separation in the presence of large field inhomogeneities using a graph cut algorithm.* Magn Reson Med, 2010. **63**(1): p. 79-90.
9. Wang, Y. and T. Liu, *Quantitative susceptibility mapping (QSM): decoding MRI data for a tissue magnetic biomarker.* Magnetic resonance in medicine, 2015. **73**(1): p. 82-101.
10. Zhou, D., et al., *Background field removal by solving the Laplacian boundary value problem.* NMR in Biomedicine, 2014. **27**(3): p. 312-319.
11. Schweser, F., et al., *Quantitative imaging of intrinsic magnetic tissue properties using MRI signal phase: an approach to in vivo brain iron metabolism?* Neuroimage, 2011. **54**(4): p. 2789-2807.
12. Schweser, F., et al., *An illustrated comparison of processing methods for phase MRI and QSM: removal of background field contributions from sources outside the region of interest.* NMR in Biomedicine, 2017. **30**(4): p. e3604.
13. De Rochefort, L., et al., *Quantitative MR susceptibility mapping using piece-wise constant regularized inversion of the magnetic field.* Magnetic Resonance in Medicine: An Official Journal of the International Society for Magnetic Resonance in Medicine, 2008. **60**(4): p. 1003-1009.
14. Kressler, B., et al., *Nonlinear regularization for per voxel estimation of magnetic susceptibility distributions from MRI field maps.* IEEE transactions on medical imaging, 2009. **29**(2): p. 273-281.
15. Wu, B., et al., *Whole brain susceptibility mapping using compressed sensing.* Magnetic resonance in medicine, 2012. **67**(1): p. 137-147.

16. Liu, J., et al., *Morphology enabled dipole inversion for quantitative susceptibility mapping using structural consistency between the magnitude image and the susceptibility map.* Neuroimage, 2012. **59**(3): p. 2560-2568.
17. de Rochefort, L., et al., *Quantitative susceptibility map reconstruction from MR phase data using bayesian regularization: validation and application to brain imaging.* Magnetic Resonance in Medicine: An Official Journal of the International Society for Magnetic Resonance in Medicine, 2010. **63**(1): p. 194-206.

Table 1.1
Theoretical 9 Fat Peak Model [3]

Peak Number	Water-Fat Chemical Shifts (ppm)	Theoretical Peak Amplitudes (Number of Protons)	Chemical Assignment
1	0.59	2*ndb	-CH=CH-
2	0.49	1	-CH-O-CO-
3	-0.50	4	$-CH_2-O-CO-$
4	-1.95	2*nmidb	$-CH=CH-CH_2-CH=CH-$
5	-2.46	6	$-CO-CH_2-CH_2-$
6	-2.68	4*(ndb-nmidb)	$-CH_2-CH=CH-CH_2-$
7	-3.10	6	$-CO-CH_2-CH_2-$
8	-3.40	6*(cl-4)-	$-(CH_2)_n-$
9	-3.80	9	$-(CH_2)_n-CH_3$

A theoretical 9 fat peak model with theoretical amplitudes of each fat resonance peak given in terms of the number of double bonds per molecule (*ndb*), the number of methylene-interrupted double bonds per molecule (*nmidb*), and the fatty acid chain length (*cl).*

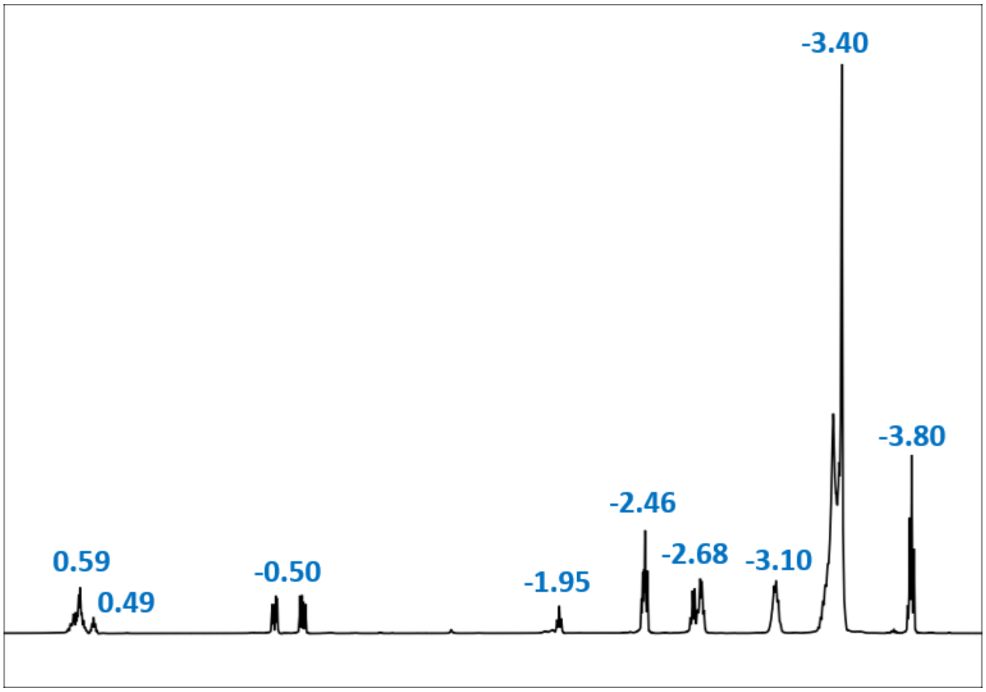

Figure 1.1: Representative water-suppressed ^{1}H NMR spectrum for murine brown adipose tissue. The chemical shift relative to water (in ppm) for each of the nine fat peaks is given above each peak.

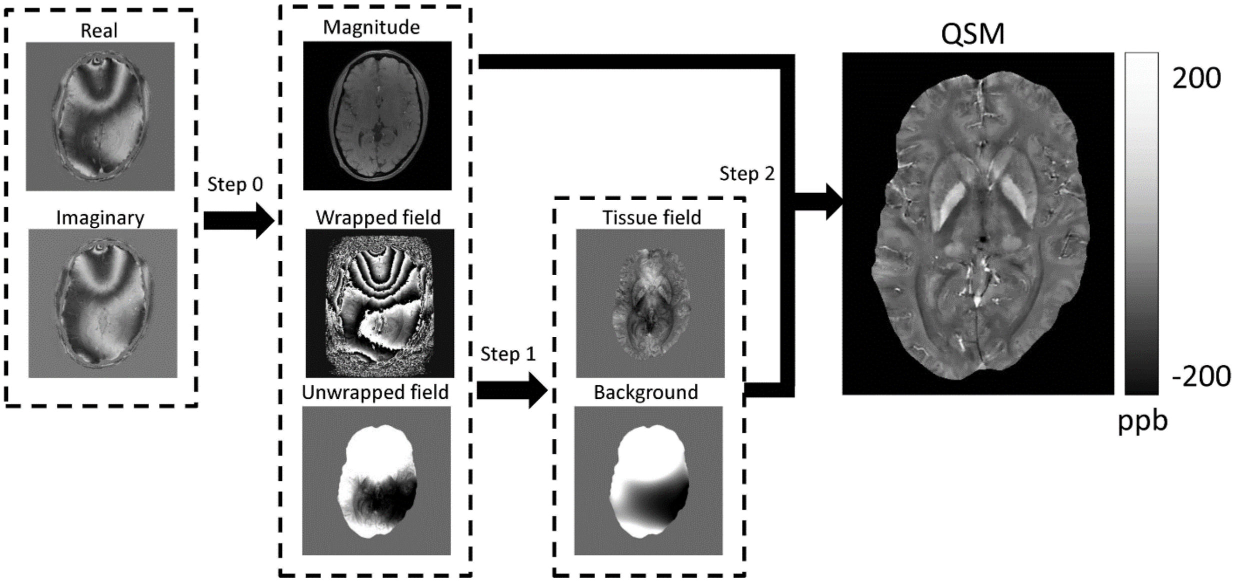

Figure 1.2: Quantitative susceptibility mapping flow chart [9]. Step 0: estimation of the unwrapped total magnetic field. Step 1: removal of the background field. Step 2: calculation of the susceptibility from the remaining local tissue field, which often uses regularization associated with the magnitude image. Figure reproduced with permission from publisher John Wiley and Sons.

CHAPTER 2

FAT SPECTRAL MODELING ON TRIGLYCERIDE COMPOSITION QUANTIFICATION USING CHEMICAL SHIFT ENCODED MAGNETIC RESONANCE IMAGING [1]

---

[1] Simchick, G., Yin, A., Yin, H., and Zhao, Q. 2018. *Magnetic resonance imaging*. 52:84-93. Reprinted here with permission of publisher Elsevier Inc.

Abstract

Purpose: To explore, at a high field strength of 7T, the performance of various fat spectral models on the quantification of triglyceride composition and proton density fat fraction (*PDFF*) using chemical-shift encoded MRI (CSE-MRI).

Methods: MR data was acquired from CSE-MRI experiments for various fatty materials, including oil and butter samples and in vivo brown and white adipose mouse tissues. Triglyceride composition and *PDFF* were estimated using various *a priori* 6- or 9-peak fat spectral models. To serve as references, NMR spectroscopy experiments were conducted to obtain material specific fat spectral models and triglyceride composition estimates for the same fatty materials. Results obtained using the spectroscopy derived material specific models were compared to results obtained using various published fat spectral models.

Results: Using a 6-peak fat spectral model to quantify triglyceride composition may lead to large biases at high field strengths. When using a 9-peak model, triglyceride composition estimations vary greatly depending on the relative amplitudes of the chosen *a priori* spectral model, while *PDFF* estimations show small variations across spectral models. Material specific spectroscopy derived spectral models produce estimations that better correlate with NMR spectroscopy estimations in comparison to those obtained using non-material specific models.

Conclusion: At a high field strength of 7T, a material specific 9-peak fat spectral model, opposed to a widely accepted or generic human liver model, is necessary to accurately quantify triglyceride composition when using CSE-MRI estimation methods that assume the spectral model to be known as *a priori* information. CSE-MRI allows for the quantification of the spatial distribution of triglyceride composition for certain in vivo applications. Additionally, *PDFF*

quantification is shown to be independent of the chosen *a priori* spectral model, which agrees with previously reported results obtained at lower field strengths (e.g. 3T).

Introduction

Chemical-shift encoded magnetic resonance imaging (CSE-MRI) water-fat separation has recently emerged as a useful method for the quantification of triglyceride composition in fatty tissues. In comparison to magnetic resonance spectroscopy (MRS), which only allows for the quantification of the average triglyceride composition in a localized volume of interest, CSE-MRI water-fat separation techniques allow for the quantification of triglyceride composition over an entire volume of interest with high spatial resolution [1-6]. Water-fat separation techniques, in general, have also been shown to produce results that are comparable to those obtained using spectroscopy methods [3, 7-14]. The ability to non-invasively quantify the spatial distribution of triglyceride composition may provide valuable clinical information about the development of obesity related diseases and assist in the evaluation of obesity related treatments through the monitoring of brown adipose tissue (BAT) activation and white adipose tissue (WAT) beiging, which have been shown to change triglyceride composition [15-18] and occur heterogeneously throughout the tissue [19-22].

CSE-MRI water-fat separation techniques have primarily been used to only separate the water and fat components of the MR signal to quantify proton density fat fraction (*PDFF*) [23-32] and has focused mostly on the study of nonalcoholic fatty liver disease and hepatic steatosis [9, 10, 12, 13, 33], as well as liver iron quantification [34-40]. These methods generally assume the liver fat spectral model (chemical shifts and relative amplitudes of the fat resonance peaks) to be known *a priori*, and therefore, the triglyceride composition is also assumed to be known *a priori*. The triglyceride composition determines the relative amplitudes of the fat peaks in the spectral model based upon three parameters: 1) the number of double bonds per molecule (*ndb*), which is associated with monounsaturated fatty acid composition, 2) the number of methylene-interrupted double bonds per molecule (*nmidb*), which is associated with polyunsaturated fatty acid composition, and 3) the fatty acid chain length (*cl*) [41, 42] (Table 2.1).

Hamilton *et al*. [41-43] has shown using MRS that the triglyceride compositions of brown, white, surface and deep subcutaneous, and visceral adipose tissue differ from that of liver tissue, and significant variations in triglyceride composition were observed across subjects [43]. Additionally, Leporq *et al.* [5, 6] has shown the presence of spatial variability in triglyceride composition within human liver tissue and murine visceral adipose tissue. This raises questions as to whether or not previously published fat spectral models can provide accurate results when used across various biological tissues, and even if using a tissue specific model, how natural spatial variability within the tissue and variability across subjects, as well as dynamic processes, such as BAT activation and WAT beiging, can affect triglyceride composition estimations.

In modeling the CSE-MR signal for adipose tissues, many different multi-fat peak models have been proposed [14, 30, 41, 42, 44, 45]. NMR spectroscopy performed at higher magnetic fields (e.g. 7T) has shown that the fat spectrum of adipose tissue may consist of as many as 10 different resonance peaks [45], with the chemical shifts being relatively fixed for all types of fatty tissues and materials, while the relative amplitudes of the peaks vary from sample to sample (Figure 2.1) based on triglyceride composition (Table 2.1). Despite availability of this 10-peak model, many studies have used fat spectral models containing less than 10 peaks to minimize errors arising from nonuniform excitation profiles and difficulties differentiating nearby fat resonance peaks due to spectral profile broadening at lower field strengths (e.g. 1.5T and 3T) [44, 45]. The two most commonly used fat spectral models are a 6-peak model and a 9-

peak model [42], which are provided in the ISMRM fat-water toolbox (https://www.ismrm.org/workshops/FatWater12/data.htm). The relative amplitudes provided in this toolbox are specific to human liver tissue, and these models have become widely accepted and are often used generically for other types of fatty tissues.

Recent works have made comparisons between the performances of different fat spectral models when estimating *PDFF* and the effective transverse relaxation rate (R_2^*) using CSE-MRI. Wang *et al.* [14] has shown that when evaluating *PDFF* in the human liver at 3T using various published fat spectral models containing a range of 3 to 9 peaks, no particular model proved to be superior, and all models produced results that correlated well with MRS-*PDFF*. Using a 6-peak model with fixed chemical shifts, Hong *et al*. [46] evaluated the variability in the estimations of both *PDFF* and R_2^* in the human liver at 3T using 60 variant relative amplitude models. Increasing variations in the estimates of *PDFF* and R_2^* were reported with increasing *PDFF* and R_2^*; however, these variations weren’t considered to be significant. These studies were both performed at low field strengths (e.g. 3T) and have focused on obtaining estimations solely within the human liver, which typically has a *PDFF* of less than 40%.

The aim of this paper is to further explore, for materials with higher *PDFF*s and at a high field strength (e.g. 7T), the effect and performance of using different 6- and 9-peak fat spectral models when estimating triglyceride composition (*ndb*, *nmidb*, and *cl*) and *PDFF* with a specific focus on differences in the relative amplitudes of the fat peaks. MRI and NMR spectroscopy experiments were conducted using oil and butter samples and an in vivo mouse model to evaluate the importance of using a material specific fat spectral model and to evaluate the variability in the estimations of triglyceride composition and *PDFF* obtained using various fat spectral models.

Material and Methods

NMR Spectroscopy Experiments

Three samples (corn oil, olive oil, and butter) were obtained from local grocery stores and prepared with a chloroform solvent (CDCl3). Then standard proton (^{1}H) NMR spectroscopy (rectangular excitation pulse followed by immediate acquisition) was performed on each sample using a 300 MHz Mercury Spectrometer (Varian Medical Systems, Palo Alto, CA) (flip angle FA = 45 degrees, repetition time TR = 2.7s, spectral width sw = 4800 Hz, pulse width pw = 4.75 µs, and 8 acquisitions for averaging).

The intercapsular brown adipose tissues (iBAT) from three 2-month-old C57/BL6 mice (n=3) were surgically removed and prepared using a standard NMR procedure [47]. Standard water suppressed ^{1}H NMR spectroscopy was then performed on each sample using a 600 MHz Varian Inova Spectrometer (FA = 90 degrees, TR = 2s, sw = 6600 Hz, pw = 6.3 µs, and 16 acquisitions for averaging).

Assuming a 9-peak spectral model (Table 2.1) [41, 42], the relative amplitudes of the fat peaks for all acquired spectra were determined by performing multiplet analysis using MNOVA (Mestrelab Research, S.L., Santiago de Compostela, Spain). Estimates of *ndb*, *nmidb,* and *cl* were obtained from the relative amplitudes using the mldivide algorithm provided by Matlab (Mathworks Inc., Natick, MA) to solve the linear system of equations associated with the theoretical peak amplitudes given in Table 2.1 [41, 42]. For the iBAT tissues, the average relative amplitudes of the three mice were used in estimating *ndb*, *nmidb,* and *cl*.

MRI Experiments

For phantom experiments, three small 5-ml vials (one filled with each oil or butter sample) were placed into a larger cylindrical tube (28 mm in diameter, 114 mm in length) filled with water. Then using a 7T Varian Magnex MRI Scanner, the tube containing the three samples was scanned with a 38 mm volume coil and a 2D multi-echo gradient-echo sequence with a unipolar readout gradient (TR = 200 ms, *FA* = 20 degrees, initial echo time TE_i = 1.7 ms, echo spacing *Δ*TE = 0.7 ms, 12 echoes, matrix size of 64x64, field of view *FOV* = 35x35 mm, slice thickness *thk* = 1 mm, and 6 acquisitions for averaging).

In vivo experiments were also performed to scan the iBAT and inguinal white adipose tissue (igWAT) of two two-month old C57/BL6 mice (n=2) using a 40 mm surface coil. Again, a 2D multi-echo gradient-echo sequence with a unipolar readout gradient was implemented (TR = 75 ms, *FA* = 20 degrees, TE_i = 3 ms, *Δ*TE = 0.525 ms, 12 echoes, matrix size of 128x128, *FOV* = 30x30 mm, *thk* = 1 mm, and 4 acquisitions for averaging). Animals were anaesthetized using isoflurane, and their respiratory rates were monitored throughout experimentation. A water heating pad was used to help maintain normal body temperature. All experimental procedures were approved by the Institutional Animal Use and Care Committee (IAUCC, University of Georgia).

For MRI experiments, *Δ*TE was selected based upon Monte Carlo simulations designed to find the optimal echo times for reducing the biases and variations in the estimations of triglyceride composition (*ndb*, *nmidb*, and *cl*) arising due to inaccuracies in the relative amplitudes of the fat spectral model. *Δ*TEs in the range of 1.0-1.4 π radians (corresponding to 0.5-0.7 ms at 7T) were determined to be optimal (see Appendix A). A minimally available TE_i was selected in order to reduce biases arising from noise, and Gaussian excitation pulses with full width at half-max bandwidths greater than 12 kHz were used to ensure near uniform excitation of the water and all fat peaks.

CSE-MRI Post Processing Methods

In CSE-MRI, the MR signal of a voxel containing water and fat, acquired using a series of *n* echoes, is given by

$$s(t_n) = (\rho_{\mathrm{W}} e^{-R^*_{2,\mathrm{W}} t_n} + \rho_{\mathrm{F}} \sum_{m=1}^{M} \alpha_m e^{i2\pi f_m t_n} e^{-R^*_{2,m} t_n}) e^{i2\pi f_B t_n} \qquad (2.1)$$

where t_n is the *n*th echo time, ρ_{W} and ρ_{F} are the water and fat signal densities, α_m is the amplitude and f_m is the frequency shift relative to water of the *m*th fat peak, f_B is the change in the frequency caused by static field inhomogeneities, and $\mathrm{R}^*_{2,\mathrm{W}}$ and $\mathrm{R}^*_{2,m}$ are the effective transverse relaxation rates of the water resonance peak and *m*th fat resonance peak.

It has been shown that accurate measurements of *PDFF* can be achieved when assuming a common R^*_2 for all chemical species [10, 11, 33]. Using this assumption, Eq. (2.1) can be rewritten as

$$s(t_n) = (\rho_{\mathrm{W}} + \rho_{\mathrm{F}} \sum_{m=1}^{M} \alpha_m e^{i2\pi f_m t_n}) e^{i2\pi f_B t_n} e^{-R^*_2 t_n} \qquad (2.2).$$

For each CSE-MRI dataset, the field map (f_B) and R^*_2 map were estimated first. The field map was estimated using a 2D graphcut algorithm [23, 24], and its contribution was removed from the signal prior to R^*_2 estimation. R^*_2 was then solved on a voxel by voxel basis using variable projection to perform complex non-linear least squares fitting [23, 24], as complex non-linear least squares fitting of the signal has been shown to outperform other methods in the presence of noise [48, 49]. Both the graphcut and variable projection algorithms assume the fat spectral model, frequency shifts (f_m) and relative amplitudes (α_m), of the signal model (Eq. (2.2)) to be known as *a priori* information.

Peterson *et al.* [3] proposed a linear system of equations which ties information regarding the triglyceride composition and the theoretical amplitudes of the fat resonance peaks together based on an 8 fat peak model. Using the previously estimated f_B and R_2^* maps within an adapted 6- or 9-peak linear system of equations, estimates of the decomposition parameters (ρ_W, ρ_F, *ndb*, *nmidb*, and *cl*) were determined on a voxel by voxel basis using the mldivide algorithm provided by Matlab to find the linear least-squares solution. The frequency shifts of the fat peaks (f_m), but not the relative amplitudes (α_m), of the fat spectral model are assumed to be known as *a priori* information within this linear system of equations. The chemical shifts and theoretical peak amplitudes for the 6- and 9-peak models are given in Table 2.1 [41, 42]. *PDFF* was then calculated using $PDFF = |\rho_F|/(|\rho_F|+|\rho_w|)$. A flowchart depicting the above-described CSE-MRI post-processing procedure is presented in Figure 2.2.

For all MRI samples, triglyceride composition (*ndb*, *nmidb*, and *cl*) and *PDFF* were estimated using the above described post-processing methods and various *a priori* fat spectral models listed in Table 2.2, which includes the widely accepted liver models provided in the ISMRM fat-water toolbox (models 9 and 10). Each model in Table 2.2 was either calculated using the theoretical peak amplitudes given in Table 2.1 and previously published values of *ndb*, *nmidb*, and *cl* [1, 41, 42] or were obtained from conducted spectroscopy experiments. For the published BAT and WAT models, values for *cl* were not presented by Hamilton *et al.* [41]. The *cl* values for these models were determined using the published *ndb*, *nmidb*, and calculated signal percentages given by Hamilton *et al.* [41] to solve for *cl* based on the theoretical peak amplitudes (Table 2.1).

For each sample and selected spectral model, average CSE-MRI estimations were determined throughout a region-of-interest that covered the full volume of the sample while avoiding voxels with partial volume effects. The variability of the CSE-MRI estimates across spectral models was evaluated by dividing the ranges of the average estimates by their corresponding medians. To determine which spectral models correlate better with spectroscopy estimations, the relative errors of the average CSE-MRI estimations with respect to the spectroscopy estimations were summed across *ndb, nmidb,* and *cl* for each model and then scaled between zero and one for each material. This provides a scaled bias for each material in which the model that correlates best with spectroscopy across the three parameters will be assigned a value of zero, the model that correlates worst with spectroscopy will be assigned a value of one, and all other models will fall between zero and one.

Results

NMR Spectroscopy Experiments

While the chemical shifts of the fat resonance peaks are relatively fixed, quantifiable differences in the relative amplitudes of the resonance peaks are observed across samples in the acquired NMR spectra (Figure 2.1), as well as differences in the estimations of *ndb, nmidb,* and *cl* (Table 2.2, models 2, 4, 5, and 7, and further referred to as the material specific spectroscopy models). For corn oil and olive oil, all estimations are slightly less than previously published results [1], except for *cl* of olive oil (Table 2.2). For butter, no previously published result was considered due to the large variation in the triglyceride composition of different types of butters. The estimations of *ndb* and *nmidb* for the iBAT are slightly greater than published values [41], while the *cl* estimate is less than the published value (Table 2.2).

MRI Experiments

Representative spatial maps of *ndb, nmidb, cl,* and *PDFF* obtained using the material specific spectroscopy models (Figure 2.3a-d) and the 9-peak liver model (Figure 2.3e-h) for the oil and butter samples are displayed in Figure 2.3. The estimations from the multiple material specific spectroscopy models were combined into one map by simply displaying the estimations obtained with each material specific spectroscopy model within the corresponding material's region-of-interest. Clear qualitative differences in triglyceride composition (*ndb, nmidb,* and *cl*), but not *PDFF,* are observed between the models, and spatial variations within each sample are also observed. Similarly, Figure 2.4 displays spatial maps of *ndb, nmidb, cl,* and *PDFF* for in vivo adipose tissues (intercapsular BAT and WAT). Spatial variations within these tissues are also observed.

To quantitatively evaluate the performance of various spectral models in estimating *ndb*, *nmidb, cl,* and *PDFF,* seven models (models 1-5 and 9-10 from Table 2.2) were examined for corn oil, olive oil, and butter, and five models (models 6-10 from Table 2.2) were examined for the in vivo iBAT and igWAT tissues. Figure 2.5a-c shows box plots that represent the difference between the average CSE-MRI estimations and the spectroscopy estimations for *ndb, nmidb,* and *cl* across the examined spectral models for each material. The results for three representative spectral models are individually labeled for comparison. It is observed that the majority of the average CSE-MRI estimations are greater than the estimations obtained using spectroscopy. In sixteen out of the twenty-one (76%) of the *ndb, nmidb,* and *cl* groups, use of a material specific spectroscopy model (green squares) produces results that correlate better with spectroscopy estimations (or the published values for igWAT) than the estimations obtained using the 6-peak and 9-peak liver models (blue diamonds and pink triangles). For all groups, the estimates obtained using the 6-peak liver model yield either the lower or higher end of the estimates among all spectral models, and in most cases, this model even produces estimations that are considered outliers (estimates not attached to the box by whiskers) from the rest of the results. Outliers were defined as estimates that were more than 1.5 times the interquartile range away from the top or bottom of the box. Even when excluding the 6-peak liver model, variations in the estimations of *ndb*, *nmidb*, and *cl* across spectral models are still relatively large (Figure 2.5a-c and Table 2.3); however, the variations in the estimations of *PDFF* are observed to be relatively small across all examined spectral models (Figure 2.5d and Table 2.3).

To determine whether the material specific spectroscopy models or other models perform better when estimating triglyceride composition (*ndb*, *nmidb*, and *cl*), a scaled bias was determined for each spectral model for each material (Figure 2.6 and Table 2.4). For four out of five of the materials studied in this work, use of a material specific spectroscopy model produces either the best or second best correlation with spectroscopy across the three parameters, and its estimations always correlate better than the estimations obtained using the widely accepted 6- and 9-peak liver models, except for iBAT. The 6-peak liver model produces the worst or second worst correlation for all five materials.

Discussion

The poor performance of the 6-peak model in this work suggests that a more accurate (e.g. 9-peak) spectral model is necessary when estimating triglyceride composition (*ndb*, *nmidb*, and *cl*) at a high field strength of 7T. Although the sufficiency of the 6-peak model has not specifically been explored at lower field strengths in relation to triglyceride composition quantification, many studies have used a 6-peak model to minimize errors arising from nonuniform excitation profiles and peak overlap due to spectral profile broadening when estimating *PDFF* at 1.5T and 3T [9, 12, 42, 44, 45, 49]. At higher field strengths, fat resonance peaks become more discernible from each other as the differences in the resonance frequencies of neighboring peaks increase and less peak broadening occurs. However, even when using a 9-peak model and ensuring near uniform excitation of all peaks, inaccuracies in the relative amplitudes of the spectral model can still lead to significant biases and variations in the estimations of triglyceride composition (Figure 2.5a-c and Table 2.3).

Despite the high SNR of the acquired data, the results for the phantom experiments still show large variations in the estimates of *ndb*, *nmidb*, and *cl* across the 9-peak spectral models examined. This demonstrates a substantial dependence of triglyceride composition quantification on the relative amplitudes of the fat spectral model and suggests that the choice of model needs to be carefully considered. However, the variations in the estimations of *PDFF* across the examined spectral models are relatively small for all materials, indicating that the *PDFF* estimate is relatively independent of the chosen spectral model. This agrees with previous observations by Hong *et al*. [46] and Wang *et al*. [14]; whose studies were performed at lower field strengths (e.g. 3T) and examined variability in the estimation of *PDFF* across spectral models in the human liver, which tends to have a *PDFF* of less than 40%. The work presented here further expands upon these observations for a higher field strength of 7T and for materials with higher *PDFF*s.

The importance of using a material specific spectral model, opposed to a widely accepted or generic spectral model, to estimate triglyceride composition is also demonstrated, as the estimates obtained using a material specific spectroscopy model produce results that correlate better with spectroscopy results in comparison to the other spectral models examined, including the 6- and 9-peak liver models provided in the ISMRM fat-water toolbox (Figure 2.6 and Table 2.4).

Within each fatty material, spatial variability in the estimates are still observed when using the material specific spectroscopy models (Figures 2.3-2.4). This is likely due to natural sample variability and biases arising from two factors: noise and spectral model inaccuracies caused by the natural sample variability. For the in vivo adipose tissues, inhomogeneity of the sample is naturally larger than in the oil and butter samples, and other factors, such as respiratory motion and blood flow, may lead to additional biases. However, using a material specific spectral model may be useful in reducing estimation biases and lead to more accurate spatial quantification.

The need for an *a priori* material specific spectral model makes the triglyceride composition estimation process seem circular. However, spectral models obtained using spectroscopy methods only quantify the average concentrations of the fat peaks throughout a localized volume of interest. These methods do not allow for the spatial quantification of triglyceride composition, while CSE-MRI methods do allow for spatial quantification.

Accurate spatial quantification is important, as certain types of adipose tissue are known to be spatially heterogeneous [22, 50-53], and dynamic processes, such as BAT activation and WAT beiging, have been shown to change the triglyceride composition of the tissue [15-18] and occur heterogeneously throughout the tissue [19-22]. Therefore, the ability to non-invasively quantify the spatial distribution of triglyceride composition may allow for the monitoring of these two processes, which may provide valuable clinical information related to the development of obesity related diseases and assist in the evaluation of obesity related treatments.

Opposed to methods that require the relative amplitudes of the spectral model to be known as *a priori* information, iterative techniques to solve for triglyceride composition without *a priori* knowledge of the relative amplitudes may be more effective [1-6]. The methods used in this work were chosen as they have been shown to outperform iterative decomposition of water and fat with echo asymmetry and least-squares estimation with T_2^* correction (T_2^*-IDEAL) and weighted least squares T_2^*-IDEAL when estimating *PDFF* and R_2^* in the presence of noise [48, 49].

There are several limitations to this work. In order to accurately quantify triglyceride composition, multiple factors related to the signal model must be accounted for. Eq. (2.2) accounts for B_o inhomogeneity, R_2^* decay, and the spectral complexity of fat. However, other factors not accounted for in the signal model, such as eddy currents [8], T1-weighting [25, 54], and noise [10, 25, 33, 48, 49], can lead to biases in the estimations, and therefore, should also be addressed. It is noted that phase errors arising due to eddy currents were not of concern in this work since upon examination of the phase within all samples and within the water background surrounding the phantom samples, no significant deviations from linear behavior were observed.

T1-weighting biases can be avoided by using a small flip angle of typically 5 degrees or less. The bias in the estimation of *PDFF* arising from T1-weighting has been shown to lead to overestimations that are most severe for materials with moderate *PDFF*s and minimal at extremely low and high *PDFF*s [25, 54]. Therefore, bias in the estimation of *PDFF* due to T1-weighting is expected to be relatively small within the oil, butter, and igWAT samples due to their extremely high *PDFF*s; however, the iBAT samples are susceptible to this bias due to their moderate *PDFF*s. For a flip angle of 20 degrees, the biases due to T1-weighting in the estimations of *ndb*, *nmidb*, and *cl* have also been shown to lead to overestimations [54];

therefore, T1-biases may contribute to the overestimations observed in this work in comparison to the spectroscopy results (Figure 2.5a-c).

Unlike the bias arising due to T1-weighting, the bias in the estimation of *PDFF* arising due to noise has been shown to lead to underestimations for materials with high *PDFF*s, and minimal bias is observed for materials with moderate *PDFF*s [25]. However, it is unclear how noise will affect the estimations of *ndb*, *nmidb*, and *cl*. The biases in the estimations due to noise are expected to be relatively small within the phantom samples due to the high SNR of the acquired data. However, the estimations within the in vivo samples are more susceptible to noise biases.

Hamilton *et al*. [43] recently reported that allowing *cl* to freely vary while estimating *ndb* and *nmidb* in various types of adipose tissues from MRS data acquired at 3T led to unstable estimates, but the stability of the estimates greatly improved when fixing *cl* to a predefined value. The range of *cl* values deemed biologically plausible by Hong *et al.* [46] is 17.35 to 17.55, and previously published values of *cl* by Bydder *et al*. [1] for three different types of human adipose tissue are in the range of 17.33 to 17.48. These ranges are smaller than the ranges for *cl* that were observed in this work. However, since the biologically plausible range of *cl* is likely very small, fixing *cl* may produce results that better correlate with spectroscopy estimations and may reduce the observed variability in the estimations across spectral models.

Some of the triglyceride composition (*ndb*, *nmidb*, and *cl*) estimations presented in this work are physically unlikely, as they either differ significantly from the USDA National Nutrient Database for Standard Reference [55] or fall outside of the biologically plausible ranges found in mammals. Despite their unlikelihood, the sensitivity of triglyceride composition quantification on the chosen spectral model is still demonstrated.

Conclusion

CSE-MRI water-fat separation is a useful method that allows for the spatial quantification of triglyceride composition, while MRS only provides an averaged estimation within a localized volume of interest. At high field strengths, a more accurate fat spectral model (e.g. a 9-peak model opposed to a 6-peak model) is necessary to accurately quantify triglyceride composition. However, the chosen 9-peak spectral model should be carefully selected, as using various relative amplitude models is shown in this work to produce large variations in the estimations of triglyceride composition, and use of a spectroscopy derived material specific 9-peak spectral model, opposed to a widely accepted or generic spectral model, is shown to produce estimates that more closely correlate with spectroscopy results.

Despite the strong dependence of the chosen spectral model on the estimation of triglyceride composition, the estimation of *PDFF* is shown to be independent of the chosen spectral model at high field strengths of 7T, which agrees with previously reported results at lower field strengths (e.g. 3T).

References

1. Bydder, M., O. Girard, and G. Hamilton, *Mapping the double bonds in triglycerides.* Magn Reson Imaging, 2011. **29**(8): p. 1041-6.
2. Berglund, J., H. Ahlstrom, and J. Kullberg, *Model-based mapping of fat unsaturation and chain length by chemical shift imaging--phantom validation and in vivo feasibility.* Magn Reson Med, 2012. **68**(6): p. 1815-27.
3. Peterson, P. and S. Mansson, *Simultaneous quantification of fat content and fatty acid composition using MR imaging.* Magn Reson Med, 2013. **69**(3): p. 688-97.
4. Leporq, B., et al., *Quantification of the triglyceride fatty acid composition with 3.0 T MRI.* NMR Biomed, 2014. **27**(10): p. 1211-21.
5. Leporq, B., et al., *Hepatic fat fraction and visceral adipose tissue fatty acid composition in mice: Quantification with 7.0 T MRI.* Magnetic resonance in medicine, 2016. **76**(2): p. 510-518.
6. Leporq, B., et al., *Simultaneous MR quantification of hepatic fat content, fatty acid composition, transverse relaxation time and magnetic susceptibility for the diagnosis of non-alcoholic steatohepatitis.* NMR in Biomedicine, 2017. **30**(10).

7. Bydder, M., et al., *Relaxation effects in the quantification of fat using gradient echo imaging.* Magn Reson Imaging, 2008. **26**(3): p. 347-59.
8. Hernando, D., et al., *Addressing phase errors in fat-water imaging using a mixed magnitude/complex fitting method.* Magn Reson Med, 2012. **67**(3): p. 638-44.
9. Hines, C.D., et al., *T(1) independent, T(2) (*) corrected chemical shift based fat-water separation with multi-peak fat spectral modeling is an accurate and precise measure of hepatic steatosis.* J Magn Reson Imaging, 2011. **33**(4): p. 873-81.
10. Horng, D.E., et al., *Comparison of R2* correction methods for accurate fat quantification in fatty liver.* J Magn Reson Imaging, 2013. **37**(2): p. 414-22.
11. Horng, D.E., D. Hernando, and S.B. Reeder, *Quantification of liver fat in the presence of iron overload.* J Magn Reson Imaging, 2017. **45**(2): p. 428-439.
12. Meisamy, S., et al., *Quantification of hepatic steatosis with T1-independent, T2-corrected MR imaging with spectral modeling of fat: blinded comparison with MR spectroscopy.* Radiology, 2011. **258**(3): p. 767-75.
13. Reeder, S.B., et al., *Quantification of hepatic steatosis with MRI: the effects of accurate fat spectral modeling.* J Magn Reson Imaging, 2009. **29**(6): p. 1332-9.
14. Wang, X., D. Hernando, and S.B. Reeder, *Sensitivity of chemical shift-encoded fat quantification to calibration of fat MR spectrum.* Magn Reson Med, 2016. **75**(2): p. 845-51.
15. Yaligar, J., et al., *Metabolic Imaging of Dynamic Fat Mobilization in Activated Brown Adipose Tissue.* In Proceedings of the 25th Annual Meeting of ISMRM, Honolulu, USA, 2017.
16. Campbell, B., et al., *Classification of White and Brown Adipose Tissue using a Support Vector Machine.* In Proceedings of the 25th Annual Meeting of ISMRM, Honolulu, USA, 2017.
17. Simchick, G., et al., *Characterization of Brown Adipose Tissue using Multi-Varying-Peak MR Spectroscopy (MVP-MRS).* In Proceedings of the 24th Annual Meeting of ISMRM, Singapore, 2016: p. 3280.
18. Simchick, G., et al., *Dynamic Monitoring of Brown Adipose Tissue Activation and White Adipose Tissue Beiging.* In Proceedings of the 25th Annual Meeting of ISMRM, Honolulu, USA, 2017.
19. Barreau, C., et al., *Regionalization of browning revealed by whole subcutaneous adipose tissue imaging.* Obesity, 2016. **24**(5): p. 1081-1089.
20. Wang, B., et al., *Retinoic acid induces white adipose tissue browning by increasing adipose vascularity and inducing beige adipogenesis of PDGFRα+ adipose progenitors.* Cell discovery, 2017. **3**: p. 17036.
21. Mueller, E., *Understanding the variegation of fat: novel regulators of adipocyte differentiation and fat tissue biology.* Biochimica et Biophysica Acta (BBA)-Molecular Basis of Disease, 2014. **1842**(3): p. 352-357.
22. Lee, Y.-H., et al., *Metabolic heterogeneity of activated beige/brite adipocytes in inguinal adipose tissue.* Scientific reports, 2017. **7**: p. 39794.
23. Hernando, D., et al., *Joint estimation of water/fat images and field inhomogeneity map.* Magn Reson Med, 2008. **59**(3): p. 571-80.
24. Hernando, D., et al., *Robust water/fat separation in the presence of large field inhomogeneities using a graph cut algorithm.* Magn Reson Med, 2010. **63**(1): p. 79-90.

25. Liu, C.Y., et al., *Fat quantification with IDEAL gradient echo imaging: correction of bias from T(1) and noise.* Magn Reson Med, 2007. **58**(2): p. 354-64.
26. Reeder, S.B., et al., *Iterative decomposition of water and fat with echo asymmetry and least-squares estimation (IDEAL): application with fast spin-echo imaging.* Magn Reson Med, 2005. **54**(3): p. 636-44.
27. Reeder, S.B., et al., *Multicoil Dixon chemical species separation with an iterative least-squares estimation method.* Magn Reson Med, 2004. **51**(1): p. 35-45.
28. Tsao, J. and Y. Jiang, *Hierarchical IDEAL: fast, robust, and multiresolution separation of multiple chemical species from multiple echo times.* Magn Reson Med, 2013. **70**(1): p. 155-9.
29. Yu, H., et al., *Multiecho reconstruction for simultaneous water-fat decomposition and T2* estimation.* J Magn Reson Imaging, 2007. **26**(4): p. 1153-61.
30. Yu, H., et al., *Multiecho water-fat separation and simultaneous R2* estimation with multifrequency fat spectrum modeling.* Magn Reson Med, 2008. **60**(5): p. 1122-34.
31. Berglund, J. and J. Kullberg, *Three-dimensional water/fat separation and T2* estimation based on whole-image optimization--application in breathhold liver imaging at 1.5 T.* Magn Reson Med, 2012. **67**(6): p. 1684-93.
32. Hu, H.H., et al., *Comparison of fat-water MRI and single-voxel MRS in the assessment of hepatic and pancreatic fat fractions in humans.* Obesity (Silver Spring), 2010. **18**(4): p. 841-7.
33. Reeder, S.B., et al., *On the performance of T2* correction methods for quantification of hepatic fat content.* Magn Reson Med, 2012. **67**(2): p. 389-404.
34. Simchick, G., et al., *Assessment of MR-based and quantitative susceptibility mapping for the quantification of liver iron concentration in a mouse model at 7T.* Magnetic Resonance in Medicine. **0**(0).
35. Sharma, S.D., et al., *MRI-based quantitative susceptibility mapping (QSM) and R2* mapping of liver iron overload: Comparison with SQUID-based biomagnetic liver susceptometry.* Magnetic resonance in medicine, 2017. **78**(1): p. 264-270.
36. Sharma, S.D., et al., *Quantitative susceptibility mapping in the abdomen as an imaging biomarker of hepatic iron overload.* Magnetic resonance in medicine, 2015. **74**(3): p. 673-683.
37. Lin, H., et al., *Quantitative susceptibility mapping in combination with water-fat separation for simultaneous liver iron and fat fraction quantification.* European radiology, 2018: p. 1-11.
38. Hernando, D., et al., *Quantification of liver iron with MRI: state of the art and remaining challenges.* Journal of Magnetic Resonance Imaging, 2014. **40**(5): p. 1003-1021.
39. Hernando, D., et al., *Magnetic susceptibility as a B0 field strength independent MRI biomarker of liver iron overload.* Magnetic resonance in medicine, 2013. **70**(3): p. 648-656.
40. Taylor, B.A., et al., *Simultaneous field and R 2* mapping to quantify liver iron content using autoregressive moving average modeling.* Journal of Magnetic Resonance Imaging, 2012. **35**(5): p. 1125-1132.
41. Hamilton, G., et al., *MR properties of brown and white adipose tissues.* J Magn Reson Imaging, 2011. **34**(2): p. 468-73.

42. Hamilton, G., et al., *In vivo characterization of the liver fat (1)H MR spectrum.* NMR Biomed, 2011. **24**(7): p. 784-90.
43. Hamilton, G., et al., *In vivo triglyceride composition of abdominal adipose tissue measured by 1 H MRS at 3T.* J Magn Reson Imaging, 2017. **45**(5): p. 1455-1463.
44. Dimitrov, I.E., et al., *In vivo determination of human breast fat composition by (1)H magnetic resonance spectroscopy at 7 T.* Magn Reson Med, 2012. **67**(1): p. 20-6.
45. Ren, J., et al., *Composition of adipose tissue and marrow fat in humans by 1H NMR at 7 Tesla.* J Lipid Res, 2008. **49**(9): p. 2055-62.
46. Hong, C.W., et al., *MRI proton density fat fraction is robust across the biologically plausible range of triglyceride spectra in adults with nonalcoholic steatohepatitis.* Journal of Magnetic Resonance Imaging, 2018. **47**(4): p. 995-1002.
47. Teng, Q., in *Structural Biology: Practical NMR Applications*. 2013, Springer: New York.
48. Hernando, D., J.H. Kramer, and S.B. Reeder, *Multipeak fat-corrected complex R2* relaxometry: theory, optimization, and clinical validation.* Magn Reson Med, 2013. **70**(5): p. 1319-31.
49. Hernando, D., Z.P. Liang, and P. Kellman, *Chemical shift-based water/fat separation: a comparison of signal models.* Magn Reson Med, 2010. **64**(3): p. 811-22.
50. Kwok, K.H., K.S. Lam, and A. Xu, *Heterogeneity of white adipose tissue: molecular basis and clinical implications.* Experimental & molecular medicine, 2016. **48**(3): p. e215.
51. Berry, D.C., et al., *The developmental origins of adipose tissue.* Development, 2013. **140**(19): p. 3939-3949.
52. Kruglikov, I.L. and P.E. Scherer, *Dermal adipocytes and hair cycling: is spatial heterogeneity a characteristic feature of the dermal adipose tissue depot?* Experimental dermatology, 2016. **25**(4): p. 258-262.
53. Brooksby, B., et al., *Imaging breast adipose and fibroglandular tissue molecular signatures by using hybrid MRI-guided near-infrared spectral tomography.* Proceedings of the National Academy of Sciences, 2006. **103**(23): p. 8828-8833.
54. Peterson, P., J. Svensson, and S. Mansson, *Relaxation effects in MRI-based quantification of fat content and fatty acid composition.* Magn Reson Med, 2014. **72**(5): p. 1320-9.
55. Gebhardt, S., et al., *USDA national nutrient database for standard reference, release 21.* United States Department of AgricultureAgricultural Research Service, 2008.

Table 2.1
Theoretical 9 Fat Peak Model [41, 42]

Water-Fat Chemical Shifts (ppm)	**Theoretical Peak Amplitudes (Number of Protons)**
0.59	2*ndb
0.49	1
-0.50	4
-1.95	2*nmidb
-2.46	6
-2.68	4*(ndb-nmidb)
-3.10	6
-3.40	6*(cl-4)-8*ndb+2*nmidb
-3.80	9

A theoretical 9 fat peak model with theoretical amplitudes of each fat resonance peak given in terms of the number of double bonds per molecule (*ndb*), the number of methylene-interrupted double bonds per molecule (*nmidb*), and the fatty acid chain length (*cl)* [41, 42]. The 6-peak model combines the peaks located at 0.49 and 0.59 ppm, -2.46 and -2.68 ppm, and -3.10 and -3.40 ppm into common peaks located at 0.60, -2.60, and -3.40 ppm, respectively.

Table 2.2

Chemical Shifts and Relative Amplitudes (%) of Various Spectral Models and Their Corresponding Triglyceride Composition Parameters

	Water-Fat Chemical Shifts (ppm)									**Triglyceride Parameters**		
9 Peak Fat Model	**-3.80**	**-3.40**	**-3.10**	**-2.68**	**-2.46**	**-1.95**	**-0.50**	**0.49**	**0.59**	**NDB**	**NMIDB**	**CL**
Corn Oil												
1. Published [1]	9.01	51.61	6.00	10.25	6.00	3.50	4.00	1.00	8.63	4.31	1.75	17.76
2. Spectroscopy	7.74	50.83	7.60	9.97	6.64	3.43	4.57	1.22	8.01	3.99	1.58	17.04
Olive Oil												
3. Published [1]	8.77	58.46	5.84	9.90	5.84	0.68	3.90	0.97	5.63	2.89	0.35	17.74
4. Spectroscopy	6.90	59.17	6.92	9.96	6.13	0.43	4.23	1.28	4.99	2.78	0.13	18.23
Butter												
Published	-	-	-	-	-	-	-	-	-	-	-	-
5. Spectroscopy	8.37	57.50	6.39	6.89	7.33	2.07	4.68	1.10	5.67	2.68	1.02	16.42
BAT												
6. Published [41]	8.97	59.32	5.98	7.98	5.98	1.40	3.99	1.00	5.38	2.70	0.70	17.28
7. Spectroscopy	8.10	56.36	6.99	8.74	6.64	1.80	4.86	0.97	5.55	2.83	0.74	16.65
WAT												
8. Published [41]	8.95	56.43	5.97	9.15	5.97	1.99	3.98	0.99	6.57	3.30	1.00	17.52
Spectroscopy	-	-	-	-	-	-	-	-	-	-	-	-
Liver												
9. Published [42]	8.75	64.15	5.83	6.22	5.83	0.62	3.89	0.97	3.73	1.92	0.32	17.45
Spectroscopy	-	-	-	-	-	-	-	-	-	-	-	-

	Water-Fat Chemical Shifts (ppm)						**Triglyceride Parameters**		
6 Peak Fat Model	**-3.80**	**-3.40**	**-2.60**	**-1.95**	**-0.50**	**0.60**	**NDB**	**NMIDB**	**CL**
Liver									
10. Published [42]	8.75	69.98	12.06	0.62	3.89	4.71	1.92	0.32	17.45

Spectral models used when performing CSE-MRI estimations. Models 2, 4, 5, and 7 were obtained from conducted spectroscopy experiments, and the triglyceride parameters (*ndb*, *nmidb*, and *cl*) were estimated from the relative amplitude measurements. The rest of the models were calculated using previously published values for the triglyceride parameters [1, 41, 42] and the theoretical peak amplitudes listed in Table 2.1.{Angelucci, 2000 #103}

Table 2.3
Variability (%) in CSE-MRI Estimations across Spectral Models

Material	NDB	NMIDB	CL	PDFF
Corn Oil	13.2	16.0	6.57	0.04
Olive Oil	15.2	44.7	5.64	0.09
Butter	22.4	28.1	8.10	0.05
iBAT(1)	10.3	6.76	4.49	1.61
iBAT(2)	27.0	18.6	10.3	2.61
igWAT(1)	5.35	11.5	3.35	2.82
igWAT(2)	6.54	6.14	5.37	0.19

Variability was determined as the range of the average CSE-MRI estimations across the examined spectral models for each parameter and material divided by the corresponding median of the estimates. The estimates obtained using the 6-peak model (model 10 in Table 2.2) were excluded when calculating the variability; therefore, for phantom experiments, the estimates obtained using models 1-5 and model 10 were used, and for the in vivo experiments, the estimates obtained using models 6-9 were used.

Table 2.4

Scaled Bias of Each Spectral Model for Each Material

	Model						
Material	**1**	**2**	**3**	**4**	**5**	**9**	**10**
Corn Oil	0.41	0.15	0.19	0.00	0.25	0.26	1.00
Olive Oil	0.24	0.04	0.11	0.00	0.18	0.20	1.00
Butter	1.00	0.43	0.47	0.00	0.69	0.73	0.95

	Model				
Material	**6**	**7**	**8**	**9**	**10**
iBAT	0.24	0.05	0.35	0.00	1.00
igWAT	0.05	0.16	0.00	0.28	1.00

Scaled biases were determined by calculating the relative errors of the average CSE-MRI estimations with respect to the spectroscopy estimations for *ndb, nmidb,* and *cl*, summing across the three parameters for each model, and then scaling between zero and one for each material. Models that correlate better with spectroscopy tend towards zero and models that correlate more poorly tend towards one.

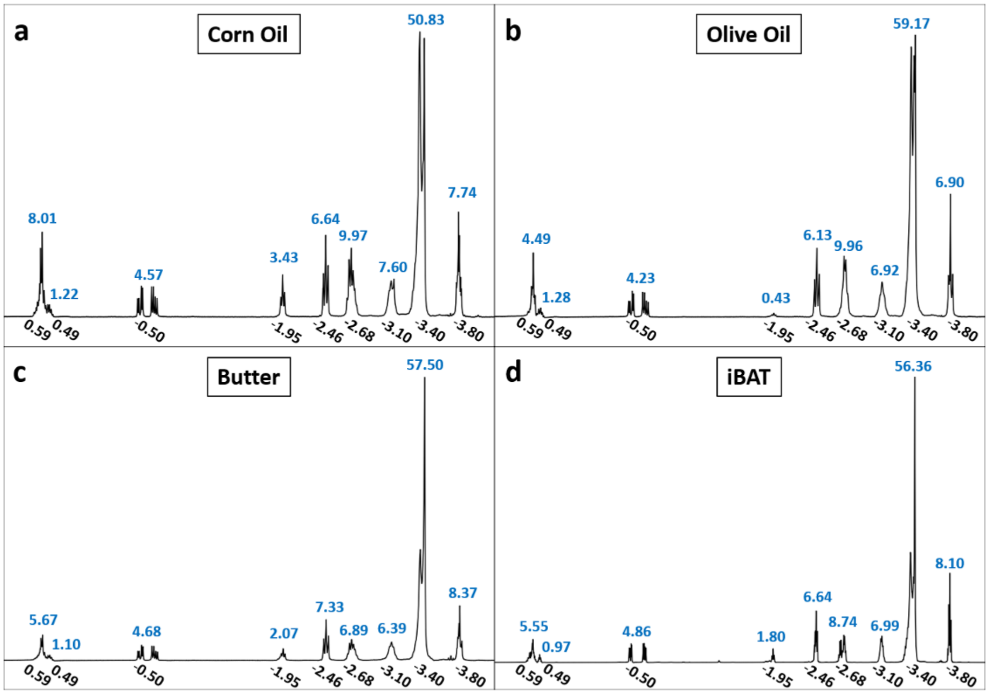

Figure 2.1: Representative spectra for corn oil (a), olive oil (b), butter (c), and surgically removed iBAT tissue (d) obtained using ^{1}H NMR. For each spectrum, the locations of the 9 fat resonance peaks (ppm relative to water) listed in Table 2.1 and their measured relative amplitudes (%) are provided below and above each peak, respectively. The chemical shifts of the 9 peaks are consistent across materials; however, the measured relative amplitudes of the peaks vary across materials. Table 2.2 gives estimates of triglyceride composition for each material obtained from the measured relative amplitudes (models 2, 4, 5, and 7).

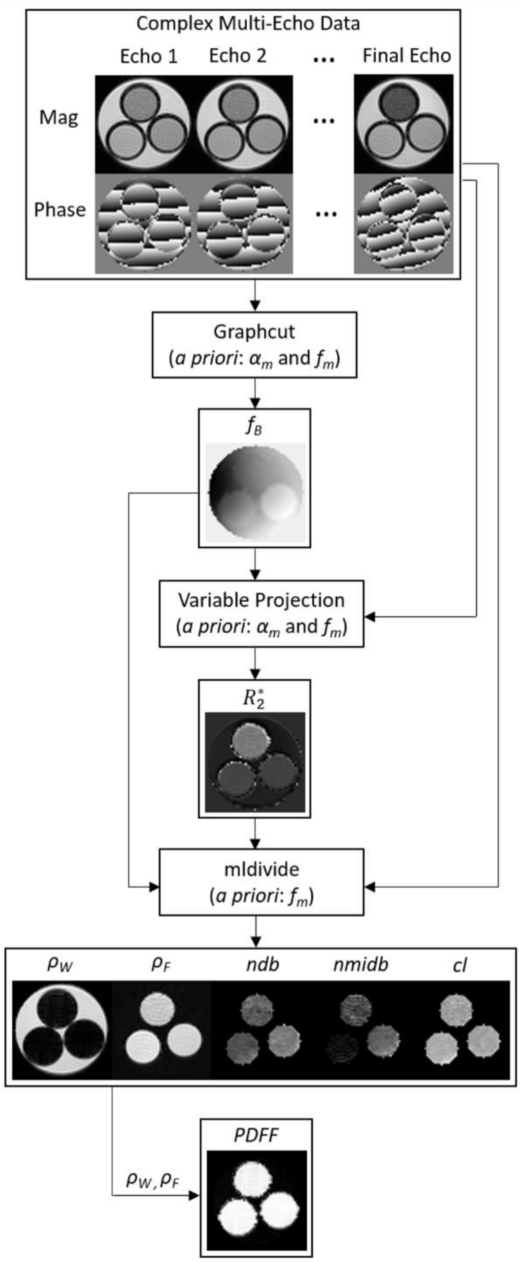

Figure 2.2: A flowchart depicting the MRI post-processing procedure used in this work. Step 1, the field map (f_B) was estimated from the complex multi-echo data using a 2D graphcut algorithm. Step 2, R_2^* was estimated using the previously estimated field map from step 1 and a variable projection algorithm. Step 3, using the field map and R_2^* estimations from steps 1 and 2, the decomposition parameters (ρ_W, ρ_F, *ndb*, *nmidb*, and *cl*) were determined by solving the adapted 6- or 9-peak linear system of equations using the mldivide algorithm. Finally, *PDFF* was estimated using the already estimated ρ_W and ρ_F maps. The necessary *a priori* spectral model information for each algorithm is given below its name.

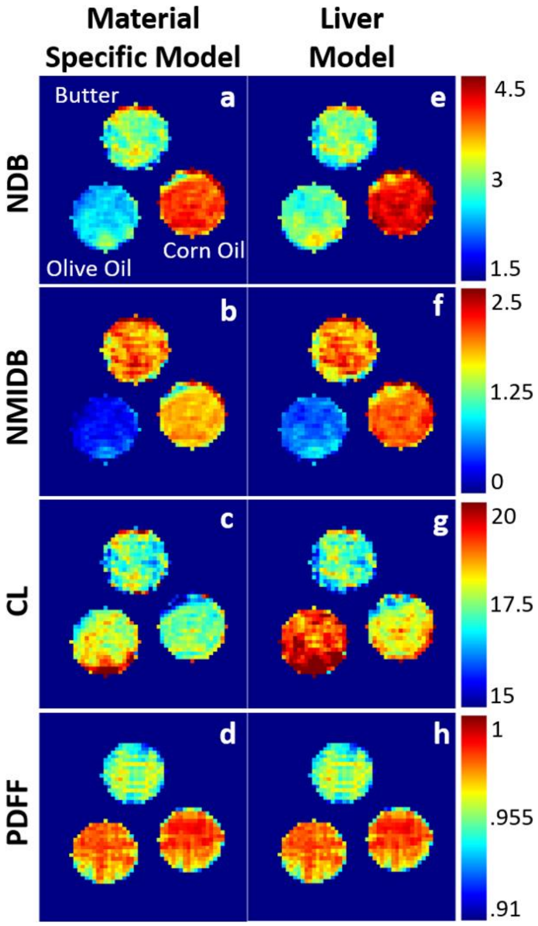

Figure 2.3: Representative *ndb* (first row), *nmidb* (second row), *cl* (third row), and *PDFF* (fourth row) maps obtained using the corresponding material specific spectroscopy models (models 2, 4, and 5 in Table 2.2) (first column, a-d) and the 9-peak liver model (model 9 in Table 2.2) (second column, e-h) for olive oil (bottom left vial), corn oil (bottom right vial), and butter (top vial). Clear differences in the estimations are observed between models, except for *PDFF*. Spatial variability within each of the samples is also observed.

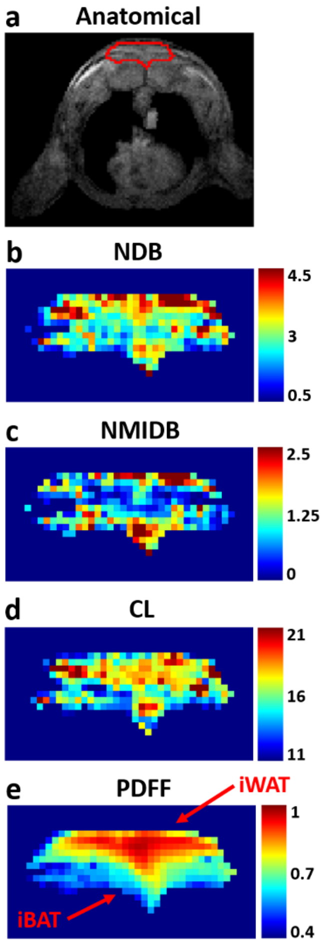

Figure 2.4: Representative anatomical image (a) and *ndb* (b), *nmidb* (c), *cl* (d), and *PDFF* (e) maps displaying the intercapsular region, which includes brown (bottom section as shown in e) and white (top-middle section as shown in e) adipose tissue (iBAT and iWAT), of a mouse from the in vivo experiments. Qualitative differences in the estimations are observed between the iBAT and iWAT, especially for *PDFF*. Natural biological, spatial variability within each tissue is also observed. The estimations displayed here were obtained using the material specific spectroscopy model for the iBAT and the published model for iWAT (models 7 and 8 in Table 2.2).

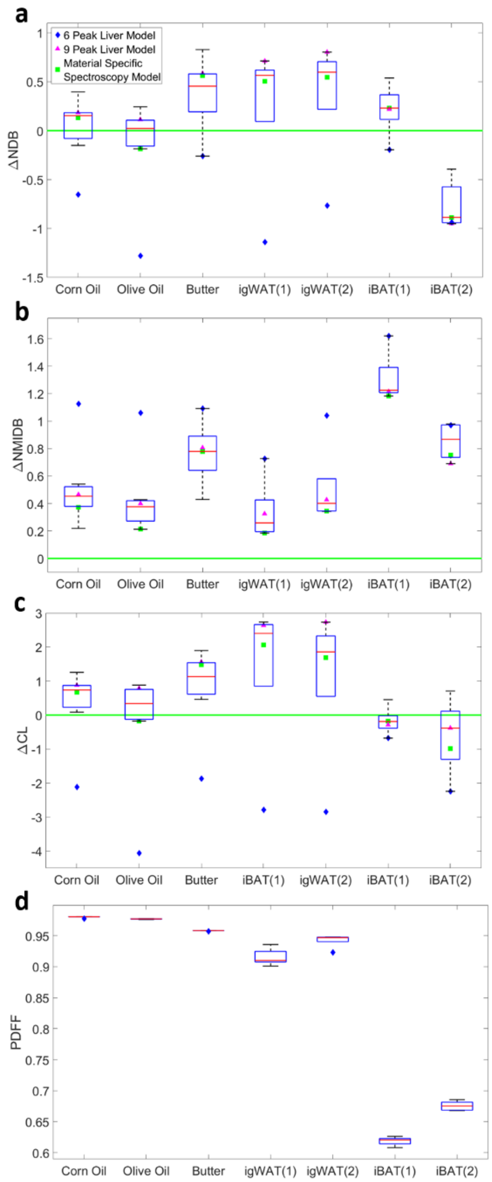

Figure 2.5: Box plots representing the difference between the average CSE-MRI estimations and the spectroscopy estimations for *ndb* (a), *nmidb* (b), and *cl* (c) across various spectral models (models 1-5 and 9-10 in Table 2.2 for the oil and butter samples and models 6-10 for the in vivo tissues). The 6-peak liver (blue diamonds), 9-peak liver (pink triangles), and material specific spectroscopy (green squares) model estimations are shown individually. For the igWAT samples, the published WAT model (model 8 in Table 2.2) was considered to be the material specific model. Box plots representing the average CSE-MRI estimations of *PDFF* (d) are also presented. All outliers shown here are associated with estimations obtaining when using the 6-peak liver model (blue diamonds).

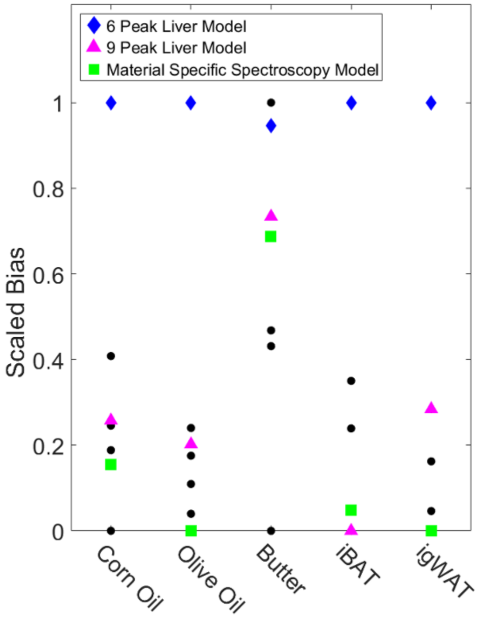

Figure 2.6: A scatter plot displaying the scaled bias of each spectral model for each material. The 6-peak liver (blue diamonds), 9-peak liver (pink triangles), and material specific spectroscopy (green squares) model biases are specifically given. For the igWAT, the published WAT model (model 8 in Table 2.2) was considered to be the material specific model. Scaled biases were obtained by calculating the relative errors of the average CSE-MRI estimations with respect to the spectroscopy estimations for *ndb*, *nmidb*, and *cl*, summing across the three parameters for each model, and then scaling between zero and one for each material. Models that correlate better with spectroscopy tend towards zero and models that correlate more poorly tend towards one. Numeric scaled biases are provided in Table 2.4.

CHAPTER 3

ASSESSMENT OF MR-BASED R_2^* AND QUANTITATIVE SUSCEPTIBILITY MAPPING FOR THE QUANTIFICATION OF LIVER IRON CONCENTRATION IN A MOUSE MODEL AT 7T [1]

---

[1] Simchick, G., Liu, Z., Nagy, T., Xiong, M., and Zhao, Q. 2018. *Magnetic Resonance in Medicine*. 80(5):2081-2093.

Reprinted here with permission of publisher John Wiley and Sons.

Abstract

Purpose: To assess the feasibility of quantifying liver iron concentration (LIC) using R_2^* and quantitative susceptibility mapping (QSM) at a high field strength of 7T.

Methods: Five different concentrations of Fe-dextran were injected into twelve mice to produce various degrees of liver iron overload. After the mice were sacrificed, blood and liver samples were harvested. Ferritin ELISA assay and inductively coupled plasma mass spectrometry were performed to quantify serum ferritin concentration and LIC. Multi-echo gradient echo MRI was conducted to estimate R_2^* and the magnetic susceptibility of each liver sample through complex non-linear least squares fitting and a morphology enabled dipole inversion method, respectively.

Results: Average estimates of serum ferritin concentration, LIC, R_2^*, and susceptibility all show good linear correlations with injected Fe-dextran concentration; however, the standard deviations in the estimates of R_2^* and susceptibility increase with injected Fe-dextran concentration. Both R_2^* and susceptibility measurements also show good linear correlations with LIC (R^2=0.78 and R^2=0.91, respectively), and a susceptibility-to-LIC conversion factor of 0.829 ppm/(mg/g wet) is derived.

Conclusion: The feasibility of quantifying LIC using MR-based R_2^* and QSM at a high field strength of 7T is demonstrated. Susceptibility quantification, which is an intrinsic property of tissues and benefits from being field strength independent, is more robust than R_2^* quantification in this ex vivo study. A susceptibility-to-LIC conversion factor is presented that agrees relatively well with previously published QSM derived results obtained at 1.5T and 3T.

Introduction

The liver is the primary organ for iron storage. However, humans do not have physiologically regulated means of excreting excess iron from the body, and therefore, accumulation of iron or iron overload occurs in the liver when the body absorbs more iron than it physiologically needs and naturally excretes. Chronic blood transfusions, which are often necessary for patients with diseases such as sickle cell anemia, thalassemia, and various cancers, are the most common cause of liver iron overload and may lead to high levels of liver iron concentration (LIC) [1-6], and although less common, diseases such as hereditary hemochromatosis, hepatitis C, alcoholic liver disease, and cirrhosis may also lead to high levels of LIC [1, 7, 8]. LIC has been shown to correlate well with total body iron content [1, 9, 10], but not only does excessive iron in the body lead to adverse effects in the liver, it may also lead to heart complications [1, 11, 12]. Removing excess iron from the body using iron chelation treatments is possible [1, 13-15]; however, methods to non-invasively monitor these treatments are highly desirable to ensure over- or under-treatment does not occur and healthy iron levels are maintained.

Despite its invasive nature and predisposition to large variations, the current reference standard for the quantification of LIC is liver biopsy [1, 7]. Many non-invasive medical imaging technologies, such as ultrasound and computed tomography, are either unable to quantify LIC or suffer from the use of ionizing radiation. However, magnetic resonance imaging (MRI) is a non-invasive imaging technique that has proven to be highly sensitive to the presence of iron and doesn’t suffer from the same radiation concerns.

Many MR-based methods for quantifying LIC have been proposed, including signal ratio [1, 16-18], relaxometry [1, 19-25], and susceptometry [1, 9, 26-34] techniques. Although longitudinal relaxation techniques have been proposed [12, 25], the transverse relaxation rate (R_2) and effective transverse relaxation rate (R_2^*) have become the most widely adopted measures of LIC, as they are more sensitive to increases in iron concentration [1, 12, 25]. MRI spin echo protocols used to acquire datasets for R_2 quantification are often very time consuming, and contradictory linear and non-linear relationships between R_2 and LIC have been reported [20, 22, 24, 35-38]. This limits the feasibility of quantifying LIC in vivo unless a respiratory motion correction is applied, and the inconsistency among reports is concerning. Advantageously, gradient echo protocols used to quantify R_2^* are generally much shorter, and the relationship between R_2^* and LIC has consistently been shown to be linear [19-23, 35]. To accurately quantify R_2^* in the liver though, many factors need to be considered and accounted for, such as, the presence of fat and its spectral multi-peak complexity [39-44], phase errors arising due to eddy currents [45], and static field inhomogeneity [43, 46-48]. Many different methods have been developed to account for these factors; however, reproducibility across methods, so far, has been poor, as many conflicting R_2^*-to-LIC conversion factors (slope of the best-fit line) have been reported [19-21, 23, 35]. The dependence of R_2^* on the static magnetic field strength also must be considered if a standardized R_2^*-to-LIC conversion factor is to be derived.

Magnetic susceptibility is an inherent property of tissues that, unlike R_2^*, is independent of the magnetic field strength and, similar to R_2^*, increases with increasing LIC. Superconducting quantum interference devices are able to accurately measure magnetic susceptibility in the liver [9, 26, 28, 29], and LIC quantification using these devices has been shown to correlate well with biopsy LIC measurements [29]. However, the operation of these devices is expensive, and their availability is extremely limited. MRI, being widely available and significantly more cost effective, can also be used to quantify magnetic susceptibility through a procedure known as quantitative susceptibility mapping (QSM), which can be performed on the same 3D gradient echo datasets acquired to quantify R_2^*. Recently, linear relationships between magnetic susceptibility obtained using QSM and LIC measurements have been reported [27, 49, 50], and a good linear correlation between susceptibility measurements obtained using QSM and a superconducting quantum interference device has been observed [26]. However, studies comparing LIC measurements and liver susceptibility measurements obtained using QSM have mostly been performed at low field strengths (e.g. 1.5T and 3T), and the reproducibility of QSM liver susceptibility quantification has not been studied. This raises the question as to whether or not LIC quantification using QSM is reproducible and whether or not a standardized, field independent susceptibility-to-LIC conversion factor can be derived.

In this paper, the feasibility of detecting varying degrees of iron overload and quantifying LIC using R_2^* and QSM at a high field strength of 7T using a mouse model is evaluated and compared to previously published results obtained for human studies performed at lower magnetic field strengths. Previously, only relaxometry methods have been evaluated using a mouse model of liver iron overload [51, 52], and to the best of the authors' knowledge, the work presented here is the first to use a mouse model for the assessment of liver iron overload using QSM.

Methods

Animal Preparation and Iron Overloading

All animal experiments were conducted in accordance with the University of Georgia Animal Care and Use Committee guidelines and the NIH Guide for the Care and Use of Laboratory Animals. Six-week-old female Balb/C mice were housed in Innovive Disposable Micro-Isolators in a room maintained at 20 ± 1 ^{o}C with 12-hour light and dark cycles. Diet and water were available *ad libitum*. Twelve mice were randomly assigned into six groups (n=2 per group) to received various degrees of iron overloading based on a dextran model [53, 54], which has been shown to cause Kupffer macrophages to be loaded with phagocytized iron dextran [14, 55, 56]. A dextran model was chosen as pharmacological (parenteral), opposed to dietary (enteral), overload with iron dextran may delay hepcidin activation [53], and parenteral administration is more easily performed in comparison to gene manipulation models [57-59]. Mice have also been shown to be able to tolerate high doses of parenterally administered iron dextran [54], and parenteral administered iron dextran is processed similarly to hemoglobin iron, which has been shown not to cause cardiac dysfunction or pathological ventricular remodeling in mice [60].

Groups 1-5 were injected with concentrations of 150, 100, 75, 50, and 25 mg/kg (Fe/mouse mass), respectively, of dextran solutions (200μL) on Day 1 using single tail vein injections, while Group 6 received saline. The mice were then started on iron-deficient powder diets *ad libitum* and were monitored for one week to ensure iron overload levels remained constant based on serum ferritin concentration measurements. On day 8, mice were euthanized by CO_2 overdose, and the livers were harvested, rinsed with fresh phosphate-buffered saline, blotted dry with Whatman filter paper, and then weighed. The livers were sectioned into two approximately equal halves. One half was snap-frozen in liquid nitrogen and later used to quantify LIC via inductively coupled plasma mass spectrometry (ICP-MS), and the other half was fixed in neutral buffered formalin and later used for MRI experiments and histology.

Serum Ferritin Concentration, ICP-MS LIC Measurements, and Histology

Blood from each mouse was directly collected via cardiac puncture immediately following CO_2 overdose and added to microcentrifuge tubes to separate out the serum. Final serum ferritin concentration was measured using a colorimetric mouse ferritin ELISA assay

(Immunology Consultants Laboratory, Inc.). The absorbance at 450 nm was used to determine serum ferritin concentration according to the manufacturer's instruction.

For ICP-MS measurements, liver samples (0.5 g) were digested in 9 mL of concentrated nitric acid and 3 mL hydrofluoric acid for 15 minutes. More specifically, each liver tissue sample in acid was placed in an inert polymeric microwave vessel and sealed prior to placing it in the laboratory microwave system. The temperature in the vessel was allowed to reach 180 ± 5 ºC in approximately 5.5 minutes and was maintained at 180 ± 5 ºC for an additional 9.5 minutes to allow for complete digestion of the sample. After cooling, the vessel content was filtered, centrifuged, decanted, and diluted to volume before quantifying iron concentration by ICP-MS. Note that all final tissue samples analyzed by ICP-MS, as well as iron standards used to calibrate (obtained from Sigma-Aldrich), contained 1% HNO_3.

For histopathological evaluation, liver samples were embedded in paraffin, sectioned into 5 μm slices, stained with Perls' Prussian Blue, and photomicrographed according to standard procedure.

NMR Spectroscopy Experiments

A non-iron overloaded liver sample was harvested using the above described methods and was prepared for NMR spectroscopy using a standard NMR procedure [61]. The ^{1}H NMR spectrum was acquired with a 600 MHz Varian Inova Spectrometer using a standard (rectangular excitation pulse followed by immediate acquisition) water suppressed ^{1}H NMR pulse sequence (spectral width sw = 6600 Hz, flip angle FA = 90 degrees, pulse width pw = 6.3 μs, repetition time TR = 2s, and 16 acquisitions for averaging). Assuming a 9-peak fat spectral model [39], the relative concentrations of the fat peaks were determined by performing multiplet analysis using

MNOVA (Mestrelab Research) to generate a mouse liver fat spectral model to be used in the post-processing field map and R_2^* estimation methods described below.

MRI Experiments

The liver samples harvested for MRI were evenly spaced out in cylindrical tubes (28 mm in diameter, 114 mm in length) filled with agar gelatin. Using a 7T Varian Magnex MRI Scanner, the tubes were scanned with a 38 mm volume coil using a 3D multi-gradient-echo sequence with a unipolar readout gradient (FA = 5 degrees, TR = 25 ms, initial echo time TE_i = 1.46 ms, echo spacing ΔTE = 0.58 ms, 12 echoes, field of view FOV = 85x35x35 mm, a matrix size of 64^3, and 6 acquisitions for averaging).

MRI Post-Processing Methods

In gradient echo based chemical shift encoded MRI, the MR signal of a voxel containing water and fat, acquired using a series of *n* echoes, is given by

$$s(t_n) = (\rho_{\mathrm{W}} + \rho_{\mathrm{F}} \textstyle\sum_{m=1}^{M} \alpha_m e^{i2\pi f_m t_n}) e^{i2\pi f_B t_n} e^{-R_2^* t_n} \qquad (3.1)$$

where t_n is the *n*th echo time, ρ_W and ρ_F are the water and fat signal densities, α_m is the relative concentration and $f_m = \gamma B_0 \sigma_m$ is the frequency shift relative to water of the *m*th fat peak with γ representing the proton gyromagnetic ratio, B_0 representing the static magnetic field strength, and σ_m representing the chemical shift of the *m*th fat peak with respect to water (4.7 ppm), and f_B is the frequency shift relative to B_0 that arises due to magnetic field inhomogeneities. Due to the strong paramagnetic nature of iron, f_B is highly dependent on the presence of iron in the local area. A common R_2^* for all chemical species was assumed in this work, as it has been shown that, even for cases of iron overload and high hepatic fat concentrations, accurate measurements can be obtained [44, 62-64].

First, an initial estimate of f_B was obtained using a 3D graphcut method [48, 65] to perform spatially regularized complex non-linear least squares (NLLS) fitting of the signal. After the field map component was removed from the signal, an initial estimate of R_2^* was obtained on a voxel-by-voxel basis from the remaining signal using variable projection to perform complex NLLS fitting [47, 66]. The final estimates of f_B and R_2^* were obtained by using the initial estimates and a Levenberg-Marquardt algorithm (Matlab, The Mathworks, Matwick, MA) to perform complex NLLS fitting of the signal on a voxel-by-voxel basis [27], as complex NLLS fitting of the signal has been shown to outperform other methods in the presence of noise [42, 62]. Note that the methods described here assume α_m and f_m in the signal model (Eq. (3.1)) to be known as *a priori* information, and ρ_W and ρ_F were estimated simultaneously along with the final estimates of R_2^* and f_B.

Using the final f_B estimate, QSM was then performed, which consists of two main steps: 1) removal of the background magnetic field and 2) calculation of the susceptibility from the remaining local field through dipole inversion [67]. The background field is generally assumed to be harmonic and can, therefore, be removed by solving Laplace’s equation [67, 68]. However, the solution to Laplacian’s equation loses uniqueness at the boundaries of the region of interest [68]. The boundaries for each MR dataset were defined by manually drawing masks around the cylindrical tubes containing the liver samples that excluded background air. Then, by assuming simple boundary value conditions, the background field was removed from the final f_B estimate by solving Laplace’s and Poisson’s equations using a Laplacian boundary value method [68] to solve the partial differential equations using a full multigrid finite difference algorithm [69].

After removing the background field, the susceptibility can be determined from the remaining local field by deconvolving the local field with a unit dipole field; however, the inversion problem is ill-posed [67, 70, 71]. In this work, the ill-posed problem was solved using a morphology enabled dipole inversion method [71] to construct a L_1-norm minimization problem that incorporates structural information from the magnitude images. Final susceptibility estimates were obtained by finding the solution to the L_1-norm problem using an iterative conjugate gradient method [72] with the solution to the deconvolution without the L_1-regularization term serving as the initial guess. A flowchart depicting the above-described MRI post-processing procedure is presented in Figure 3.1.

Using the NMR derived mouse liver fat spectral model and the above-described post-processing methods, R_2^* and susceptibility maps were generated for each MR dataset. For each liver sample, the average and standard deviation of measurements obtained throughout a region-of-interest that covered the full volume of the liver sample, while avoiding voxels with partial volume effects, was determined. The susceptibility measurements were determined in reference to the average susceptibility of the agar gelatin background on a slice-by-slice basis.

Results

Serum Ferritin Concentration, ICP-MS LIC Measurements, and Histology

Measured serum ferritin concentrations and ICP-MS LIC measurements are compared to the injected Fe-dextran concentrations using linear regression analysis (Figure 3.2a,b). Both measurements increase linearly with increasing injected Fe-dextran concentration and show good linear correlations (R^2=0.95 and R^2=0.91, respectively). The injected Fe-dextran concentration-to-LIC conversion factor was determined to be 0.0386 (mg/g wet)/(mg/kg) (Figure 3.2b). A good linear correlation is also observed between the serum ferritin concentration and ICP-MS LIC measurements (R^2=0.88 and serum ferritin concentration-to-LIC conversion factor = 8006 (ng/ml)/(mg/g wet)) (Figure 3.2c).

It is also observed in the Prussian blue stained liver sections (Figure 3.3) that iron accumulates in Kupffer macrophages as expected, and that this accumulation occurs non-homogeneously throughout the liver tissue.

NMR Spectroscopy Experiment

The water suppressed ^{1}H NMR spectrum for a non-iron overloaded mouse liver is shown in Figure 3.4, which displays the chemical shifts (σ) in reference to water (4.7 ppm) and the measured relative concentrations (α) of each of the 9 fat resonance peaks. The resonance peak associated with total choline concentration, which includes choline and its derivatives phosphocholine and glycerophosphocholine, is also labeled [73-75]. The 9-peak mouse liver fat spectral model derived here differs from previously published human liver models [39, 76-78]. When estimating R_2^* and f_B from MRI data, this mouse model (α_m and $f_m = \gamma B_0 \sigma_m$) was used in the post-processing methods as *a priori* information.

MR-Based LIC Quantification

Quantitative measurements of R_2^* and susceptibility for all liver samples are displayed in Figure 3.5. The average R_2^* values measured throughout each liver appear to increase linearly with injected Fe-dextran concentration up to a concentration of 50 mg/kg (Figure 3.5a); a slight loss in linearity is then observed for injected concentrations between 50-100 mg/kg. A continuous, positive, linear dependency on the injected Fe-dextran concentration, however, is observed in the average susceptibility measurements (Figure 3.5b). The standard deviations of the R_2^* and susceptibility measurements obtained throughout each liver also tend to increase with increasing injected Fe-dextran concentration.

The changes in the averages and standard deviations of the measurements can be more easily seen by examining their distributions (Figure 3.5c,d). For injected concentrations of 50-100 mg/kg, the R_2^* distributions significantly overlap with each other, while clear shifts between other concentrations are observed. The susceptibility distributions, conversely, show clear shifts between all injected Fe-dextran concentrations. It is also observed that the distributions of both R_2^* and susceptibility become more spread out for higher injected concentrations, indicating larger standard deviations.

LIC measurements obtained using ICP-MS are compared to the R_2^* and susceptibility measurements using linear regression analysis (Figure 3.6a,b). Good correlations between ICP-MS LIC measurements and the average R_2^* and susceptibility measurements are observed (R^2=0.78 and R^2=0.91, respectively), and R_2^*-to-LIC and susceptibility-to-LIC conversion factors of 372.2 s^{-1}/(mg/g wet) and 0.829 ppm/(mg/g wet) are derived. A good linear correlation is also observed between the average R_2^* and susceptibility measurements (R^2=0.90 and susceptibly-to-R_2^* conversion factor = 0.0020 ppm/s^{-1}) (Figure 3.6c).

The overall average susceptibility of the agar gelatin background, in which liver susceptibility measurements were made in reference to on a slice-by-slice basis, was found to be -0.050 ppm, and the average measured proton density fat fractions of the liver samples varied within the range of 4-18%.

An MRI magnitude image and its corresponding R_2^* and quantitative susceptibility maps for a representative slice containing two excised livers from mice that were injected with differing Fe-dextran concentrations are shown in Figure 3.7. Clear differences in signal intensity,

R_2^*, and susceptibility can be seen between the two livers. It is also observed that the spatial distributions of R_2^* and susceptibility are non-homogeneous.

Discussion and Conclusion

The observed increases in the average R_2^* and susceptibility measurements suggest that iron accumulates approximately linearly in the liver with increasing injected Fe-dextran concentration, which is confirmed with ICP-MS LIC measurements (Figure 3.2b). This demonstrates the feasibility of the proposed methodology to create a controlled iron overload in the mouse liver, and the injected Fe-dextran concentration-to-LIC conversion factor can further be used to generate desired approximate LICs in future studies. However, the observed increases in the standard deviations of the R_2^* and susceptibility measurements and their observed spatial distributions suggest that the accumulation of iron throughout the liver is non-homogeneous and that this inhomogeneity increases with higher injected Fe-dextran concentration, which is confirmed by histology (Figure 3.3). These observed increases and spatial distributions may also be due in part to noise more strongly influencing the estimates for livers with higher measured LICs, as the MR signal decays more rapidly leading to reduced SNR of the acquired data, especially for later echoes.

The good linear relationships between serum ferritin measurements and injected Fe-dextran concentration and ICP-MS measurements (Figure 3.2a,c) suggest that serum ferritin measurements correlate well with LIC, which has previously been reported [1, 79]. Although serum ferritin concentration assays are commonly used to screen for iron overload in clinical settings, excessive alcohol use, viral hepatitis, and other systemic inflammatory disorders can injure hepatocytes and elevate serum ferritin levels [1, 9]. Therefore, these measurements may be misleading and are not always good quantitative measures of LIC.

However, in this work, MR-based R_2^* and susceptibility techniques are shown to be good quantitative measures of LIC, and the feasibility of quantifying LIC at a high field strength of 7T is demonstrated. Approximately linear correlations between the estimates of these parameters and ICP-MS LIC measurements are observed (Figure 3.6a,b), which agrees with previously published results from experiments performed at lower field strengths (e.g. 1.5T and 3T) [19-23, 27, 35, 49, 50]. However, a better linear correlation with LIC is observed for susceptibility (R_2=0.91) than for R_2^* (R_2=0.78), which is likely due to the slight loss of linearity in the R_2^* measurements for injected Fe-dextran concentrations of 50-100 mg/kg (Figure 3.5a). The susceptibility measurements also tend to have a smaller average standard deviation to slope ratio than the R_2^* measurements indicating that smaller changes in LIC can be measured without significant overlap in the distributions of the measurements. This suggests that R_2^* quantification may be more sensitive due to factors such as, background field perturbations, static field inhomogeneities, the choice of quantification method, and acquisition parameter selection [1], while susceptibility quantification through QSM is more robust.

Due to the high sensitivity of R_2^* quantification and the fact that R_2^* is dependent on field strength, the development of a standardized R_2^*-to-LIC conversion factor is difficult to obtain. Many studies have demonstrated good reproducibility of R_2^* estimations using various acquisition parameters [1, 80-84], and estimates of R_2^* obtained at 1.5T and 3T have been shown to differ by a factor of two when using consistent acquisition parameters and quantification methods [85]. However, agreement across studies that have used different quantification methods has been poor, as many different R_2^*-to-LIC conversion factors have been reported [19-21, 23, 35], even for studies performed at the same field strengths. Although this limits the ability to make direct comparisons of R_2^*-to-LIC conversion factors across studies, these differences can be corrected through the use of method specific calibration curves [86].

Good linear correlations between R_2^* and susceptibility have also been reported [26, 27, 87], but with various susceptibility-to-R_2^* conversion factors. Factors obtained at 1.5T and 3T using the same quantification method have also been shown to differ by a factor of two [27], but susceptibility-to-R_2^* conversion factors also suffer from the sensitivity and poor reproducibility of R_2^* across quantification methods.

Susceptibility is an intrinsic property of tissues that is independent of field strength, and this ex vivo study suggests that its quantification may be more robust than R_2^* quantification. Therefore, a standardized susceptibility-to-LIC conversion factor should be feasible to obtain, and the direct comparison of derived conversion factors across studies should be possible without the need for method specific calibration curves. Langkammer et al. [88] derived a factor of 0.89 ppm/(mg/g wet) by performing QSM on MR datasets acquired at 3T and comparing it to ICP-MS measurements in post mortem human brains. Using this factor, Sharma et al. [27] converted measured susceptibility values in the human liver obtained using QSM to LIC values. Once the susceptibility values were converted to LIC values, linear regression analysis was performed between the converted QSM-LIC values and acquired Ferriscan-LIC measurements. Using the same conversion factor by Langkammer et al. [88], the slopes from Sharma et al.'s [27] linear regression analysis can be converted to susceptibility-to-LIC conversion factors, and upon making this conversion, results of 0.703 ppm/(mg/g wet) for 1.5T and 0.730 ppm/(mg/g wet) for 3T are obtained. The susceptibility-to-LIC conversion factor derived in this work of 0.829 ppm/(mg/g wet) (Figure 3.6b) is in relatively good agreement with the factors derived by Sharma et al. [27] and Langkammer et al. [88]. The slight differences observed between the susceptibility-to-LIC conversion factors may be due to differences in the accuracies of the chosen QSM techniques, which have been shown to lead to different degrees of underestimation [67], and/or due to differences in the spatial resolution of the acquired data, which has been shown to effect QSM estimates [89, 90]. Two recent studies using QSM have similarly reported good linear correlations between susceptibility and LIC [49, 50]; however, they did not present susceptibility-to-LIC conversion factors.

Iron in the body is primarily found in the storage complexes hemosiderin and ferritin, which based on the Curie-Weiss law, have reported theoretical susceptibility concentrations in the range of 1.1-1.6 ppm/(mg/g wet) [22, 88, 91, 92], which are larger than the susceptibility-to-LIC conversion factors discussed in this work. Recent work quantifying susceptibility in the human liver has also reported smaller measurements obtained using QSM in comparison to measurements obtained using a superconducting quantum interference device [26]. This suggests that the above discussed susceptibility-to-LIC conversion factors derived using QSM may be underestimated. Sharma et al. [26] suggested that the use of a relatively large slice thickness in comparison to the in-plane resolution may have contributed to the QSM underestimation observed in their work. All three susceptibility-to-LIC conversion factors discussed above were estimated from acquired data with slice thicknesses that were at least 2.4 times greater than the in-plane resolution. Therefore, this may be a contributing factor to the underestimations.

Although the presence and spectral complexity of fat, as well as the static field inhomogeneity, was accounted for in this work, confounding factors related to phase errors [45] were not addressed. Upon examination of the phase within all samples and within the agar gelatin, no significant deviations from linear behavior were observed, which suggests that no significant phase errors were arising due to eddy currents.

The work presented here does suffer from a few limitations though, including a small sample size and relatively small LIC concentrations. Quantitative measurements were only performed on twelve mice (six groups of n=2), all of which had measured LICs of less than 0.8 mg/g of wet tissue. Other studies conducted on human liver tissues have reported significantly higher LIC measurements, with a maximum around 7 mg/g of wet tissue [19-22, 24, 27, 37, 38]. Therefore, in order to more accurately develop a standardized susceptibility-to-LIC conversion factor, a larger sample size covering a wider range of LIC values should be evaluated. Nevertheless, the results presented in this work demonstrate the feasibility of accurately detecting very small changes in LIC in ex vivo mouse livers using a high field strength of 7T.

LIC quantification, especially for cases of severe iron overload, would presumably be less challenging at lower clinical field strengths (e.g. 1.5T and 3T) due to slower signal decay (smaller R_2^*) in comparison to that at a higher field of 7T. However, high field iron quantification is becoming increasingly important as it allows for pre-clinical animal studies, for which biopsy validation is possible, and for human neural imaging, as certain neurodegenerative diseases and micro-bleeding caused by traumatic brain injuries can lead to relatively small iron deposits or changes in iron concentration that can be more easily measured using higher fields. However, the study presented here only demonstrates the high field (e.g. 7T) feasibility of quantifying small differences in iron concentration in ex vivo mouse livers. In vivo LIC quantification at high fields will likely be more challenging due to faster signal decay (larger R_2^*) caused by additional factors such as blood flow and respiratory motion. Although this study suggests that susceptibility quantification using QSM may be more robust than R_2^* quantification, these additional factors, as well as changes in the geometry of the iron deposits, may lead to greater challenges for in vivo QSM than for R_2^*. Therefore, further in vivo validation studies are necessary.

In this work, twelve echoes of MR data was acquired resulting in a scan time of about four minutes per acquisition. However, in vivo human studies seek to minimize scan times so that data can be acquired in single breath holds. Using Cramer-Rao bound analysis, Hernando et al. [42] found that the theoretical noise performance of R_2^* estimation doesn't significantly improve beyond six echoes, except for cases of low R_2^*. Since the non-iron overloaded livers (Group 6) had average measured R_2^* values of approximately 40 s^{-1} and highly accurate quantification was desired for all R_2^* and susceptibility estimations, all twelve acquired echoes were used for MRI post-processing procedures. Future work will seek to use the proposed methodology to quantify LIC using an in vivo mouse model and explore the feasibility of monitoring various iron chelation treatments. These studies will likely require reduced scan times, and therefore, a reduced number of echoes. However, confounding factors such as blood flow and respiratory motion should compromise R_2^* values with a reduced number of echoes.

In conclusion, the work presented here demonstrates the feasibility of quantifying LIC using MR-based R_2^* and QSM techniques at a high field strength of 7T. Susceptibility quantification, which is an intrinsic property of tissues and benefits from being field strength independent, is found to be more robust and more comparable across studies than R_2^* quantification, and a susceptibility-to-LIC conversion factor is presented that agrees relatively well with previously published QSM derived results obtained at 1.5T and 3T [27, 88].

References

1. Hernando, D., et al., *Quantification of liver iron with MRI: state of the art and remaining challenges.* Journal of Magnetic Resonance Imaging, 2014. **40**(5): p. 1003-1021.

2. Harmatz, P., et al., *Severity of iron overload in patients with sickle cell disease receiving chronic red blood cell transfusion therapy.* Blood, 2000. **96**(1): p. 76-79.
3. Siegelman, E.S., D.G. Mitchell, and R.C. Semelka, *Abdominal iron deposition: metabolism, MR findings, and clinical importance.* Radiology, 1996. **199**(1): p. 13-22.
4. Prati, D., et al., *Clinical and histological characterization of liver disease in patients with transfusion-dependent beta-thalassemia. A multicenter study of 117 cases.* Haematologica, 2004. **89**(10): p. 1179-1186.
5. Eng, J. and J.D. Fish, *Insidious iron burden in pediatric patients with acute lymphoblastic leukemia.* Pediatric blood & cancer, 2011. **56**(3): p. 368-371.
6. Nottage, K., et al., *Trends in transfusion burden among long-term survivors of childhood hematological malignancies.* Leukemia & lymphoma, 2013. **54**(8): p. 1719-1723.
7. Batts, K.P., *Iron overload syndromes and the liver.* Modern Pathology, 2007. **20**(1s): p. S31.
8. Olynyk, J.K., et al., *Duration of hepatic iron exposure increases the risk of significant fibrosis in hereditary hemochromatosis: a new role for magnetic resonance imaging.* The American journal of gastroenterology, 2005. **100**(4): p. 837-841.
9. Brittenham, G.M. and D.G. Badman, *Noninvasive measurement of iron: report of an NIDDK workshop.* Blood, 2003. **101**(1): p. 15-19.
10. Angelucci, E., et al., *Hepatic iron concentration and total body iron stores in thalassemia major.* New England Journal of Medicine, 2000. **343**(5): p. 327-331.
11. Sempos, C.T., R.F. Gillum, and A.C. Looker, *Iron and heart disease*, in *Preventive Nutrition*. 1997, Springer. p. 181-192.
12. Wood, J.C., et al., *Cardiac iron determines cardiac T2*, T2, and T1 in the gerbil model of iron cardiomyopathy.* Circulation, 2005. **112**(4): p. 535-543.
13. Poggiali, E., et al., *An update on iron chelation therapy.* Blood Transfusion, 2012. **10**(4): p. 411.
14. Liu, Z., et al., *Enzymatically Biodegradable Polyrotaxane-Deferoxamine Conjugates for Iron Chelation.* ACS applied materials & interfaces, 2016. **8**(39): p. 25788.
15. Liu, Z., et al., *Oxidation-Induced Degradable Nanogels for Iron Chelation.* Scientific reports, 2016. **6**.
16. Gandon, Y., et al., *Hemochromatosis: diagnosis and quantification of liver iron with gradient-echo MR imaging.* Radiology, 1994. **193**(2): p. 533-538.
17. Ernst, O., et al., *Hepatic iron overload: diagnosis and quantification with MR imaging.* AJR. American journal of roentgenology, 1997. **168**(5): p. 1205-1208.
18. Bonkovsky, H.L., et al., *Hepatic iron concentration: noninvasive estimation by means of MR imaging techniques.* Radiology, 1999. **212**(1): p. 227-234.
19. Chan, W.C., et al., *R2* as a surrogate measure of ferriscan iron quantification in thalassemia.* Journal of Magnetic Resonance Imaging, 2014. **39**(4): p. 1007-1011.
20. Wood, J.C., et al., *MRI R2 and R2* mapping accurately estimates hepatic iron concentration in transfusion-dependent thalassemia and sickle cell disease patients.* Blood, 2005. **106**(4): p. 1460-1465.
21. Hankins, J.S., et al., *R2* magnetic resonance imaging of the liver in patients with iron overload.* Blood, 2009. **113**(20): p. 4853-4855.

22. Ghugre, N.R. and J.C. Wood, *Relaxivity-iron calibration in hepatic iron overload: Probing underlying biophysical mechanisms using a Monte Carlo model.* Magnetic resonance in medicine, 2011. **65**(3): p. 837-847.
23. Garbowski, M.W., et al., *Calibration of Improved T2* Method for the Estimation of Liver Iron Concentration in Transfusional Iron Overload*. 2009, Am Soc Hematology.
24. Pierre, T.G.S., et al., *Noninvasive measurement and imaging of liver iron concentrations using proton magnetic resonance.* Blood, 2005. **105**(2): p. 855-861.
25. Henninger, B., et al., *Evaluation of MR imaging with T1 and T2* mapping for the determination of hepatic iron overload.* European radiology, 2012. **22**(11): p. 2478-2486.
26. Sharma, S.D., et al., *MRI-based quantitative susceptibility mapping (QSM) and R2* mapping of liver iron overload: Comparison with SQUID-based biomagnetic liver susceptometry.* Magnetic resonance in medicine, 2017. **78**(1): p. 264-270.
27. Sharma, S.D., et al., *Quantitative susceptibility mapping in the abdomen as an imaging biomarker of hepatic iron overload.* Magnetic resonance in medicine, 2015. **74**(3): p. 673-683.
28. Brittenham, G.M., et al., *Magnetic-susceptibility measurement of human iron stores.* New England Journal of Medicine, 1982. **307**(27): p. 1671-1675.
29. Brittenham, G.M., et al. *Noninvasive methods for quantitative assessment of transfusional iron overload in sickle cell disease*. in *Seminars in hematology*. 2001. Elsevier.
30. Holt, R.W., *MRI susceptometry: theory and robustness of an external phantom method for measuring bulk susceptibility from MRI field echo phase reconstruction maps applied to human liver iron overload*. 1993, Case Western Reserve University.
31. Holt, R.W., et al., *MR susceptometry: an external-phantom method for measuring bulk susceptibility from field-echo phase reconstruction maps.* Journal of Magnetic Resonance Imaging, 1994. **4**(6): p. 809-818.
32. Chu, Z., et al., *MRI measurement of hepatic magnetic susceptibility—Phantom validation and normal subject studies.* Magnetic resonance in medicine, 2004. **52**(6): p. 1318-1327.
33. Hernando, D., et al., *Magnetic susceptibility as a B0 field strength independent MRI biomarker of liver iron overload.* Magnetic resonance in medicine, 2013. **70**(3): p. 648-656.
34. Taylor, B.A., et al., *Simultaneous field and R 2* mapping to quantify liver iron content using autoregressive moving average modeling.* Journal of Magnetic Resonance Imaging, 2012. **35**(5): p. 1125-1132.
35. Christoforidis, A., et al., *MRI assessment of liver iron content in thalassamic patients with three different protocols: comparisons and correlations.* European journal of haematology, 2009. **82**(5): p. 388-392.
36. Hitti, E., et al., *MRI quantification of splenic iron concentration in mouse.* Journal of Magnetic Resonance Imaging, 2010. **32**(3): p. 639-646.
37. Wang, Z.J., et al., *Evaluation of iron overload by single voxel MRS measurement of liver T2.* Journal of Magnetic Resonance Imaging, 2002. **15**(4): p. 395-400.
38. Wood, J.C., et al., *R2 and R2* are equally effective in evaluating chronic response to iron chelation.* American journal of hematology, 2014. **89**(5): p. 505-508.
39. Hamilton, G., et al., *In vivo characterization of the liver fat (1)H MR spectrum.* NMR Biomed, 2011. **24**(7): p. 784-90.

40. Hines, C.D., et al., *T(1) independent, T(2) (*) corrected chemical shift based fat-water separation with multi-peak fat spectral modeling is an accurate and precise measure of hepatic steatosis.* J Magn Reson Imaging, 2011. **33**(4): p. 873-81.
41. Meisamy, S., et al., *Quantification of hepatic steatosis with T1-independent, T2-corrected MR imaging with spectral modeling of fat: blinded comparison with MR spectroscopy.* Radiology, 2011. **258**(3): p. 767-75.
42. Hernando, D., J.H. Kramer, and S.B. Reeder, *Multipeak fat-corrected complex R2* relaxometry: theory, optimization, and clinical validation.* Magn Reson Med, 2013. **70**(5): p. 1319-31.
43. Hernando, D., et al., *R*(2) mapping in the presence of macroscopic B(0) field variations.* Magn Reson Med, 2012. **68**(3): p. 830-40.
44. Reeder, S.B., et al., *On the performance of T2* correction methods for quantification of hepatic fat content.* Magn Reson Med, 2012. **67**(2): p. 389-404.
45. Hernando, D., et al., *Addressing phase errors in fat-water imaging using a mixed magnitude/complex fitting method.* Magn Reson Med, 2012. **67**(3): p. 638-44.
46. Berglund, J. and J. Kullberg, *Three-dimensional water/fat separation and T2* estimation based on whole-image optimization--application in breathhold liver imaging at 1.5 T.* Magn Reson Med, 2012. **67**(6): p. 1684-93.
47. Hernando, D., et al., *Joint estimation of water/fat images and field inhomogeneity map.* Magn Reson Med, 2008. **59**(3): p. 571-80.
48. Hernando, D., et al., *Robust water/fat separation in the presence of large field inhomogeneities using a graph cut algorithm.* Magn Reson Med, 2010. **63**(1): p. 79-90.
49. Lin, H., et al., *Feasibility of Breath-hold Quantitative Susceptibility Mapping on Hepatic Iron quantification.* In Proceedings of the 25th Annual Meeting of ISMRM, Honolulu, USA, 2017.
50. Lin, H., et al., *Feasibility and grading performance of Quantitative Susceptibility Mapping for Hepatic Iron quantification.* In Proceedings of the 25th Annual Meeting of ISMRM, Honolulu, USA, 2017.
51. Song, R., et al., *Relationships between MR transverse relaxation parameters R* 2, R2 and R′ 2 and hepatic iron content in thalassemic mice at 1.5 T and 3 T.* NMR in Biomedicine, 2008. **21**(6): p. 574-580.
52. Jackson, L.H., et al., *Non-invasive MRI biomarkers for the early assessment of iron overload in a humanized mouse model of β-thalassemia.* Scientific Reports, 2017. **7**: p. srep43439.
53. Daba, A., et al., *Differences in activation of mouse hepcidin by dietary iron and parenterally administered iron dextran: compartmentalization is critical for iron sensing.* Journal of Molecular Medicine, 2013. **91**(1): p. 95-102.
54. Musumeci, M., et al., *Iron excretion in iron dextran-overloaded mice.* Blood Transfusion, 2014. **12**(4): p. 485.
55. Muir, A. and L. Golberg, *OBSERVATIONS ON SUBCUTANEOUS MACROPHAGES. PHAGOCYTOSIS OF IRON-DEXTRAN AND FERRITIN SYNTHESIS.* Experimental Physiology, 1961. **46**(4): p. 289-298.
56. Richter, G., *The iron-loaded cell--the cytopathology of iron storage. A review.* The American journal of pathology, 1978. **91**(2): p. 362.

57. Huang, F.W., et al., *A mouse model of juvenile hemochromatosis.* Journal of Clinical Investigation, 2005. **115**(8): p. 2187.
58. Zhou, X.Y., et al., *HFE gene knockout produces mouse model of hereditary hemochromatosis.* Proceedings of the National Academy of Sciences, 1998. **95**(5): p. 2492-2497.
59. Vidal, R., et al., *Expression of a mutant form of the ferritin light chain gene induces neurodegeneration and iron overload in transgenic mice.* Journal of Neuroscience, 2008. **28**(1): p. 60-67.
60. Musumeci, M., et al., *The C57BL/6 genetic background confers cardioprotection in iron-overloaded mice.* Blood Transfusion, 2013. **11**(1): p. 88.
61. Teng, Q., in *Structural Biology: Practical NMR Applications*. 2013, Springer: New York.
62. Hernando, D., Z.P. Liang, and P. Kellman, *Chemical shift-based water/fat separation: a comparison of signal models.* Magn Reson Med, 2010. **64**(3): p. 811-22.
63. Horng, D.E., et al., *Comparison of R2* correction methods for accurate fat quantification in fatty liver.* J Magn Reson Imaging, 2013. **37**(2): p. 414-22.
64. Horng, D.E., D. Hernando, and S.B. Reeder, *Quantification of liver fat in the presence of iron overload.* J Magn Reson Imaging, 2017. **45**(2): p. 428-439.
65. Boykov, Y., O. Veksler, and R. Zabih, *Fast approximate energy minimization via graph cuts.* IEEE Transactions on pattern analysis and machine intelligence, 2001. **23**(11): p. 1222-1239.
66. O'leary, D.P. and B.W. Rust, *Variable projection for nonlinear least squares problems.* Computational Optimization and Applications, 2013. **54**(3): p. 579-593.
67. Wang, Y. and T. Liu, *Quantitative susceptibility mapping (QSM): decoding MRI data for a tissue magnetic biomarker.* Magnetic resonance in medicine, 2015. **73**(1): p. 82-101.
68. Zhou, D., et al., *Background field removal by solving the Laplacian boundary value problem.* NMR in Biomedicine, 2014. **27**(3): p. 312-319.
69. Stüben, K. and U. Trottenberg, *Multigrid methods: Fundamental algorithms, model problem analysis and applications*, in *Multigrid methods*. 1982, Springer. p. 1-176.
70. Li, L. and J.S. Leigh, *Quantifying arbitrary magnetic susceptibility distributions with MR.* Magnetic resonance in medicine, 2004. **51**(5): p. 1077-1082.
71. Liu, J., et al., *Morphology enabled dipole inversion for quantitative susceptibility mapping using structural consistency between the magnitude image and the susceptibility map.* Neuroimage, 2012. **59**(3): p. 2560-2568.
72. Nocedal, J. and S.J. Wright, *Conjugate gradient methods.* Numerical optimization, 2006: p. 101-134.
73. Feng, J., et al., *Studies of secondary melanoma on C57BL/6J mouse liver using 1H NMR metabolomics.* Metabolites, 2013. **3**(4): p. 1011-1035.
74. Ghosh, S., et al., *Multivariate modelling with 1 H NMR of pleural effusion in murine cerebral malaria.* Malaria journal, 2011. **10**(1): p. 330.
75. Mao, J., et al., *A Selective NMR Method for Detecting Choline Containing Compounds in Liver Tissue: The 1H− 14N HSQC Experiment.* Journal of the American Chemical Society, 2010. **132**(49): p. 17349-17351.
76. Yu, H., et al., *Multiecho water-fat separation and simultaneous R2* estimation with multifrequency fat spectrum modeling.* Magn Reson Med, 2008. **60**(5): p. 1122-34.

77. Ren, J., et al., *Composition of adipose tissue and marrow fat in humans by 1H NMR at 7 Tesla.* J Lipid Res, 2008. **49**(9): p. 2055-62.
78. Wang, X., D. Hernando, and S.B. Reeder, *Sensitivity of chemical shift-encoded fat quantification to calibration of fat MR spectrum.* Magn Reson Med, 2016. **75**(2): p. 845-51.
79. Papakonstantinou, O., et al., *Quantification of liver iron overload by T2 quantitative magnetic resonance imaging in thalassemia: impact of chronic hepatitis C on measurements.* Journal of pediatric hematology/oncology, 1999. **21**(2): p. 142-148.
80. Tanner, M.A., et al., *Multi-center validation of the transferability of the magnetic resonance T2* technique for the quantification of tissue iron.* Haematologica, 2006. **91**(10): p. 1388-1391.
81. Westwood, M.A., et al., *Interscanner reproducibility of cardiovascular magnetic resonance T2* measurements of tissue iron in thalassemia.* Journal of Magnetic Resonance Imaging, 2003. **18**(5): p. 616-620.
82. Westwood, M.A., et al., *Intercentre reproducibility of magnetic resonance T2* measurements of myocardial iron in thalassaemia.* The international journal of cardiovascular imaging, 2005. **21**(5): p. 531-538.
83. Ramazzotti, A., et al., *Multicenter validation of the magnetic resonance T2* technique for segmental and global quantification of myocardial iron.* Journal of magnetic resonance imaging, 2009. **30**(1): p. 62-68.
84. Kirk, P., et al., *International reproducibility of single breathhold T2* MR for cardiac and liver iron assessment among five thalassemia centers.* Journal of Magnetic Resonance Imaging, 2010. **32**(2): p. 315-319.
85. Storey, P., et al., *R2* imaging of transfusional iron burden at 3T and comparison with 1.5 T.* Journal of Magnetic Resonance Imaging, 2007. **25**(3): p. 540-547.
86. Meloni, A., et al., *The use of appropriate calibration curves corrects for systematic differences in liver R2* values measured using different software packages.* British journal of haematology, 2013. **161**(6): p. 888-891.
87. Li, J., et al., *Quantitative Susceptibility Mapping (QSM) Overcomes R2* Confounding Factors for Measuring Liver Iron.* In Proceedings of the 25th Annual Meeting of ISMRM, Honolulu, USA, 2017.
88. Langkammer, C., et al., *Quantitative susceptibility mapping (QSM) as a means to measure brain iron? A post mortem validation study.* Neuroimage, 2012. **62**(3): p. 1593-1599.
89. Zhou, D., et al., *Accuracy of the QSM reconstruction: dependence on imaging resolution and B0 strength.* In Proceedings of the 3rd QSM Workshop on Phase Contrast and Quantitative Suceptibility Mapping, Durham, North Carolina, USA, 2014. .
90. Karsa, A., et al., *The effect of large slice thickness and spacing and low coverage on the accuracy of susceptibility mapping.* In Proceedings of the 24th Annual Meeting of ISMRM, Singapore, 2016.
91. Fischer, R., et al., *Monitoring Long-Term Efficacy of Iron Chelation Treatment with Biomagnetic Liver Susceptometry.* Annals of the New York Academy of Sciences, 2005. **1054**(1): p. 350-357.

92. Schenck, J.F., *The role of magnetic susceptibility in magnetic resonance imaging: MRI magnetic compatibility of the first and second kinds.* Medical physics, 1996. **23**(6): p. 815-850.

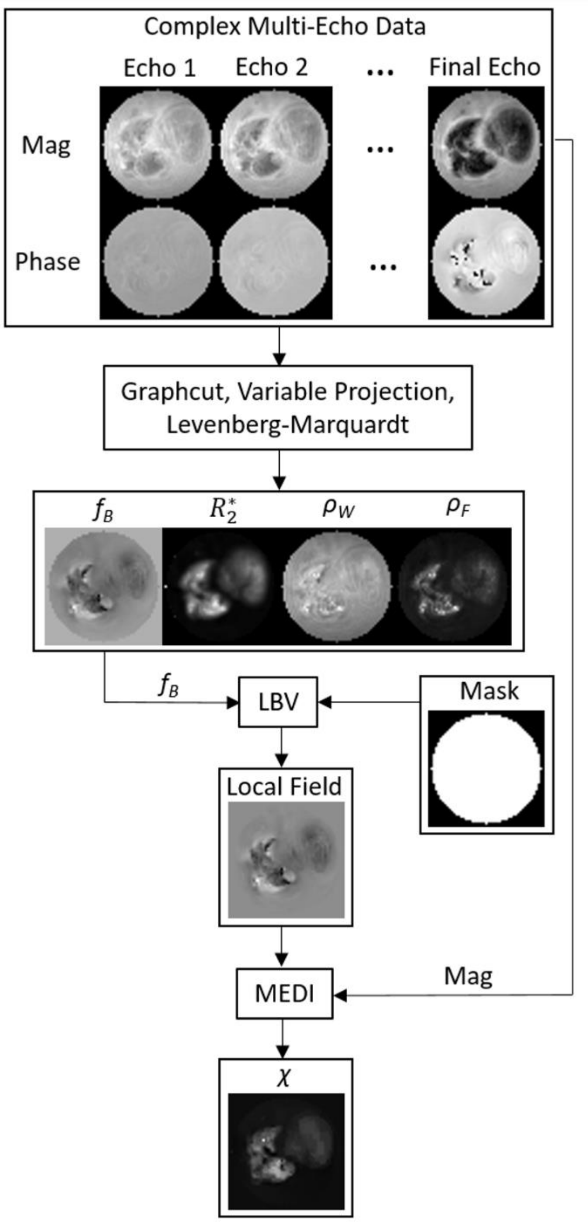

Figure 3.1: A flowchart depicting the MRI post-processing procedure used in this work. Using complex multi-gradient echo data, estimates of the field map (f_B), R_2^* map, and water and fat signal densities (ρ_W and ρ_F) were first estimated using a series of algorithms (graphcut, variable projection, and Levenberg-Marquardt) to perform complex non-linear least squares fitting of the MR signal. Using the field map and manually drawn boundary masks, the local field contribution of the field map was then determined using a Laplacian boundary value method (LBV). Finally, susceptibility (χ) maps were determined using the local field map, the magnitude images, and a morphology enabled dipole inversion method (MEDI).

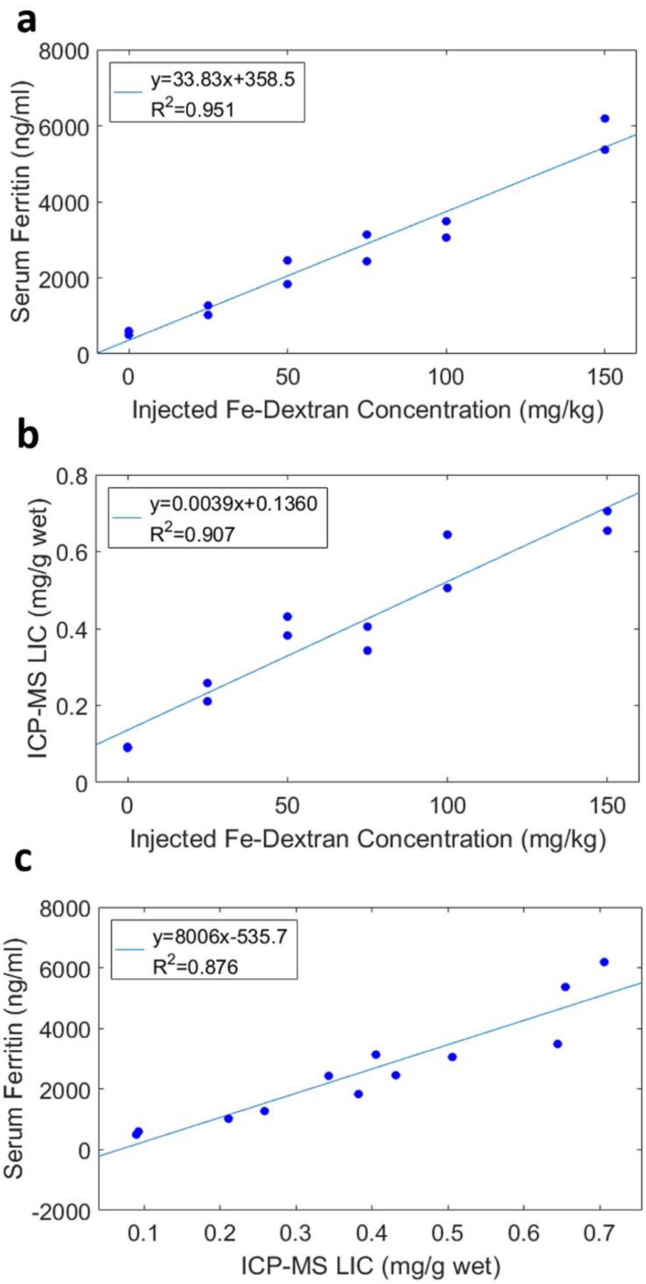

Figure 3.2: Linear regression plots for injected Fe-dextran concentration (six groups, n=2 per group) and serum ferritin measurements (a) and ICP-MS LIC measurements (b). Both serum ferritin concentration and ICP-MS LIC increase linearly with injected Fe-dextran concentration and show good linear correlations (R^2=0.95 and R^2=0.91, respectively). A good linear correlation is also observed between the serum ferritin concentration and ICP-MS LIC measurements (c).

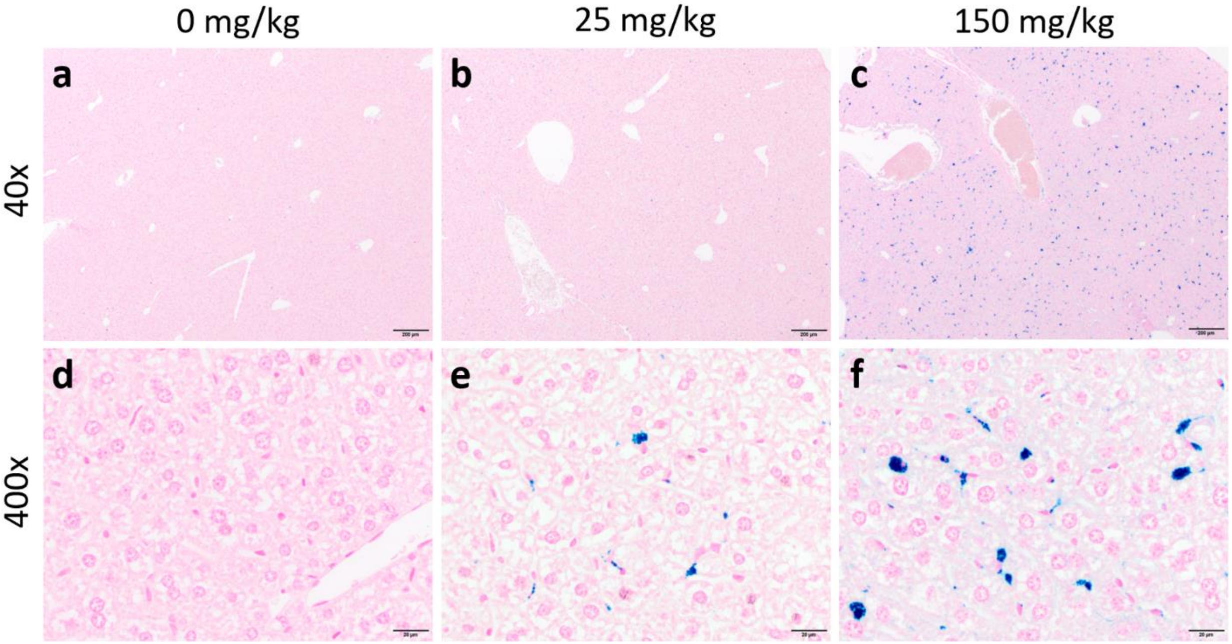

Figure 3.3: Photomicrographs of histological liver sections stained with Prussian blue at 40 (a-c, scale bar equals 200 µm) and 400 (d-f, scale bar equals 20 µm) times original magnification obtained from mice injected with 0 (a,d), 25 (b,e), and 150 mg/kg (c,f) concentrations (Fe/mouse mass) of saline-dextran solutions (200µL). Many scattered iron-containing Kupffer macrophages are observed in the mice injected with non-zero concentrations, and the degree of iron overloading increases with concentration. No iron deposits are observed in the mouse injected with a concentration of zero.

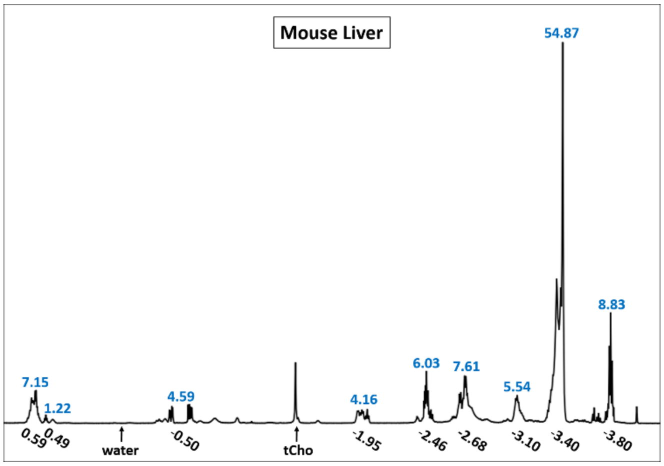

Figure 3.4: Acquired NMR water suppressed ^{1}H spectrum for a non-iron overloaded mouse liver. The locations of the 9 fat resonance peaks (ppm relative to water) and their measured relative concentrations (%) of the total fat concentration are provided below and above each peak, respectively. A larger non-fat peak located between -0.50 and -1.95 ppm is also observed and is likely associated with the total choline (tCho) concentration, which includes choline and its derivatives phosphocholine and glycerophosphocholine.

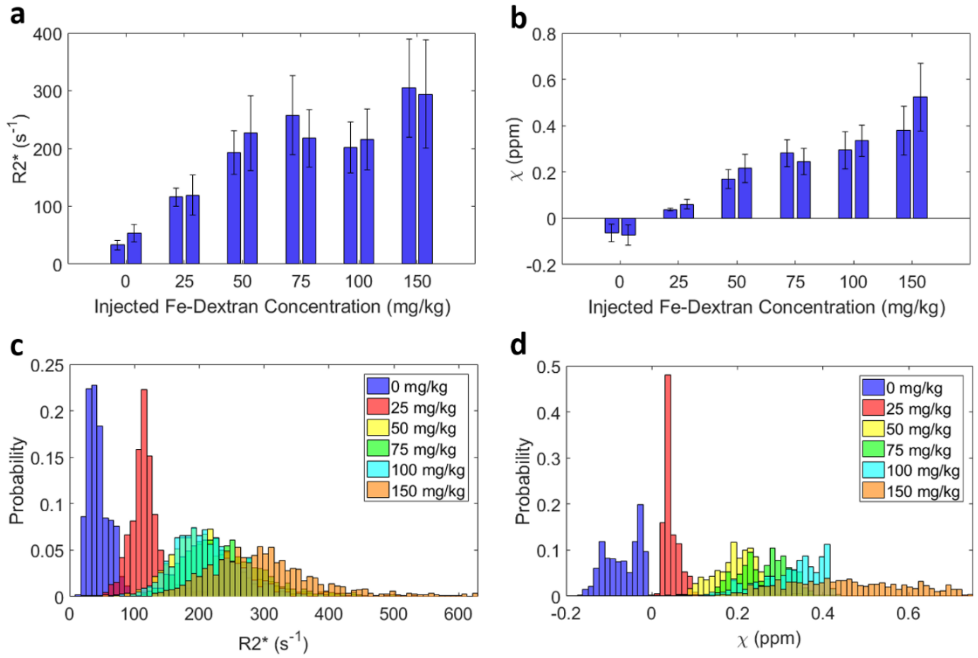

Figure 3.5: Quantitative R_2^* (a and c) and susceptibility (b and d) measurements obtained from MR acquired data. Average R_2^* and susceptibility measurements both increase relatively linearly with the experimentally injected Fe-dextran concentration, and the standard deviations also tend to increase as the injected concentration increases. The increases in the averages of R_2^* and susceptibility suggest that larger amounts of iron is accumulating in the liver with higher concentrations of injected Fe-dextran, which is confirmed by ICP-MS measurements (Figure 3.2b), and the larger standard deviations suggest that iron is accumulating non-homogeneously (which can be seen in a representative slice in Figure 3.7), which is confirmed by histology (Figure 3.3).

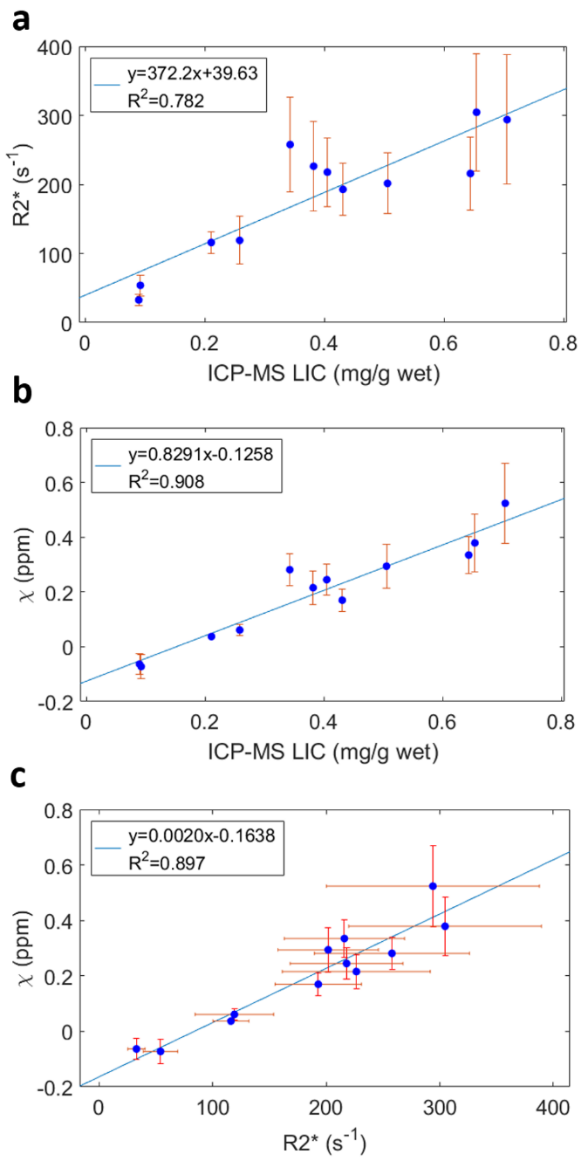

Figure 3.6: Linear regression plots for measured ICP-MS LIC and average measured R_2^* (a) and susceptibility (b) values. Both R_2^* and susceptibility measurements correlate well with ICP-MS LIC (R^2=0.78 and R^2=0.91, respectively), which demonstrates the feasibility of quantifying LIC using MR-based quantification methods. The susceptibility measurements, however, correlate more strongly and also have a smaller average standard deviation to slope ratio (0.073±0.045 mg/g wet) than the R_2^* measurements (0.128±0.0735 mg/g wet) indicating that smaller changes in LIC can be measured without significant overlap in the distributions of the measurements. This suggests that susceptibility may be a better measure for quantifying LIC than R_2^*. A good linear correlation is also observed between the average R_2^* and susceptibility measurements (c).

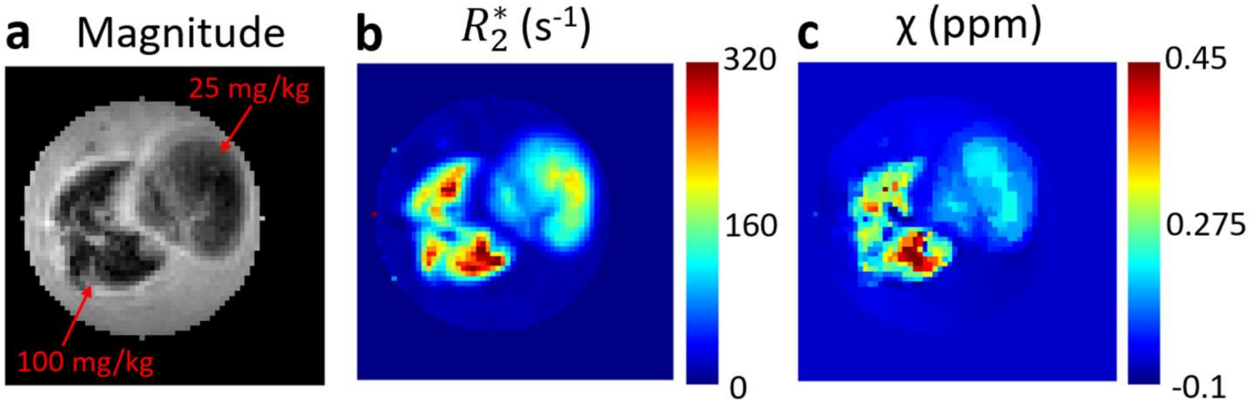

Figure 3.7: MRI magnitude image (a), R_2^* map (b), and quantitative susceptibility map (c) for a representative slice containing two excised livers from mice injected with different Fe-dextran concentrations (left: 100 mg/kg and right: 25 mg/kg). The liver from the mouse injected with a concentration of 100 mg/kg shows lower signal intensities and higher R_2^* and susceptibility values than the liver from the mouse injected with 25 mg/kg. The spatial distributions of R_2^* and susceptibility throughout each liver also appear to be non-homogeneous; suggesting that iron accumulation is non-homogeneous, which is confirmed by histology (Figure 3.3).

PART 2

STUDYING PIG BRAIN FUNCTIONAL CONNECTIVITY USING MAGNETIC RESONANCE IMAGING

Functional magnetic resonance imaging (fMRI) is a non-invasive medical imaging technique that allows for the spatial monitoring of neuronal activity and the mapping of the brain's functional connectivity. Along with diffusion tensor imaging (DTI), which allows for the mapping of the brain's structural connectivity by tracking the diffusion of water molecules, MRI can provide valuable information to help study brain connectivity.

To facilitate its study, an animal model often serves as a surrogate for a human subject. Rodent and non-human primate models have primarily been used for studying functional and structural brain connectivity in pre-clinical research. However, rodents have some significant differences in brain anatomy compared to the human brain, and the use of non-human primates is economically challenging. Due to the similar size, structure, composition, and neurodevelopment of the pig brain in comparison to the human brain, the pig serves as a useful large animal model for studying brain connectivity.

Part 2 of this dissertation examines the use of the pig as a translational model for brain research, with a specific focus on functional connectivity. Chapter 4 provides a brief overview of the physical mechanisms that govern fMRI and DTI. Chapter 5 seeks to detect and establish resting-state networks (RSNs) in the pig brain and draws comparisons with human RSNs, and

Chapter 6 explores the feasibility of detecting functional connectivity disruptions in the pig brain caused by traumatic brain injury using both resting-state and task-based fMRI.

CHAPTER 4

INTRODUCTION AND LITERATURE REVIEW

Functional Magnetic Resonance Imaging

Electroencephalography (EEG), which measures electrical impulses in the brain, and magnetoencephalography (MEG), which measures magnetic fields generated during brain activity, are two common techniques for studying brain functional connectivity. However, these techniques are limited by the spatial resolution they can achieve (~10-20mm) [1]. Positron emission tomography (PET) is another technique that uses the decay of radioactive isotopes to study functional connectivity, and PET can achieve spatial resolutions of approximately 5-10mm [1]. However, consumption of the radioactive isotope makes this technique semi-invasive and creates additional risks. Functional magnetic resonance imaging (fMRI) is a technique that allows for high spatial resolution (~0.5-4mm) [1, 2], while remaining entirely non-invasive. It uses changes in brain metabolism, specifically oxygenation, to detect and study brain functional connectivity.

The processes associated with neural signaling require the nucleotide adenosine triphosphate (ATP), which is primarily produced from glycolytic oxygenation of glucose [3]. When a region of the brain is active, there’s an increase in ATP demand in the local area of activation, and therefore, an increase demand for oxygen, which is delivered through the blood [4]. Immediately following neural firing, deoxygenated hemoglobin increases and oxygenated hemoglobin deceases as the oxygen in the area is utilized. Then a hemodynamic response occurs which causes the reverse of this (decrease in deoxygenated hemoglobin and increase in oxygenated hemoglobin) as oxygen levels are restored and then exceeded resulting in an over-abundance of oxygenated hemoglobin [1, 5, 6]. Deoxygenated hemoglobin is paramagnetic and causes magnetic field perturbations that decrease the MR signal. Therefore, the hemodynamic response causes an increase in the MR signal as most of the deoxygenated hemoglobin is replaced by oxygenated hemoglobin. Due to this process, we call the fMRI signal a blood oxygenation level dependent (BOLD) signal.

There are two main types of fMRI experiments: task-based (tb-) and resting-state (rs-). Both require the BOLD signal to be acquired temporally over several minutes with a temporal resolution usually around 1-3s. In tb-fMRI, an external stimulus is applied or a specific task is performed in order to activate a desired brain region(s). This stimulus or task is typically applied/performed in either a block design, meaning the stimulus has alternating periods of being on and off with each block typically lasting 10-30s, or an event-related design, meaning the stimulus is randomized non-periodically. Alternatively, rs-fMRI temporal measures the BOLD signal explicitly in the absence of any external stimulus or task. It seeks to detect the intrinsic neural activity or synchronized fluctuations in brain activity that are naturally and continually occurring due to processes related to high-level cognitive processes, such as self-awareness, emotion, and memory [7-10]. Resting state networks (RSNs) associated with visual, auditory, and sensorimotor functions have also been discovered [8, 9].

From the acquired spatial-temporal data, various methods have been proposed to decompose the data into spatial activation maps and their associated time series. Data driven approaches, such as independent component analysis (ICA), have become the most popular methodologies for determining functional connectivity. ICA attempts to extract independent signal components from a mixed signal through linear matrix decomposition [11]. More recently, machine learning techniques, such as sparse dictionary learning (sDL) and convolutional neural network (CNN) sparse autoencoders, have been explored to perform the decomposition [12, 13]. sDL is an iterative algorithm for learning a sparse representation of the input data as a linear combination of a dictionary of elements or signal components [14]. Unlike ICA, which assumes independent components, sDL does not assume independence between its elements. A CNN sparse autoencoder also does not assume independent components, and unlike ICA and sDL, which are linear decompositions, CNNs perform non-linear decomposition [15]. CNN sparse autoencoder algorithms are iterative and learn features of a dataset by applying a series of mathematical convolutions and data dimensionality reductions through a pooling process [13, 16]. Chapter 5 draws comparisons between some of these methods while attempting to characterize RSNs in the pig brain.

Diffusion Tensor Imaging

As discussed in the previous section, functional connectivity in the brain can be determined using fMRI to measure changes in the BOLD signal. Another feature of the brain that is important in many neurological studies is the brain’s structural connectivity, referring to the white matter nerve tracts that transmit electrical signals allowing different brain regions to communicate. The primary method for mapping the brain’s structural connectivity is an MRI-based method called diffusion tensor imaging (DTI) [17, 18].

DTI uses magnetic field gradients to track the Brownian motion of water molecules along structural pathways. White matter nerve tracts contain axons, which are long cylindrical structures that are covered by a cell membrane called the axolemma [19]. This bilipid membrane restricts the motion of water molecules causing them to generally diffuse along the cylindrical axis. By applying a series of magnetic field gradients and following the movement of these water molecules, a map of the white matter nerve tracts can be constructed.

In theory, following MR excitation of water molecules in the brain, all of the magnetic moments or spin-precessional moments of the hydrogen atoms within the molecules should be in-phase with each other. Then when a directional magnetic field gradient (referred to as a diffusion gradient) is applied, the magnetic moments in different locations along the gradient begin to precess at different frequencies, causing the signals at those locations to become out-of-phase with each other. After the first diffusion gradient is applied, a period of time (typically 10-100ms) is given to allow the water molecules to freely diffuse [20]. Then an identical diffusion gradient is applied, only this time in the opposite direction. Molecules that did not diffuse will re-phase with each other, while molecules that diffused along the gradient's axis will not re-phase due to the difference in their location during the second applied gradient in comparison to the first [17, 20]. A schematic of this process is given in Figure 4.1.

By performing this process once, information about the diffusion of water molecules along the direction of the applied diffusion gradient can be determined. However, in order to fully map out the three-dimensional structural white matter tracts in the brain, this process needs to be performed with a minimum of six non-collinear diffusion gradient directions, allowing for the creation of a three-by-three diffusion tensor matrix for each voxel in the MR image. The eigenvectors of the diffusion tensor matrix give information about the directionality of the diffusion, and the eigenvalues give information about the magnitude [17, 20, 21]. Although only six diffusion gradient directions are theoretically necessary to solve for the eigenvectors and eigenvalues, in practice as many as 30-60 uniformly distributed diffusion gradient directions are applied to improve estimation accuracy and reduce errors caused by factors such as noise. Many methods for estimating these vectors and values have been proposed, including: ordinary least squares [21, 22], weighted linear least squares [22, 23], and non-linear least squares [24].

Once the eigenvectors and eigenvalues have been determined for each voxel, tractography is performed, which is the methodology of connecting voxels to construct the nerve fiber tracts [18]. The primary eigenvector reflects the direction of maximal diffusion. Therefore, tractography methods usually involve fibers being constructed starting from voxels with fractional anisotropy (directional magnitude) greater than a specified threshold, propagating along the direction of the primary eigenvector across voxels, and ending once the fractional anisotropy reaches a voxel with a fractional anisotropy below a specified threshold (Figure 6.2) [18, 20]. Quantitative measures related to the nerve fibers, such as mean diffusivity, fractional anisotropy, fiber length, and fiber density, can then be determined, and these structural connectivity measures have been shown to correlate with functional connectivity [25, 26]. Chapter 5 uses these structural connectivity measures to support the validity of newly characterized functional RSNs in the pig brain.

References

1. Glover, G.H., *Overview of functional magnetic resonance imaging.* Neurosurgery Clinics, 2011. **22**(2): p. 133-139.
2. Shmuel, A., et al., *Spatio-temporal point-spread function of fMRI signal in human gray matter at 7 Tesla.* Neuroimage, 2007. **35**(2): p. 539-552.
3. Roland, P.E., P.E. Roland, and P.E. Roland, *Brain activation*. 1993: Wiley-Liss New York.
4. Buxton, R.B. and L.R. Frank, *A model for the coupling between cerebral blood flow and oxygen metabolism during neural stimulation.* Journal of cerebral blood flow & metabolism, 1997. **17**(1): p. 64-72.
5. Buxton, R.B., E.C. Wong, and L.R. Frank, *Dynamics of blood flow and oxygenation changes during brain activation: the balloon model.* Magnetic resonance in medicine, 1998. **39**(6): p. 855-864.
6. Davis, T.L., et al., *Calibrated functional MRI: mapping the dynamics of oxidative metabolism.* Proceedings of the National Academy of Sciences, 1998. **95**(4): p. 1834-1839.

7. Biswal, B., et al., *Functional connectivity in the motor cortex of resting human brain using echo-planar MRI.* Magnetic resonance in medicine, 1995. **34**(4): p. 537-541.
8. Shen, H.H., *Core concept: Resting-state connectivity.* Proceedings of the National Academy of Sciences, 2015. **112**(46): p. 14115-14116.
9. Damoiseaux, J.S., et al., *Consistent resting-state networks across healthy subjects.* Proceedings of the national academy of sciences, 2006. **103**(37): p. 13848-13853.
10. Uddin, L.Q., K. Supekar, and V. Menon, *Reconceptualizing functional brain connectivity in autism from a developmental perspective.* Frontiers in human neuroscience, 2013. **7**: p. 458.
11. Calhoun, V.D., et al., *A method for making group inferences from functional MRI data using independent component analysis.* Human brain mapping, 2001. **14**(3): p. 140-151.
12. Zhang, W., et al., *Experimental comparisons of sparse dictionary learning and independent component analysis for brain network inference from fMRI data.* IEEE Transactions on Biomedical Engineering, 2018. **66**(1): p. 289-299.
13. Huang, H., et al., *Modeling task fMRI data via deep convolutional autoencoder.* IEEE transactions on medical imaging, 2017. **37**(7): p. 1551-1561.
14. Mairal, J., et al., *Online learning for matrix factorization and sparse coding.* Journal of Machine Learning Research, 2010. **11**(Jan): p. 19-60.
15. Lopez, M. and W. Yu. *Nonlinear system modeling using convolutional neural networks*. in *2017 14th International Conference on Electrical Engineering, Computing Science and Automatic Control (CCE)*. 2017. IEEE.
16. Lawrence, S., et al., *Face recognition: A convolutional neural-network approach.* IEEE transactions on neural networks, 1997. **8**(1): p. 98-113.
17. Basser, P.J., J. Mattiello, and D. LeBihan, *MR diffusion tensor spectroscopy and imaging.* Biophysical journal, 1994. **66**(1): p. 259-267.
18. Basser, P.J., et al., *In vivo fiber tractography using DT-MRI data.* Magnetic resonance in medicine, 2000. **44**(4): p. 625-632.
19. Fitzpatrick, M., W. Maxwell, and D. Graham, *The role of the axolemma in the initiation of traumatically induced axonal injury*. 1998, BMJ Publishing Group Ltd.
20. Mori, S. and J. Zhang, *Principles of diffusion tensor imaging and its applications to basic neuroscience research.* Neuron, 2006. **51**(5): p. 527-539.
21. Soares, J., et al., *A hitchhiker's guide to diffusion tensor imaging.* Frontiers in neuroscience, 2013. **7**: p. 31.
22. Koay, C.G., et al., *Investigation of anomalous estimates of tensor-derived quantities in diffusion tensor imaging.* Magnetic Resonance in Medicine: An Official Journal of the International Society for Magnetic Resonance in Medicine, 2006. **55**(4): p. 930-936.
23. Anderson, A.W., *Theoretical analysis of the effects of noise on diffusion tensor imaging.* Magnetic Resonance in Medicine: An Official Journal of the International Society for Magnetic Resonance in Medicine, 2001. **46**(6): p. 1174-1188.
24. Papadakis, N.G., et al., *A measure of curve fitting error for noise filtering diffusion tensor MRI data.* Journal of Magnetic Resonance, 2003. **164**(1): p. 1-9.
25. Honey, C.J., et al., *Predicting human resting-state functional connectivity from structural connectivity.* Proceedings of the National Academy of Sciences, 2009. **106**(6): p. 2035-2040.

26. Damoiseaux, J.S. and M.D. Greicius, *Greater than the sum of its parts: a review of studies combining structural connectivity and resting-state functional connectivity*. Brain Structure and Function, 2009. **213**(6): p. 525-533.

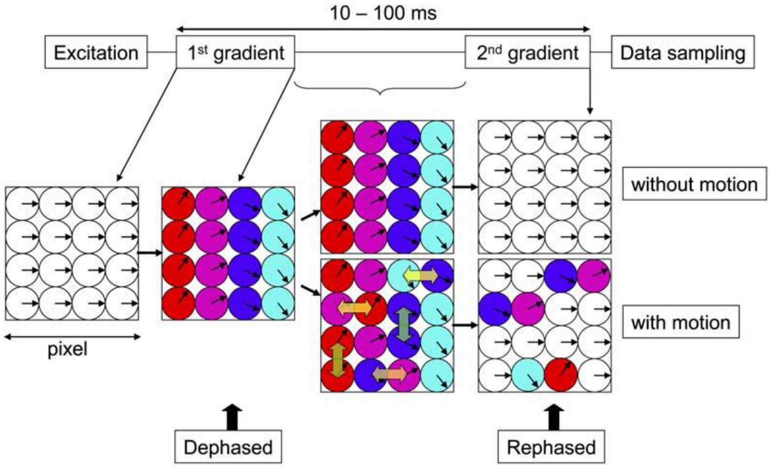

Figure 4.1: A schematic showing the principles of diffusion weighted imaging [20]. The magnetic moments (arrows) of the water molecules (circles) are initially in-phase after excitation. A magnetic field gradient, known as a diffusion gradient, is applied to intentionally dephase the molecules. A period of time is given to allow the molecules to freely diffuse. Finally, a second diffusion gradient is applied with equal magnitude, but opposite direction as the first gradient. The molecules that did not diffuse rephase, while the molecules that diffused along the axis of the applied gradients (horizontal) do not rephase. Note that the water molecules that diffuse along the vertical axis or perpendicular to the applied gradients do rephase as well. Figure reproduced with permission from publisher Elsevier Inc.

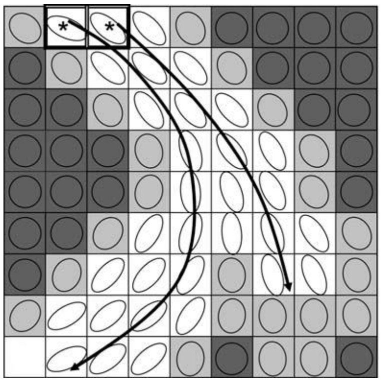

Figure 4.2: Two-dimensional example of nerve fiber tracting or tractography [20]. Fibers begin at pixels of high fractional anisotropy (pixels with asterisks), propagate along the direction of the primary eigenvectors (indicated by the major axis of each ellipse), and end once reaching a pixel of low anisotropy (darker, less oblong pixels). Figure reproduced with permission from publisher Elsevier Inc.

CHAPTER 5

PIG BRAINS HAVE HOMOLOGOUS RESTING STATE NETWORKS WITH HUMAN BRAINS [1]

---

[1] Simchick, G., Shen, A., Campbell, B., Park, H. J., West, F. D., and Zhao, Q. 2019. *Brain Connectivity,* (ja).

Reprinted here with permission of publisher Mary Ann Liebert Inc., New Rochelle, NY.

Abstract

Many neurological and psychiatric diseases in humans are caused by disruptions to large-scale functional properties of the brain, including functional connectivity. There has been growing interest in discovering the functional organization of brain networks in larger animal models. As a result, the use of translational pig models in neuroscience has significantly increased in the past decades. The gyrencephalic pig brain resembles the human brain more in anatomy, growth, and development than the brains of commonly-used small laboratory animals such as rodents**.** In this work, resting state functional MRI (rs-fMRI) and diffusion tensor imaging (DTI) data were acquired from a group of pigs (n=12). rs-fMRI data was analyzed for resting state networks (RSNs) using independent component analysis (ICA) and sparse dictionary learning (sDL). Six RSNs (executive control, cerebellar, sensorimotor, visual, auditory, and default mode) were detected that resemble their counterparts in human brains, as measured by Pearson spatial correlations and mean ratios. Supporting evidence of the validity of these RSNs was provided through the evaluation and quantification of structural connectivity measures (mean diffusivity, fractional anisotropy, fiber length, and fiber density) estimated from the DTI data. This study shows that as a translational, large animal model, pigs demonstrate great potential for mapping connectome-scale functional connectivity in experimental modeling of human brain disorders.

Introduction

Resting-state fMRI (rs-fMRI) is used to examine functional connectivity in the brain through the recording and analysis of blood-oxygenation-level dependent (BOLD) oscillations originating from synchronized intrinsic neuronal activity in the absence of any explicit task [1-3]. In rs-fMRI analysis, functional connectivity is quantified using various temporal and/or spatial metrics, such as correlation, covariance, and mutual information between the BOLD time series signals collected from different brain regions. This quantification of functional connectivity can highlight sets of distinct cortical and subcortical areas that form integrated information processing networks and can be used to construct connectivity maps.

Numerous prior rs-fMRI studies have reported a number of functional connectivity networks, commonly referred to as resting-state networks (RSNs) or intrinsic connectivity networks (ICNs) [4], in the human brain. Atlases of the most common human brain RSNs or ICNs have been developed [5, 6] and have been used to quantify fMRI activation patterns in healthy subjects. In addition to functional connectivity, structural connectivity has also been studied using diffusion tensor imaging (DTI) to measure the diffusion of water molecules in the brain. Many studies have reported associations between functional and structural connectivity [7], for example in the default mode network [8] and in the aging population [9]. Some studies have shown that the strength of resting-state functional connectivity is positively correlated with that of structural connectivity [10]. However, other studies have also reported functional connectivity detected between regions with little or no structural connectivity [11], suggesting that functional connectivity may also be mediated by indirect structural connections.

Inspired by the discovery of RSNs in the human brain from rs-fMRI analysis, there has been a growing interest in finding similar networks of functional connectivity in animal models. The ability to map homologous connectome-scale functional connectivity in a highly translational animal model will improve characterization of the effects of neural diseases and brain injuries on major neural functions and allow such findings to have meaningful translational implications in humans. Rodents and non-human primates have been the most commonly used animal models [12, 13]. However, these animal models are non-ideal due to a number of limitations: the rodent brain is lissencephalic (lacks gyri and sulci) and has significantly different brain anatomy relative to the human brain, and economic considerations hinder the use of non-human primates in brain research. Because of this, there is a growing need for the establishment of alternative non-primate, large animal models.

Use of the pig brain as a model has been rapidly increasing in neuroscience research due to its similarities in size, structure, composition, and development to that of the human brain. The percentage of brain weight at birth, brain growth spurts, and prenatal and postnatal brain maturation patterns in humans are also more similar to pigs relative to other animal models [14]. The pig brain is larger in volume and weight (~180 g) than that of a rodent (~10 g) and is comparable in size to that of a non-human primate (~300 g), while being much less expensive [15]. The pig brain, like the human brain, is also gyrencephalic and follows a similar gyral pattern [16]. The volume of the prefrontal cortex in the pig constitutes 10% of total brain volume, which is comparable to humans whose prefrontal cortex constitutes approximately 12.5% of total brain volume [17, 18]. The dorsal striatum of the pig brain is split by the internal capsule into two distinct structures: the caudate nucleus and the putamen; while in comparison, the rodent brain only contains a single caudate-putamen structure [19, 20]. The pig hippocampus has been well described and found to be structurally more similar to the human hippocampus than the rodent, having a degree of encephalization that lies between rodent and primate [21]. A number of descriptive, comparative anatomical studies have been performed for the pig brain thalamus, hypothalamus, hypothalamic nuclei [22-24], brainstem structures [25, 26], and cerebellum [27]. Similar to humans, sensory cortices such as the motor cortex [28] and the somatosensory cortex [29] are arranged somatotopically.

In establishing a translational animal model for brain injury and neurological disease research, it is important that the brain of the animal have similar anatomy and organization to the human brain, as it impacts the brain regions injured, vascular responses, short- and long-term effects of the injury, and ultimately whether the findings are translational to humans [30]. Pig models of stroke and traumatic brain injury (TBI) have recently been developed and show comparable anatomical damage and physiological responses as would be expected in human patients [31, 32]. However, groundwork studies to characterize functional connectivity in the pig animal model have yet to be conducted.

To model rs-fMRI data and determine brain functional connectivity, a variety of data-driven approaches have been proposed over the past decades. Independent component analysis (ICA) is one method that has been very successful [33]. Alternatively, sparse dictionary learning (sDL) [34] is another data-driven approach that has been successfully applied to reconstruct brain functional connectivity . In sDL-based methods, fMRI data is decomposed into two matrices: a dictionary basis matrix (which represents the time-domain activity of functional networks) and a reference weight matrix (which represents the spatial distributions of the functional networks within the brain). Generally, the sDL approach provides a compact, high-fidelity representation of the fMRI data and discovers spatial patterns representing functional connectivity [35, 36].

In this manuscript, rs-fMRI and DTI data were acquired from a group of three-week-old piglets. From the rs-fMRI data, both ICA and sDL were employed to empirically detect RSNs in the pig brain. In order to quantify the degree of homology between the detected pig RSNs and human RSNs, a reference pig RSN atlas was created by combining anatomies from a standard pig brain atlas [37] that are known to be associated with human RSNs. Using the reference atlas and empirically detected pig RSNs, Pearson spatial correlation coefficients and mean ratio metrics were calculated and used to determine the degree of homology between the detected pig RSNs and human RSNs. From acquired DTI data, structural connectivity measures (mean diffusivity, fractional anisotropy, fiber length, and fiber density) were quantified for each detected pig RSN in order to provide supporting evidence of their validity. To the best knowledge of the authors, this is the first study to attempt to characterize RSNs in the pig brain to date.

Materials and Methods

Subjects

Three-week-old Landrace-cross pigs (n=12) were used in this study. Pigs were initially sedated through an intramuscular injection of xylazine (7 mg/kg), butorphanol (0.3 mg/kg), and midazolam (0.3 mg/kg). Then mild anesthesia was maintained with 1.5% inhalational isoflurane in oxygen in order to keep the pigs sedated while reducing anesthetic agents from interfering with pig brain neural activity and neurovascular coupling. All experimental procedures were approved by the Institutional Animal Use and Care Committee (IAUCC, University of Georgia).

Data acquisition

Using a GE Signa HDx 3T scanner and a HD quadrature knee coil, rs-fMRI, T1-weighted anatomical, and DTI data was acquired using the following three sequences: 1.) rs-fMRI: gradient echo EPI sequence (TR=3s, TE=30ms, FA=80°, FOV=12.8x12.8x6.4cm, a matrix size of 96x96x32, 300 total volumes, and an acquisition time of 15 mins), 2.) T1-weighted anatomical: 3D fast spoiled gradient echo (FSPGR) sequence (TR=5.5s, TE=2.1ms, FA=9°, FOV=12.8x12.8x6.4cm, slice thickness=1mm, and a matrix size of 256x256x112), and 3.) DTI: spin echo EPI sequence (TR=15.5s, TE=min-full, FOV=12.8x12.8x6.4cm, a matrix size of 64×64x32, 3 b=0 images, and 30 diffusion weighted images using b=1000s/mm^2).

Data preprocessing

Pig rs-fMRI data was preprocessed to realign images to correct for motion, perform slice-timing correction, and execute spatial normalization using the Realign and Unwarp, Slice timing, and Old Normalize Statistical Parametric Mapping (SPM) software algorithms, respectively [38, 39]. One pig was chosen as the template, and the rs-fMRI datasets of the other eleven pigs were spatially normalized to the template pig fMRI space. The first volume from each rs-fMRI dataset was used to calculate a spatial transformation, and the transformation was then applied to the rest of the volumes. All spatial transformations in this work were performed by first applying a 12-parameter affine transformation, followed by a nonlinear deformation transformation [40, 41].

Next, brain tissue was separated from the skull and other surrounding tissues by manual slice-by-slice segmentation of the images, and the rs-fMRI time series from the twelve pigs were temporally concatenated into a group dataset. Due to severe movement that occurred for one of the pigs towards the end of its rs-fMRI data acquisition, eight volumes could not be corrected for motion and were removed; therefore, the total time series length of the group dataset was 3592 (total number of volumes).

Data analysis

The group dataset was analyzed using FastICA and sparse Dictionary Learning, respectively. ICA attempts to extract independent signal components from a mixed signal through matrix decomposition. In fMRI studies, spatial ICA is typically used, which extracts independent spatial components representing proposed functional networks. In this study, spatial ICA was performed using the Group ICA of fMRI Toolbox’s (GIFT) [33] FastICA algorithm, which is a commonly-used iterative algorithm for doing approximate ICA efficiently on large datasets. FastICA first performs a whitening process on the input data matrix before iteratively calculating a series of components through maximization of non-Gaussianity of the projection of the whitened input data matrix along the component.

An automated process to estimate the number of independent components for ICA decomposition from the group dataset was performed using the GIFT Toolbox, and it was estimated that the data was composed of 9 independent components. In order to reduce error in this estimation, ICA decomposition was performed using 20 independent components, which doubles the estimated component number and is also commonly used throughout the literature [5].

Sparse Dictionary Learning (sDL) is an iterative algorithm for learning a sparse representation of the input data as a linear combination of a typically complete or over-complete dictionary of elements, or “atoms” [34]. In fMRI analysis, the entire signal volume of v voxels over t timepoints is arranged as a 2D signal matrix $\boldsymbol{X} \in \boldsymbol{R}^{t\times v}$, where the time course data of each of the v voxels is represented as a column with t rows.

Given a desired n number of atoms, sDL iteratively decomposes matrix $\boldsymbol{X}$ into a dictionary matrix $\boldsymbol{D} \in \boldsymbol{R}^{t\times n}$ and a sparse coefficient matrix $\boldsymbol{\alpha} \in \boldsymbol{R}^{n\times v}$, such that $\boldsymbol{D} \times \boldsymbol{\alpha}$ closely approximates the signal matrix $\boldsymbol{X}$ through the minimization of the mean squared error between $\boldsymbol{X}$ and $\boldsymbol{D} \times \boldsymbol{\alpha}$, while fulfilling a L$_1$-regularization sparsity constraint of λ on $\boldsymbol{\alpha}$, as summarized in Eq. (5.1). Again, n is typically selected so that the dictionary matrix $\boldsymbol{D}$ is complete or over-complete ($n \geq t$), allowing the $\boldsymbol{\alpha}$ matrix to be sparse.

$$\min_{\boldsymbol{D}\in C} \lim_{n\to+\infty} \frac{1}{n}\sum_{i=1}^{n}\left(\min_{\alpha^i} \frac{1}{2}\left\|\boldsymbol{x}^i - D\boldsymbol{\alpha}^i\right\|_2^{\;2} + \lambda\left\|\boldsymbol{\alpha}^i\right\|_1\right) \qquad (5.1)$$

Through this decomposition, the original signal time series of each voxel is represented as a linear combination of n dictionary atoms of length t, where each atom corresponds to the time series of a potential functional network detected by the decomposition. The corresponding row in $\boldsymbol{\alpha}$ represents the strength of involvement of each of v voxels in the detected functional network, which can be mapped back to a brain volume in order to generate a map of each of the n potential functional networks, as illustrated in Figure 5.1.

In this study, the SPArse Modeling Software (SPAMS) toolbox [34] was used to implement the Online Dictionary Learning (ODL) algorithm. ODL trains a dictionary by iteratively using each sample of an input data matrix to calculate a sparse coding using least angle regression, and then using the calculated sparse coding to update the dictionary [34]. As an iterative algorithm, ODL is suitable for performing sDL on large datasets that are too large to fit into memory [36]. When performing sDL, a complete dictionary (n=292) and a sparsity parameter of λ=0.15 were used. For details regarding the optimization of n and λ, see Appendix B.

Pig Reference RSN analysis

In order to quantify the degree of homology between the detected pig RSNs and established human RSNs, a reference pig RSN atlas was created by first spatially normalizing a standard pig brain atlas [37] to the anatomical space of the template pig. Spatial normalization was accomplished by calculating a spatial transformation using anatomical data provided in the same space as, and associated with, the standard pig brain atlas and the anatomical data of the template pig. The calculated transformation was then applied to the atlas. The anatomically homologous pig brain regions associated with six major human RSNs [5, 6] were manually selected and combined to construct the following six pig RSNs: executive control (EX), cerebellar (CERE), visual (VIS), sensorimotor (SM), auditory (AUD), and default mode (DMN). These six manually constructed pig RSNs formed a reference atlas that was assumed to be perfectly homologous to the six human RSNs and subsequently used as a reference to calculate the degree of homology of the empirically detected RSNs found by ICA and sDL. Table 5.1 lists the anatomies and corresponding atlas labels from the standard pig brain atlas [37] that were used to construct each of the six reference pig RSNs.

To determine which brain connectivity decomposition method best identified the six reference RSNs, the functional activation maps generated by each method were thresholded using a Z-score of one, normalized between zero and one, and then spatially normalized to the anatomical space of the template pig. Spatial normalization was accomplished by calculating a spatial transformation using the template pigs' fMRI data and anatomical data; then applying the calculated transformation to the activation maps.

The activation maps that produced the maximum Pearson spatial correlation coefficients for each of the six reference RSNs were then determined for each method, and mean ratio values were calculated for the selected activation maps. The Pearson spatial correlation coefficient was defined as

$$r = \frac{\sum_{i=1}^{n}(A_i-\bar{A})(R_i-\bar{R})}{\sqrt{\sum_{i=1}^{n}(A_i-\bar{A})^2}\sqrt{\sum_{i=1}^{n}(R_i-\bar{R})^2}} \qquad (5.2)$$

where *n* is the number of voxels within the brain, *A* is the activation value or sparse coefficient, *R* is the atlas value (which is binary), and an overbar denotes the arithmetic mean. The mean ratio was defined as

$$m = \frac{(\sum_{i=1}^{n} A_i * R_i) \big/ (\sum_{i=1}^{n} R_i)}{\bar{A}} \qquad (5.3)$$

or simply stated, the mean activation value within a given RSN atlas divided by the mean activation value of the entire brain. Rose maps of the Pearson and mean ratio values were used to evaluate the effectiveness of each method at generating activation maps that correlate well with the reference pig RSN atlas.

DTI analysis

Group tractography was performed using an early registration and superset method [42], which included two spatial transformations. First, the DTI dataset of each pig was spatially normalized to the DTI space of the template pig. The spatial transformation was calculated using the DTI volumes of each pig that were acquired when no diffusion gradient (b=0) was applied, and the transformation was then applied to all DTI volumes. Next, the volumes from all of the spatially normalized datasets were combined into a group superset giving a total of 396 (33 diffusion gradient directions per pig x 12 pigs) DTI volumes, and brain tissue was separated from surrounding tissue by manual segmentation. The DTI superset was then spatially normalized to the anatomical space. The second spatial transformation was calculated using the DTI volume of the template pig acquired with no diffusion gradient applied (b=0) and the anatomical data, and the transformation was then applied to all volumes within the superset. During this second transformation, voxel size was forced to be 0.75mm cubed, opposed to the 0.5mm cubed voxels of anatomical space, in order to reduce the computational size of the dataset. The DTI gradient vectors were corrected accordingly based on each spatial transformation applied to the DTI data.

Tractography was performed on the spatially normalized DTI superset using Medinria [43]. The Tensor ToolKit's (TTK) tensor estimation algorithm was used to determine the DTI tensors, and from the estimated tensors, mean diffusivity (*MD*) and fractional anisotropy (*FA*) maps were created. Tractography was also performed using the TTK's tensor tractography algorithm. Whole brain tractography was performed with fibers seeding from voxels with *FA* greater than approximately double the whole brain average, fibers stopping at voxels with *FA* less than approximately two-thirds of the whole brain average, and the fibers were not restricted to any minimum fiber length (*FL*). In addition, tractography of just the major fibers was performed with fibers seeding from voxels with *FA* greater than approximately double the whole brain average, fibers stopping at voxels with *FA* less than approximately four-thirds of the whole brain average, and a minimum *FL* of 10mm.

Before making quantitative measurements, the activation maps determined by the pig RSN analysis described above were corrected by removing any regions of the activation volume that were not overlapping with gray matter structures. Using the whole brain tractography result, measurements of *MD*, *FA*, and *FL* were then obtained for the fibers intersecting with the remaining activation volume. The fiber density (*FD*), defined as the number of fibers intersecting with an activation volume divided by the activation volume, was also determined. All measurements of *MD*, *FA*, *FL*, and *FD* were normalized by their respective whole brain averages, calculated from all brain structures for comparison.

Results

Using the above describe Pearson correlation analysis, the maximum Pearson values obtained from the 20 activation maps generated using ICA and 292 maps generated using sDL for each reference RSN are given in Figure 5.2a, and Figure 5.2b gives the associated mean ratio values for these maps. The activation maps produced by sDL show stronger Pearson correlations with the atlas than the maps produced by ICA (values in the range of 0.30-0.53 and 0.16-0.47, respectively), as well as greater mean ratio values (range of 2.00-3.98 and 2.12-2.71, respectively). It was observed that sDL tends to produce multiple maps with similar activation patterns and similarly high Pearson values for each RSN from the atlas. When using a complete or over-complete dictionary to achieve sparseness, redundant representations of the same signal are possible. Therefore, averaged sDL activation maps were created by averaging the top three maps with the highest Pearson values for each reference RSN. These averaged maps produce even stronger Pearson correlations with the reference atlas (range of 0.32-0.53) and even higher mean ratio values (range of 2.72-7.64) in comparison to values obtained by ICA and non-averaged sDL (Figure 5.2).

Cross-sectional images of the activation maps associated with the maximum Pearson values generated by ICA for each reference RSN are displayed in Figure 5.3a, as well as cross sectional images of the reference RSN itself. All cross-sectional images are overlaid on the corresponding anatomical images. Rose maps giving the associated Pearson values (Figure 5.3b) and mean ratio values (Figure 5.3c) for the displayed activation maps are also presented. The activation map generated by ICA that gives the maximum Pearson value for the executive control RSN shows a strong correlation with this RSN exclusively, as evidenced by its low correlations with the other five RSNs within the reference atlas (Figure 5.3b-c, first column). However, this exclusivity is not consistent for all RSNs. For the cerebellar, visual, and default mode RSNs, the maximally correlated activation maps simultaneously exhibit comparatively strong correlations with their respective RSNs and other RSNs as well (Figure 5.3b-c, second, third, and sixth column), and for the sensorimotor and auditory RSNs, the maximally correlated activation maps show stronger correlations with other RSNs within the atlas than with their respective RSN (Figure 5.3b-c, fourth and fifth column).

The maximally correlated activation maps generated by sDL for the executive control, cerebellar, and visual RSNs all show strong and exclusive correlations with their respective RSNs (Figure 5.4b-c, first-third columns). However, for the sensorimotor, auditory, and default mode RSNs, sDL produced maximally correlated activation maps with comparatively strong correlations with other RSNs as with their respective RSNs (Figure 5.4b-c, fourth-sixth columns). In comparison to ICA, sDL tends to produce maps that correlate better with an exclusive RSN.

For the averaged sDL activation maps, strong and exclusive correlations between each maximally correlated activation map and its respective reference RSN are observed (Figure 5.5b-c), except for the mean ratio of the default mode RSN. In comparison to the maps generated by ICA and sDL, the averaged sDL maps tend to correlate more strongly with an exclusive RSN. Three-dimensional projections of each of the averaged sDL activation maps, as well as each of the reference atlases, can be found in Figure B4-5 of Appendix B.

Correlations between the averaged sDL activation maps and the individual anatomical components of each reference RSN given in Table 5.1 were further explored using spatial Pearson correlations, mean ratios, and the volumetric percentage of each anatomical component in relation to its corresponding RSN volume, as determined from the reference pig RSN atlas (Table B1). Good correlations and high mean ratios were observed for the majority of individual anatomical components in each RSN. However, poor correlations were observed between the executive control network and the ventral anterior cingulate cortex and between the DMN and the anterior prefrontal, orbitofrontal, and parahippocampal cortices.

The averaged sDL activation maps were also further evaluated by examining the normalized *MD*, *FA*, *FL*, and *FD* measurements determined for the fibers intersecting with each activation volume (Figure 5.6). The overwhelming majority of the *MD* and *FA* values for the fibers intersecting with each activation volume are greater than the average value of the whole brain (Figure 5.6a-b), while the average *FL* of these fibers only tends to be slightly greater than the average fiber length in the whole brain (Figure 5.6c). The executive control, cerebellar, sensorimotor, and default mode RSNs all have *FD* values of approximately four times greater than the average *FD* of the whole brain, while the visual and auditory RSNs only have *FD* values of approximately two times greater than the average *FD* of the whole brain (Figure 5.6d).

To better demonstrate how structural fibers interact with each individual RSN, tractography of the whole brain, major fibers, and the fibers intersecting with the activation volume for each RSN determined from the averaged sDL activation maps are shown in Figure 5.7. The activation maps were corrected by removing any regions of the activation volume that were not overlapping with gray matter structures.

Discussion

Using ICA and sDL, the described empirical analysis generated six activation maps that have high degrees of correlation with the six reference pig RSNs (executive control, cerebellar, sensorimotor, visual, auditory, and default mode), which were derived from well-established human RSNs, indicating a high degree of homology. This finding suggests that there are RSNs in the translational pig brain model that may be homologous to RSNs found in the human brain. To the best of the authors' knowledge, this is the first study to identify RSNs in the pig brain and draw comparisons between those RSNs experimentally found in pigs and those previously established in humans.

In this work, the use of ICA and sDL to detect RSNs produces activation maps with Pearson values that fall within the typical range reported in the literature [44-46], and by averaging the top three sDL maps with the highest Pearson values, an averaged map can be generated that produces even stronger Pearson correlations in the range of 0.32-0.53 (Figure 5.2). These maps demonstrate six well-defined RSNs within the pig brain (Figure 5.5).

The detection of these RSNs using two separate methods, as well as evidence provided from structural connectivity analysis, further supports the validity of these RSNs, as functional and structural connectivity have been shown to be positively correlated [7, 8]. The *MD* and *FA* values of the fibers intersecting with each RSN show much greater diffusion and directionality of the diffusion along structural pathways through and within the RSNs in comparison to the average diffusion and directionality of the diffusion throughout the whole brain (Figure 5.6a-b). The fibers intersecting with each RSN also show greater average *FL* than the average *FL* found throughout the whole brain (Figure 5.6c), and each RSN's *FD* is greater than the *FD* found throughout the whole brain (Figure 5.6d).

The discovery of the six RSNs defined in this work may help to establish an experimental RSN atlas of a healthy pig brain, which will allow for future investigation of effects of neural diseases and disorders on major neural connections and functions within the pig brain model. There are a number of important pig neural injury, disease, and developmental models that cause functional changes closely associated with the six RSNs identified in this study. One such example is TBI. Multiple types of TBI in both pigs and humans have previously been shown to cause changes in activity in the sensorimotor network, as well as the executive control network and default mode network, resulting in a variety of symptoms, including deficits in motor coordination, proprioception, problem-solving, cognitive flexibility, and regular modulation of day and night activity patterns [47-51]. Stroke, the number one cause of long-term disability in the world, is another example of a major neurological injury successfully modeled in pigs and may cause changes in RSN activity [31, 32, 47, 52, 53]. In the pig model, studies found that ischemic stroke causes lesioning of the temporal and piriform lobes in regions housing the insular and auditory cortices, which are associated with the executive control and auditory networks, respectively [32]. Middle cerebral artery occlusion (MCAO) stroke in pigs can lead to atrophy in the hippocampus, parahippocampal cortex, and inferior temporal gyrus regions, all of which are associated with the default mode network [32]. The high amount (>60%) of white matter in the pig brain currently also makes it a suitable model for studying lucunar infarctions, small areas of necrosis in deep cerebral white matter occurring in 25% of ischemic stroke patients that can affect the activation of the primary motor cortex and sensorimotor network [54, 55].

By identifying pig RSNs homologous to the human sensorimotor, auditory, executive control, and default mode networks, which are associated with TBI and multiple types of ischemic stroke, the findings presented here further support the extended use of pigs as a translational model for characterizing the effects of TBI and stroke on functional network disruption and brain injury. Many previous pig studies of TBI, stroke, and nutrition [56-58] have heavily relied on observed tissue or whole animal function (e.g. behavior and cognitive tests, such as open field) changes, yet most were not capable of studying changes in brain functional networks due in part to the absence of developed pig functional network maps. This further highlights the importance of the pig RSNs reported in this study.

Despite the good correlations between the averaged sDL activation maps and most of the individual anatomical components of each RSN given in Table B1, some poor correlations for specific RSN anatomies were observed, including: the ventral anterior cingulate cortex of the executive control network and the anterior prefrontal, orbitofrontal, and parahippocampal cortices of the DMN. These poor correlations are possibly due to one or more of three reasons: 1) the anatomical region is not associated with the RSN, 2) anesthetic agents suppressed neural activity in the anatomical region, and/or 3) only a sub-region or fractional volume of the anatomical region is involved in the RSN.

Although, the minimal, feasible amounts of anesthetic agents were used in order to minimize interference with brain activity, the use of anesthesia is known to have potentially confounding effects on functional connectivity, as many anesthetic agents are known to interfere with neural activity and neurovascular coupling [59, 60]. It is possible the RSNs reported in this study may have been affected by the anesthesia protocol, and specific anatomical regions may have been affected more than others. This study is also potentially limited by the creation of the reference RSN atlas from a preexisting standard pig brain atlas and the assumption that the reference atlas is perfectly homologous with the human brain. In humans, certain anatomies, such as the anterior prefrontal cortex, are known to consist of sub-regions that may be functionally activated separately from the rest of the region. For example, only the medial area of the prefrontal cortex is involved in the human DMN [61], and this is also observed in the pig brain (Figure 5.5a, sixth column). However, the anterior prefrontal cortex listed in the standard pig brain atlas [37] was not segmented into smaller regions, and the medial area of the pig brain was unable to be differentiated from the rest of the region.

Among the four anatomical regions that were identified as having poor correlations with their corresponding functional activation maps, the orbitofrontal cortex is likely not associated with the DMN RSN. Since this anatomical region was also included in the reference atlas for the executive control network and shows good correlation with the functional activation map for this network, significant interference from anesthesia is unlikely, and the volume of this region is relatively small making fractional volume effects also unlikely.

Although anesthesia can have potentially confounding effects on functional connectivity, it should not interfere with structural connectivity. Therefore, to better determine which of the three reasons may have caused the poor correlations observed in the other three anatomical regions yet discussed (the ventral anterior cingulate, anterior prefrontal, and parahippocampal cortices), structural connectivity measures were evaluated for these regions (Figures B2-3). For the ventral anterior cingulate cortex of the executive control network, high structural connectivity measures were observed in comparison to the whole brain values (Figure B2). Since structural connectivity and functional connectivity have been shown to be positively correlated [7, 8], it is hypothesized that interference from anesthesia may have possibly affected this region. Since the volume of this region is relatively small, fractional volume effects are considered less likely.

For the anterior prefrontal and parahippocampal cortices of the DMN, high structural connectivity measures were also observed in comparison to the whole brain values (Figure B2). However, when comparing the measures of structural connectivity for the anatomical region defined by the reference atlas to the measures obtained for just the functionally activated sub-region from the averaged sDL activation maps of each anatomical region, increased fiber length and fiber density were observed within the sub-regions that were empirically determined to be activated (Figure B3). This observation, as well as the fact that these two anatomical regions are relatively large, leads to the hypothesis that these two regions only have fractional volumes that are involved in the DMN RSN.

As a whole, the DMN shows lower correlation values compared to the other five RSNs (Figure 5.2). This is possibly due to these fractional volume activations and may also be due in part to the young age of the pigs used in this study. Studies have shown that in the human infant brain, there is limited evidence of DMN activation, whereas functional connectivity is more consistent in children aged 9–12 years and older, suggesting that the DMN undergoes developmental change [62]. A possible explanation for the lower correlation values observed for the DMN in this work is that the pigs used are still young (3-weeks-old), and the DMN may not be fully developed at such a young age.

One other limitation of this study that the authors intend to improve upon in future work is the relatively small sample size (n=12). For larger sample sizes, better-defined RSNs may be obtained possibly leading to stronger correlations with the reference pig RSN atlas and/or better determination of non-involved anatomies contained within the atlas and fractional volumes may be feasible.

The results presented in this study provide a groundwork for the development of a standard pig brain functional network and RSN atlas, which can be used to support future translational pig model studies characterizing functional network disruption caused by disease and injury. Over the years, many studies have reported associations between functional and structural connectivity [7, 63], and some studies have shown that the strength of resting-state functional connectivity is positively correlated with that of structural connectivity [10]. However, other studies have detected functional connectivity between regions with little or no structural connectivity [11], suggesting that functional connectivity is likely mediated by indirect structural connections. In future work, the authors intend to continue exploring the relationship between functional and structural networks in the pig brain at multiple time points during brain development using advanced deep learning methods such as convolutional neural networks and deep generative models [64], and explore how these networks are effected by acute ischemic stroke and potential treatments of stroke.

Conclusion

The use of the pig model in neuroscience has significantly increased in the past two decades. The pig brain, which is gyrencephalic, resembles the human brain more in anatomy, growth, and development than the brains of commonly used small laboratory animals such as rodents**.** Using independent component analysis (ICA) and sparse dictionary learning (sDL), six RSNs (executive control, cerebellar, sensorimotor, visual, auditory, and default mode) were detected in the pig brain that resemble their counterparts in humans, as measured by Pearson spatial correlations and mean ratios, and supporting evidence of the validity of these RSNs was provided through the evaluation of structural connectivity. This study shows that as a translational, large animal model, pigs demonstrate great potential for mapping connectome-scale functional connectivity in experimental modeling of human brain disorders.

References

1. Biswal, B., et al., *Functional connectivity in the motor cortex of resting human brain using echo-planar mri.* Magnetic Resonance in Medicine, 1995. **34**(4): p. 537-541.
2. Fox, M.D., et al., *The human brain is intrinsically organized into dynamic, anticorrelated functional networks.* Proceedings of the National Academy of Sciences of the United States of America, 2005. **102**(27): p. 9673-9678.
3. Chang, C., et al., *Mapping and interpreting the dynamic connectivity of the brain.* NeuroImage, 2018. **180**: p. 335-336.
4. Hutchison, R.M., et al., *Dynamic functional connectivity: Promise, issues, and interpretations.* NeuroImage, 2013. **80**: p. 360-378.
5. Smith, S.M., et al., *Correspondence of the brain's functional architecture during activation and rest.* Proceedings of the National Academy of Sciences, 2009. **106**(31): p. 13040-13045.
6. Laird, A.R., et al., *Behavioral Interpretations of Intrinsic Connectivity Networks.* Journal of Cognitive Neuroscience, 2011. **23**(12): p. 4022-4037.
7. Honey, C.J., et al., *Predicting human resting-state functional connectivity from structural connectivity.* Proceedings of the National Academy of Sciences, 2009. **106**(6): p. 2035-2040.
8. Greicius, M.D., et al., *Resting-State Functional Connectivity Reflects Structural Connectivity in the Default Mode Network.* Cerebral Cortex, 2008. **19**(1): p. 72-78.
9. Damoiseaux, J.S., *Effects of aging on functional and structural brain connectivity.* NeuroImage, 2017. **160**: p. 32-40.
10. Damoiseaux, J.S. and M.D. Greicius, *Greater than the sum of its parts: a review of studies combining structural connectivity and resting-state functional connectivity.* Brain Structure and Function, 2009. **213**(6): p. 525-533.
11. Zimmermann, J., et al., *Structural architecture supports functional organization in the human aging brain at a regionwise and network level.* Human Brain Mapping, 2016. **37**(7): p. 2645-2661.

12. Lu, H., et al., *Synchronized delta oscillations correlate with the resting-state functional MRI signal.* Proceedings of the National Academy of Sciences, 2007. **104**(46): p. 18265-18269.
13. Vincent, J.L., et al., *Intrinsic functional architecture in the anaesthetized monkey brain.* Nature, 2007. **447**: p. 83.
14. Dobbing, J. and J. Sands, *Comparative aspects of the brain growth spurt.* Early Human Development, 1979. **3**(1): p. 79-83.
15. Sauleau, P., et al., *The pig model in brain imaging and neurosurgery. .* Animal, 2009. **3**(8): p. 1138-1151.
16. Gieling, E.T., et al., *The pig as a model animal for studying cognition and neurobehavioral disorders.* Curr Top Behav Neurosci, 2011. **7**: p. 359-83.
17. Jelsing, J., et al., *The prefrontal cortex in the Gottingen minipig brain defined by neural projection criteria and cytoarchitecture.* Brain Res Bull, 2006. **70**(4-6): p. 322-36.
18. McBride, T., S.E. Arnold, and R.C. Gur, *A comparative volumetric analysis of the prefrontal cortex in human and baboon MRI.* Brain Behav Evol, 1999. **54**(3): p. 159-66.
19. Matsas, R., A.J. Kenny, and A.J. Turner, *An immunohistochemical study of endopeptidase-24.11 ("enkephalinase") in the pig nervous system.* Neuroscience, 1986. **18**(4): p. 991-1012.
20. Felix, B., et al., *Stereotaxic atlas of the pig brain.* Brain Res Bull, 1999. **49**(1-2): p. 1-137.
21. Holm, I.E. and M.J. West, *Hippocampus of the domestic pig: a stereological study of subdivisional volumes and neuron numbers.* Hippocampus, 1994. **4**(1): p. 115-25.
22. Campos-Ortega, J.A., *The distribution of retinal fibres in the brain of the pig.* Brain Res, 1970. **19**(2): p. 306-12.
23. Szteyn, S., et al., *The stereotaxic configuration of hypothalamus nerve centres in the pig.* Anat Anz, 1980. **147**(1): p. 12-32.
24. Junge, D., *[The topography and cytoarchitectonic of the diencephalon of the cow (Bos taurus var. domesticus L.). II. The internal structure of the diencephalon of the cow (Bos taurus var. domesticus L.) (author's transl)].* Anat Anz, 1977. **141**(5): p. 478-97.
25. Freund, E., *[Cytoarchitectonics of the mesencephalon and pons in the domestic pig (Sus scrofa domestica)].* Anat Anz, 1969. **125**(4): p. 345-62.
26. Otabe, J.S. and A. Horowitz, *Morphology and cytoarchitecture of the red nucleus of the domestic pig (Sus scrofa).* J Comp Neurol, 1970. **138**(3): p. 373-89.
27. Larsell, O., *The development of the cerebellum of the pig.* Anat Rec, 1954. **118**(1): p. 73-107.
28. Breazile, J.E., Swafford, B.C.; Thompson, W.D., *Study of the motor cortex of the domestic pig.* Amer J Veterinary Res, 1966. **27**(120): p. 1369-1373.
29. Craner, S.L. and R.H. Ray, *Somatosensory cortex of the neonatal pig: I. Topographic organization of the primary somatosensory cortex (SI).* J Comp Neurol, 1991. **306**(1): p. 24-38.
30. Duhaime, A.C., *Large animal models of traumatic injury to the immature brain.* Dev Neurosci, 2006. **28**(4-5): p. 380-7.
31. Baker, E.W., et al., *Induced Pluripotent Stem Cell-Derived Neural Stem Cell Therapy Enhances Recovery in an Ischemic Stroke Pig Model.* Scientific Reports, 2017. **7**(1): p. 10075.

32. Platt, S.R., et al., *Development and characterization of a Yucatan miniature biomedical pig permanent middle cerebral artery occlusion stroke model.* Experimental & Translational Stroke Medicine, 2014. **6**(1): p. 5.
33. Calhoun, V. and T. Adali, *Group ICA of fMRI toolbox (GIFT).* Online at http://icatb. sourceforge. net, 2004.
34. Mairal, J., et al., *Online learning for matrix factorization and sparse coding.* Journal of Machine Learning Research, 2010. **11**(Jan): p. 19-60.
35. Zhang, W., et al., *Experimental Comparisons of Sparse Dictionary Learning and Independent Component Analysis for Brain Network Inference from fMRI Data.* IEEE Transactions on Biomedical Engineering, 2018: p. 1-1.
36. Lv, J., et al., *Sparse representation of whole-brain fMRI signals for identification of functional networks.* Medical Image Analysis, 2015. **20**(1): p. 112-134.
37. Saikali, S., et al., *A three-dimensional digital segmented and deformable brain atlas of the domestic pig.* Journal of neuroscience methods, 2010. **192**(1): p. 102-109.
38. Ashburner, J., et al., *SPM12 manual.* URL: http://www. fil. ion. ucl. ac. uk/spm/doc/spm12 manual. pdf, 2016.
39. Penny, W.D., et al., *Statistical parametric mapping: the analysis of functional brain images*. 2011: Elsevier.
40. Ashburner, J. and K.J. Friston, *Nonlinear spatial normalization using basis functions.* Human brain mapping, 1999. **7**(4): p. 254-266.
41. Ashburner, J., et al., *Incorporating prior knowledge into image registration.* Neuroimage, 1997. **6**(4): p. 344-352.
42. Vo, A., et al., *Early registration of diffusion tensor images for group tractography of dystonia patients.* Journal of Magnetic Resonance Imaging, 2013. **37**(1): p. 67-75.
43. Toussaint, N., J.-C. Souplet, and P. Fillard. *MedINRIA: Medical image navigation and research tool by INRIA.* in *Proc. of MICCAI*. 2007.
44. Brookes, M.J., et al., *Investigating the electrophysiological basis of resting state networks using magnetoencephalography.* Proceedings of the National Academy of Sciences, 2011: p. 201112685.
45. Smith, S.M., et al., *Correspondence of the brain's functional architecture during activation and rest.* Proceedings of the National Academy of Sciences, 2009. **106**(31): p. 13040-13045.
46. Lois, G., J. Linke, and M. Wessa, *Altered functional connectivity between emotional and cognitive resting state networks in euthymic bipolar I disorder patients.* PLoS One, 2014. **9**(10): p. e107829.
47. Tanaka, Y., et al., *Experimental Model of Lacunar Infarction in the Gyrencephalic Brain of the Miniature Pig.* Stroke, 2008. **39**(1): p. 205-212.
48. Ustinova, K.I., et al., *Physical therapy for correcting postural and coordination deficits in patients with mild-to-moderate traumatic brain injury.* Physiotherapy Theory and Practice, 2015. **31**(1): p. 1-7.
49. Iandolo, R., et al., *Neural correlates of lower limbs proprioception: An fMRI study of foot position matching.* Human Brain Mapping, 2018. **39**(5): p. 1929-1944.
50. Amit Etkin , M.D., Ph.D. , and P.D. Tor D. Wager *Functional Neuroimaging of Anxiety: A Meta-Analysis of Emotional Processing in PTSD, Social Anxiety Disorder, and Specific Phobia.* American Journal of Psychiatry, 2007. **164**(10): p. 1476-1488.

51. Jak, A.J., et al., *SMART-CPT for veterans with comorbid post-traumatic stress disorder and history of traumatic brain injury: a randomised controlled trial.* Journal of Neurology, Neurosurgery & Psychiatry, 2018: p. jnnp-2018-319315.
52. Duberstein, K.J., et al., *Gait analysis in a pre- and post-ischemic stroke biomedical pig model.* Physiology & Behavior, 2014. **125**: p. 8-16.
53. Webb, R.L., et al., *Human Neural Stem Cell Extracellular Vesicles Improve Recovery in a Porcine Model of Ischemic Stroke.* Stroke, 2018. **49**(5): p. 1248-1256.
54. Izquierdo, A., et al., *The neural basis of reversal learning: An updated perspective.* Neuroscience, 2017. **345**: p. 12-26.
55. Swindale, N.V., *Orientation tuning curves: empirical description and estimation of parameters.* Biological Cybernetics, 1998. **78**(1): p. 45-56.
56. Mudd, A., et al., *Dietary Sialyllactose Influences Sialic Acid Concentrations in the Prefrontal Cortex and Magnetic Resonance Imaging Measures in Corpus Callosum of Young Pigs.* Nutrients, 2017. **9**(12): p. 1297.
57. Mudd, A., et al., *Early-Life Iron Deficiency Reduces Brain Iron Content and Alters Brain Tissue Composition Despite Iron Repletion: A Neuroimaging Assessment.* Nutrients, 2018. **10**(2): p. 135.
58. Mudd, A.T., C.M. Getty, and R.N. Dilger, *Maternal Dietary Choline Status Influences Brain Gray and White Matter Development in Young Pigs.* Current Developments in Nutrition, 2018. **2**(6): p. nzy015-nzy015.
59. Hamilton, C., Y. Ma, and N. Zhang, *Global reduction of information exchange during anesthetic-induced unconsciousness.* Brain Structure and Function, 2017. **222**(7): p. 3205-3216.
60. Liang, Z., J. King, and N. Zhang, *Intrinsic Organization of the Anesthetized Brain.* The Journal of Neuroscience, 2012. **32**(30): p. 10183-10191.
61. Buckner, R.L., J.R. Andrews-Hanna, and D.L. Schacter, *The brain's default network.* Annals of the New York Academy of Sciences, 2008. **1124**(1): p. 1-38.
62. Broyd, S.J., et al., *Default-mode brain dysfunction in mental disorders: A systematic review.* Neuroscience & Biobehavioral Reviews, 2009. **33**(3): p. 279-296.
63. Greicius, M., *Resting-state functional connectivity in neuropsychiatric disorders.* Current Opinion in Neurology, 2008. **21**(4): p. 424-430.
64. Shen, D., G. Wu, and H.-I. Suk, *Deep Learning in Medical Image Analysis.* Annual Review of Biomedical Engineering, 2017. **19**(1): p. 221-248.

Table 5.1

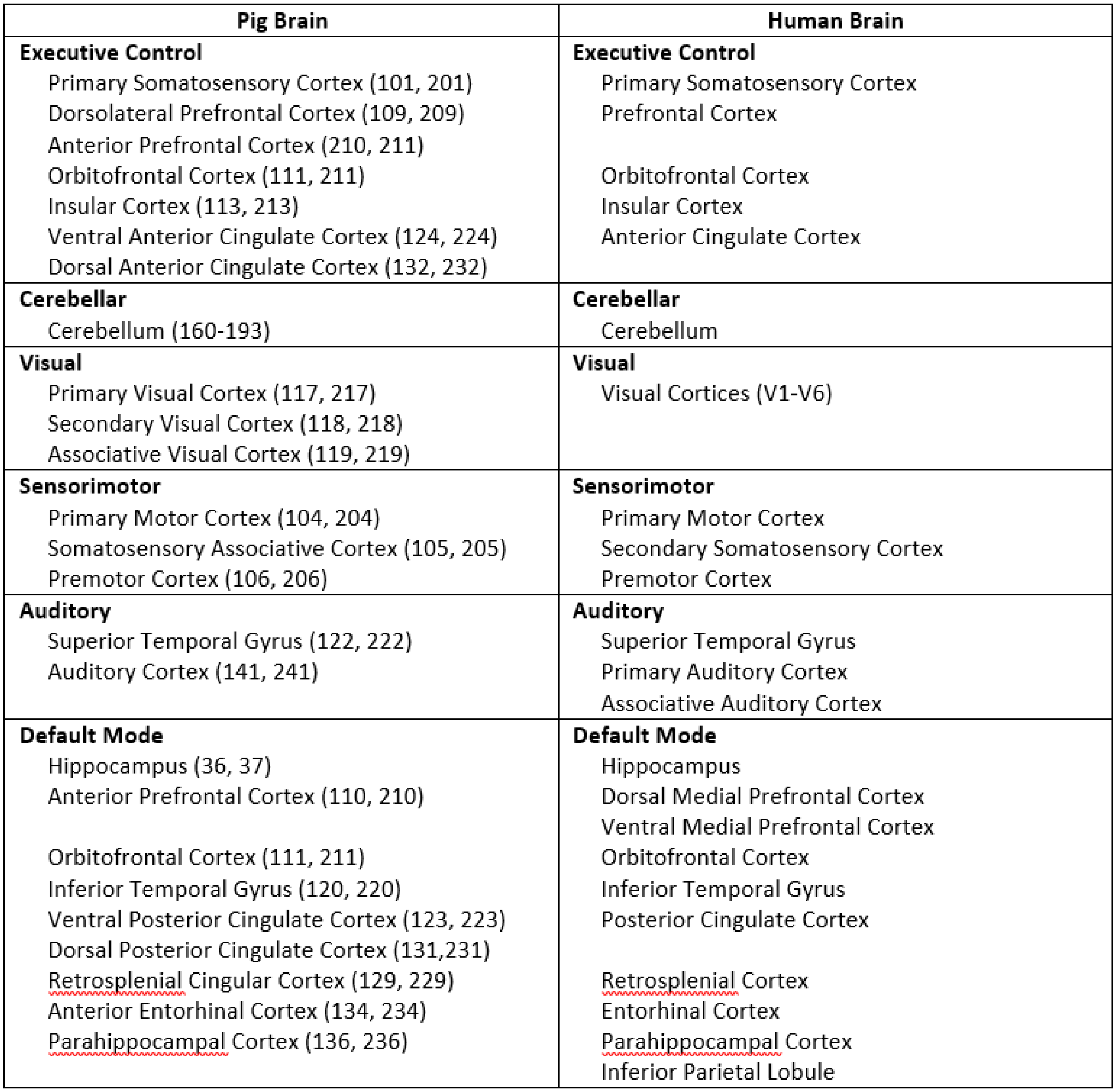

Pig Brain	Human Brain
Executive Control	**Executive Control**
Primary Somatosensory Cortex (101, 201)	Primary Somatosensory Cortex
Dorsolateral Prefrontal Cortex (109, 209)	Prefrontal Cortex
Anterior Prefrontal Cortex (210, 211)	
Orbitofrontal Cortex (111, 211)	Orbitofrontal Cortex
Insular Cortex (113, 213)	Insular Cortex
Ventral Anterior Cingulate Cortex (124, 224)	Anterior Cingulate Cortex
Dorsal Anterior Cingulate Cortex (132, 232)	
Cerebellar	**Cerebellar**
Cerebellum (160-193)	Cerebellum
Visual	**Visual**
Primary Visual Cortex (117, 217)	Visual Cortices (V1-V6)
Secondary Visual Cortex (118, 218)	
Associative Visual Cortex (119, 219)	
Sensorimotor	**Sensorimotor**
Primary Motor Cortex (104, 204)	Primary Motor Cortex
Somatosensory Associative Cortex (105, 205)	Secondary Somatosensory Cortex
Premotor Cortex (106, 206)	Premotor Cortex
Auditory	**Auditory**
Superior Temporal Gyrus (122, 222)	Superior Temporal Gyrus
Auditory Cortex (141, 241)	Primary Auditory Cortex
	Associative Auditory Cortex
Default Mode	**Default Mode**
Hippocampus (36, 37)	Hippocampus
Anterior Prefrontal Cortex (110, 210)	Dorsal Medial Prefrontal Cortex
	Ventral Medial Prefrontal Cortex
Orbitofrontal Cortex (111, 211)	Orbitofrontal Cortex
Inferior Temporal Gyrus (120, 220)	Inferior Temporal Gyrus
Ventral Posterior Cingulate Cortex (123, 223)	Posterior Cingulate Cortex
Dorsal Posterior Cingulate Cortex (131,231)	
Retrosplenial Cingular Cortex (129, 229)	Retrosplenial Cortex
Anterior Entorhinal Cortex (134, 234)	Entorhinal Cortex
Parahippocampal Cortex (136, 236)	Parahippocampal Cortex
	Inferior Parietal Lobule

Anatomies from a standard pig brain atlas [37] (atlas labels in parentheses) that were combined to create six reference pig RSNs (left column) and corresponding human anatomies known to be associated with the same six RSNs (right column).

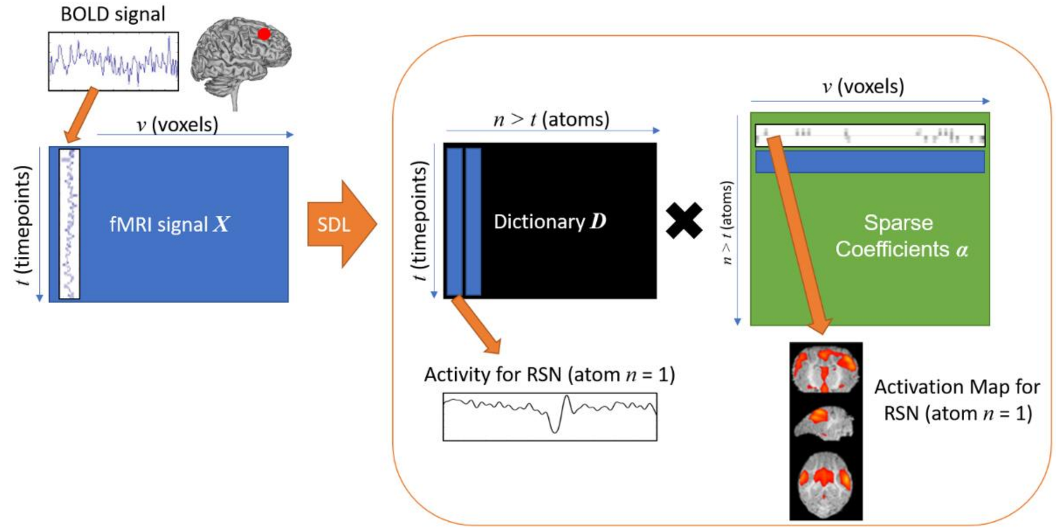

Figure 5.1: Illustrated representation of the decomposition process of sDL. A matrix representing the complete volume of *v* voxel signals acquired from a scan of time *t* is arranged into a signal matrix $\boldsymbol{X}$. Through sDL, the matrix is decomposed into a dictionary matrix $\boldsymbol{D}$ and $\boldsymbol{\alpha}$, such that $\boldsymbol{X}$ approximates $\boldsymbol{D} \times \boldsymbol{\alpha}$. Dictionary $\boldsymbol{D}$ contains activity for *n* number of atoms, or detected RSNs, while $\boldsymbol{\alpha}$ contains representations of the detect RSN maps that can be mapped back to a brain volume.

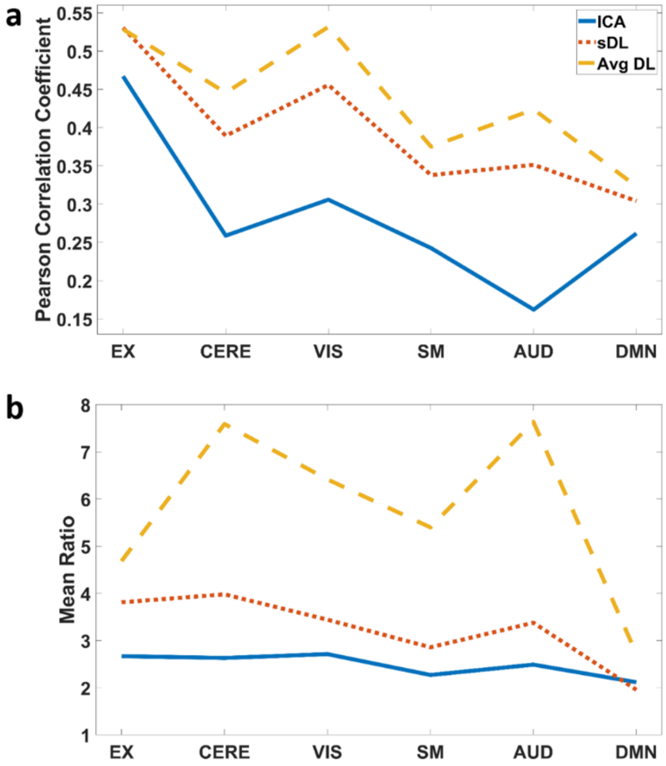

Figure 5.2: Maximum Pearson spatial correlation coefficient values (a) and corresponding mean ratio values (b) from activation maps generated by ICA (solid line), sDL (dotted line), and averaged sDL (dashed line) for six RSNs defined by the reference pig RSN atlas (executive control, cerebellar, visual, sensorimotor, auditory, and default mode).

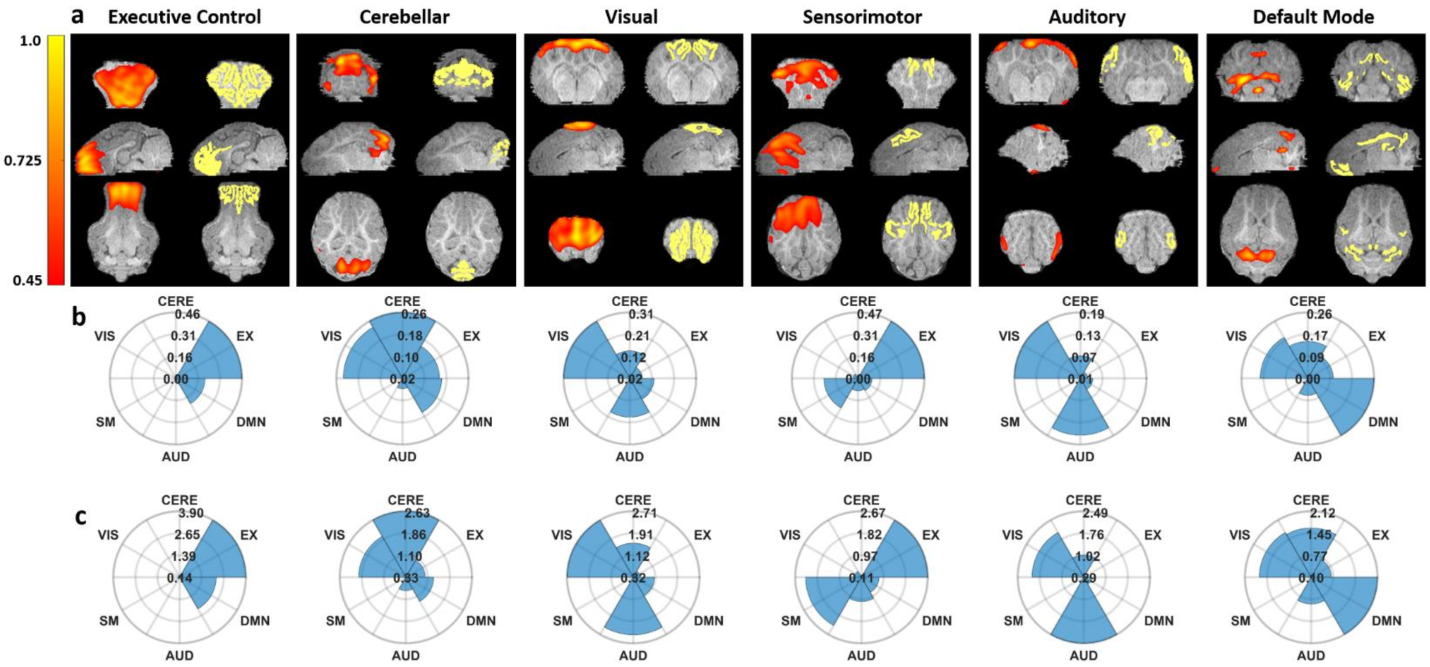

Figure 5.3: a.) Representative cross sectional images of activation maps generated using ICA (left) for six RSNs and the corresponding reference pig RSN atlas (right). All activation map and atlas cross sections are overlaid on the corresponding anatomical images. b-c.) Rose maps of the corresponding Pearson spatial correlation coefficient values (b) and mean ratio values (c) for the displayed activation maps.

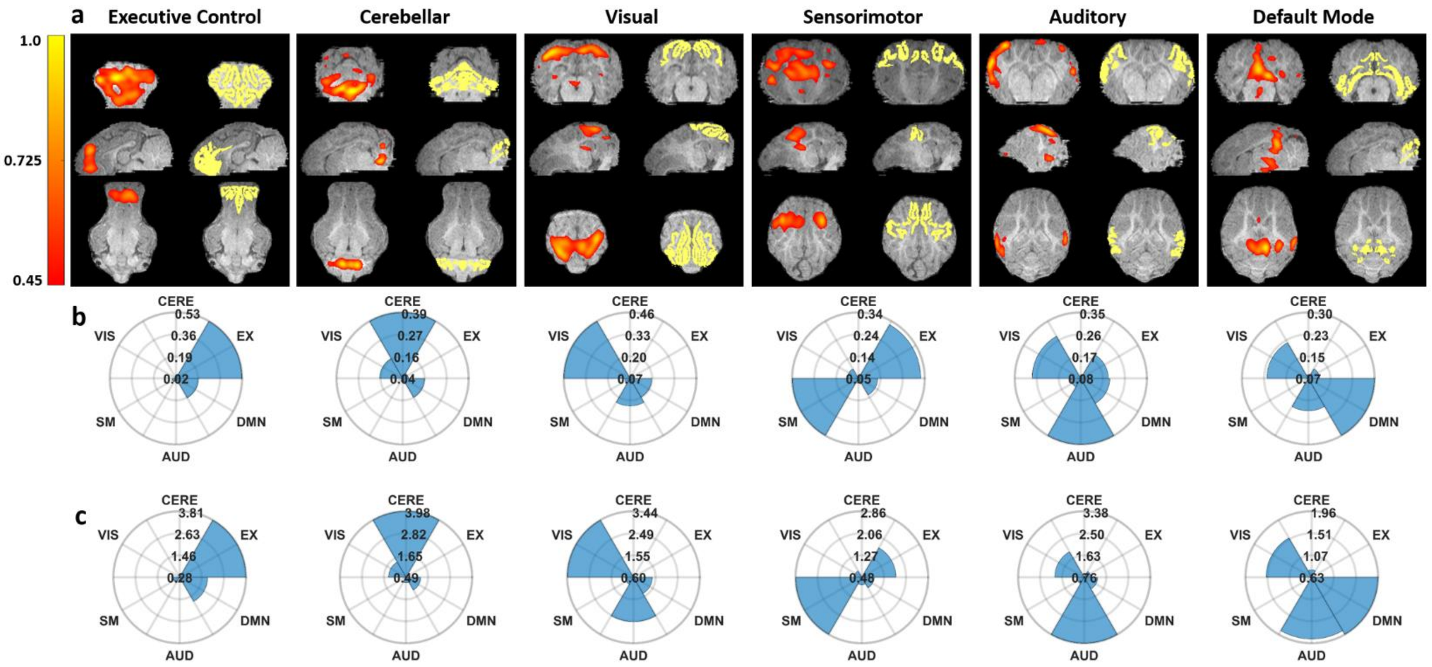

Figure 5.4: a.) Representative cross sectional images of activation maps generated using sDL (left) for six RSNs and the corresponding reference pig RSN atlas (right). All activation map and atlas cross sections are overlaid on the corresponding anatomical images. b-c.) Rose maps of the corresponding Pearson spatial correlation coefficient values (b) and mean ratio values (c) for the displayed activation maps.

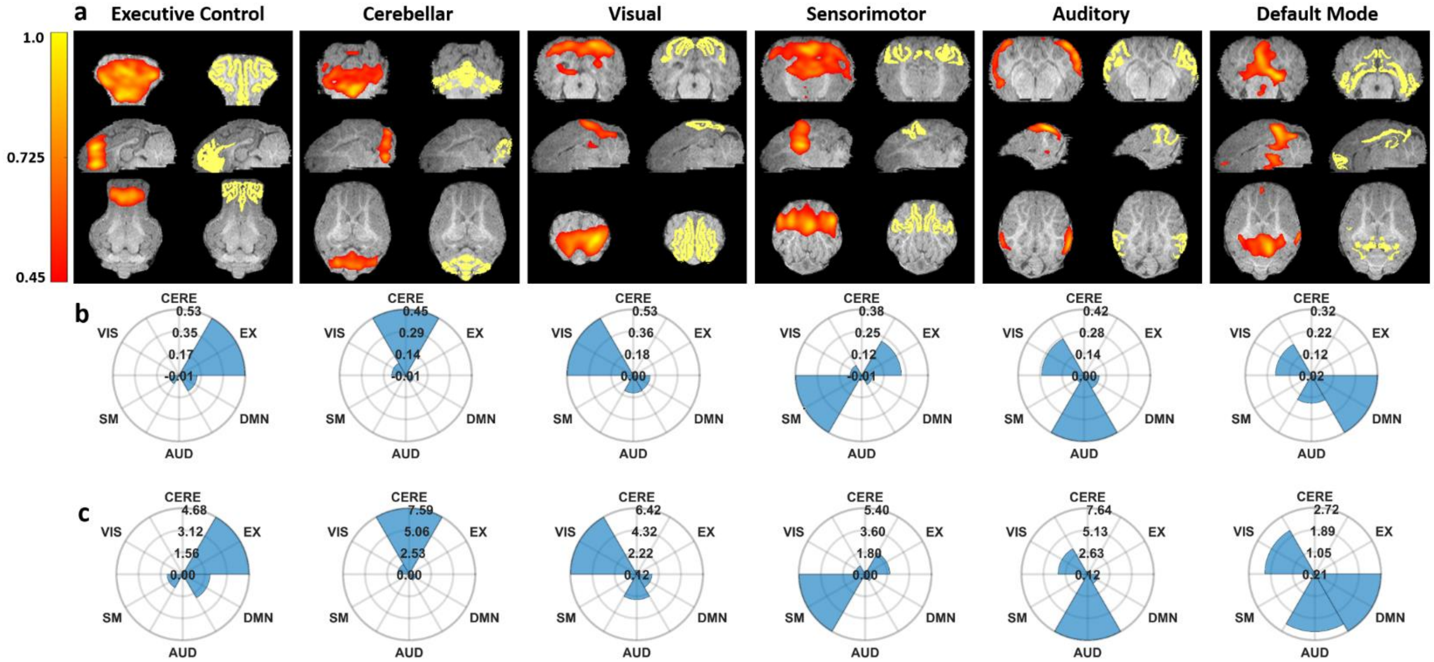

Figure 5.5: a.) Representative cross sectional images of the averaged sDL activation maps (left) for six RSNs and the corresponding reference pig RSN atlas (right). All activation map and atlas cross sections are overlaid on the corresponding anatomical images. b-c.) Rose maps of the corresponding Pearson spatial correlation coefficient values (b) and mean ratio values (c) for the displayed activation maps.

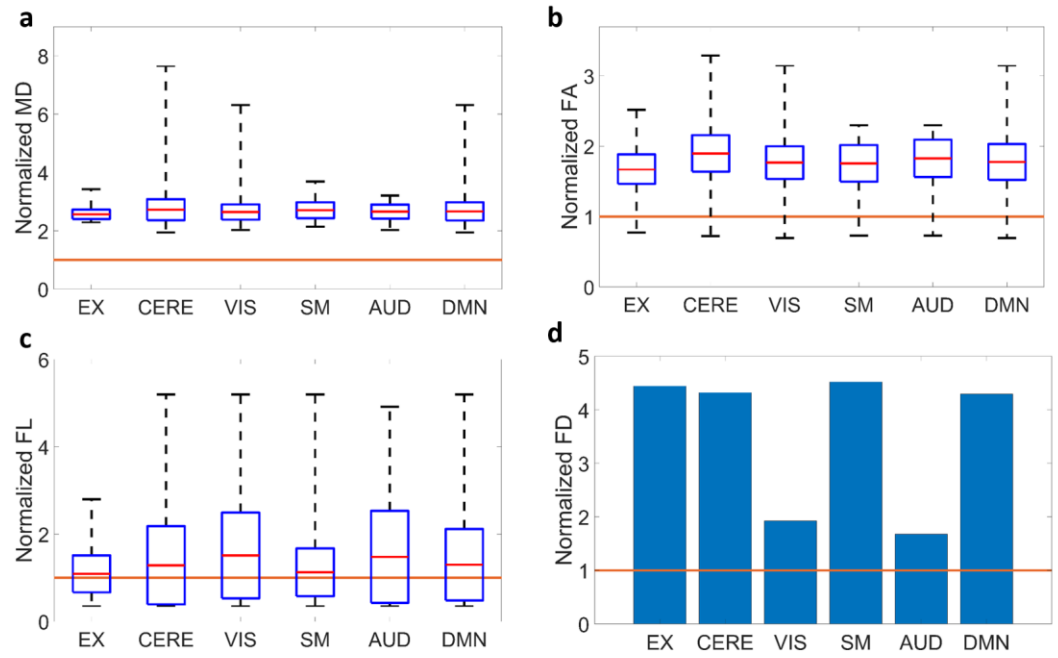

Figure 5.6: Normalized *MD* (a), *FA* (b), *FL* (c), and *FD* (d) measurements for the fibers intersecting with each activation volume of the averaged sDL activation maps. The lower and upper whiskers of the boxplots represent the minimum and maximum measurements, respectively. The central red line in each box represents the mean of the measurements, and the box represents one standard deviation from the mean. All measurements were normalized by their respective whole brain averages, represented as the brown line across all six RSNs.

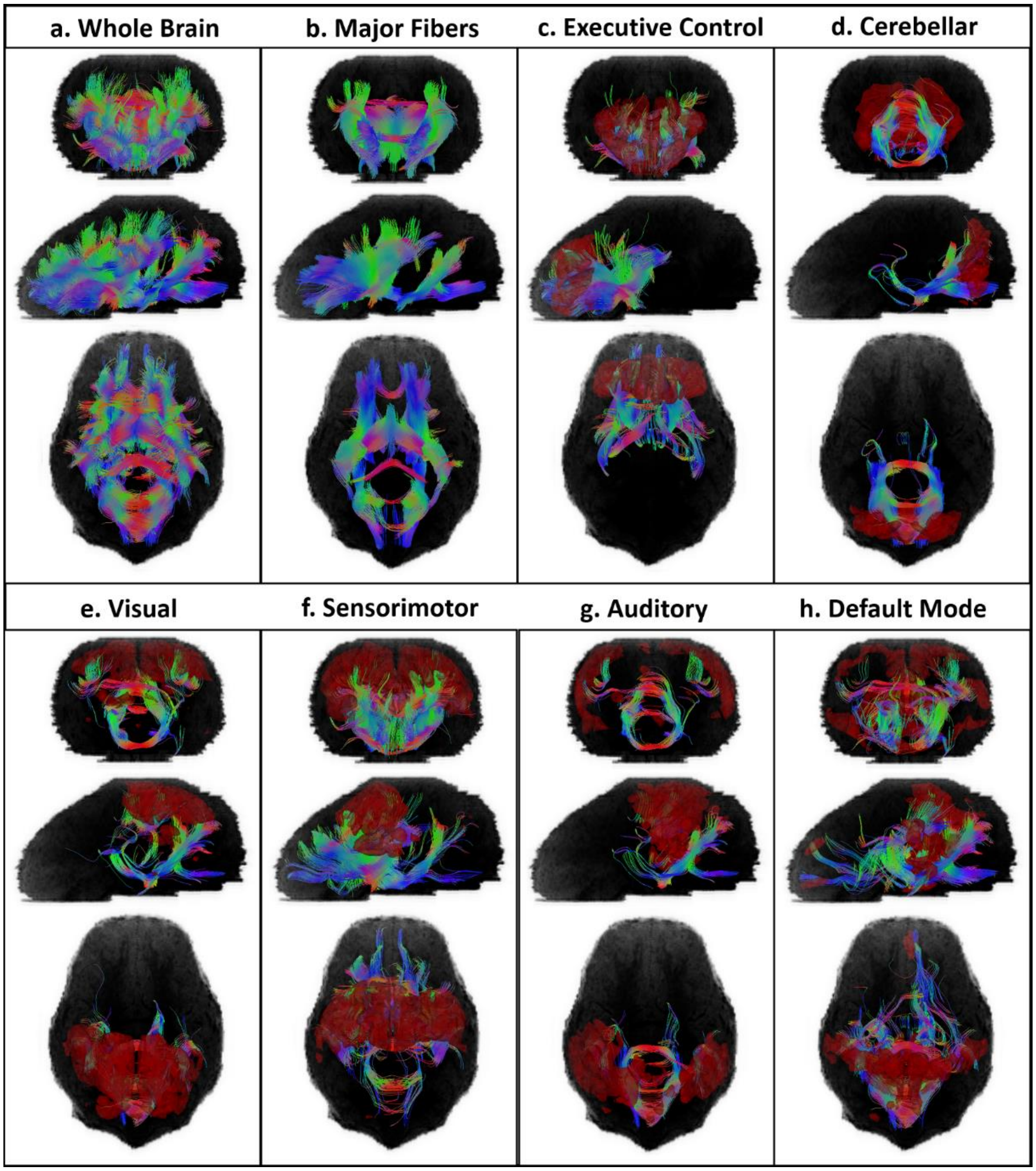

Figure 5.7: Group tractography of the whole brain (a) and major fibers (b) obtained using an early registration and superset method, and the fibers intersecting with the activation volume (shown in red) for each RSN determined from the averaged sDL activation maps (c-h). The activation maps were corrected by removing any regions of the activation volume that were not overlapping with gray matter structures. Coronal, sagittal, and axial views are projections from the front, left, and top of the brain, respectively.

CHAPTER 6

DETECTING FUNCTIONAL CONNECTIVITY DISRUPTIONS IN A TRANSLATIONAL TRAUMATIC BRAIN INJURY PIG MODEL USING FUNCTIONAL MAGNETIC RESONANCE IMAGING

Introduction

Due to both the short-term and long-term effects, traumatic brain injuries (TBIs) have become an active area of research over the last several years. Therefore, there has been a growing interest to establish a translational animal model for studying TBIs. Many pig models of TBI, as well as other neural injuries and developmental models, such as stroke and nutrition, have been developed [1-8], and these models have been shown to cause functional changes associated with resting-state networks (RSNs) that have recently been reported in the pig brain (Chapter 5) [9], including the visual, executive control, sensorimotor, cerebellar, and default mode networks.

In both controlled cortical impact (CCI) and rapid nonimpact head rotation (RNR) TBI, deficits associated with the sensorimotor network were observed, including gait changes, such as increased stance time, decreased stride velocity, percent of two limb support, and proprioception [2-4]. These changes are commonly observed in human TBI patients and are due to a loss of coordination, lack of bilateral arm/leg coupling, and reduced agility and balance [10]. Functional magnetic resonance imaging (fMRI) studies in humans have demonstrated that the cerebellar network is also involved in lower limb proprioception and thus gait [11]. The coordination between these networks is important for basic motor tasks to occur, and TBI leads to aberrant communication between these networks.

In a T-maze assessment that tests cognitive flexibility, problem solving, and goal directed behavior, all of which are associated with the executive control network [12, 13], RNR TBI pigs showed difficulties in reversal learning [4]. TBI pigs learned that a food reward was in a specific T-maze arm. However, once the reward was reversed to the alternate arm, TBI animals spent significantly more time in the old food location trying to find the reward in comparison to sham pigs, indicating problems in relearning and executive function after insult. RNR TBI pigs have also shown increased fear and anxiety behaviors, including running and escape behaviors in open field testing [14]. Fear and anxiety are modulated by the dorsal anterior cingulate cortex, which is also associated with the executive control network [15].

CCI and RNR TBI also resulted in abnormal day and night activity similar to patterns found in human patients [8, 16]. TBI pigs showed hypoactivity during the day followed by increased instances of high activity during nighttime hours, including continuous pacing and running. This suggests blurring of the distinction between day and night. In humans, transitioning from an awake to sleeping state involves the activation of the default mode network [16]. Aberrant day and night activity in TBI pigs suggests that there may be irregularities in the default mode network's function.

The visual cortex in the pig brain is especially similar to the corresponding human cortex making the pig a highly relevant and useful model for studying the visual network's functional connectivity and potential disruptions caused by TBI. Pigs and humans have similar visual acuity, the ability to distinguish colors, and maturational and topographic similarities related to the visually evoked response [17]. The pig is similar to the human in regards to the sequence of temporal development as well, including the pig's retinae maturing by early postnatal days [18, 19]. Fang et al. [18] examined the visual cortex in awake, restrained pigs aged from two to six months old using fMRI and observed functional changes over time, thus demonstrating the feasibility of detecting changes and differences in the visual network.

In this Chapter, rs-fMRI is employed to study the functional connectivity disruptions caused by TBIs using a translational pig model. A reference pig functional connectivity atlas was constructed for five different networks using a previously published pig anatomical atlas. Functional connectivity activation maps were generated for individual pigs using two methods: individual analysis and group dual regression analysis. Within each method sparse dictionary learning (sDL) was used to generate activation maps, and these activation maps were compared to each reference atlas using Pearson spatial correlation coefficients and mean ratios. Differences between a healthy control group and TBI group were explored using p-values.

Materials and Methods

Subjects

Four-week-old male castrated and intact female Landrace-cross pigs (n=8) were used in this study. TBI was induced in five (n=5) of the pigs using the previously published procedure [26], while the other three (n=3) served as controls (normal, healthy pigs). All experimental procedures were approved by the Institutional Animal Use and Care Committee (IAUCC, University of Georgia). Pigs were group housed in a Public Health Service (PHS) and Association for Assessment and Accreditation of Laboratory Animal Care (AAALAC) approved facility at a room temperature approximately 27°C with a 12-hour light/dark cycle. Pigs encountered daily enrichment through toys and human contact and were fed standard pig starter 1 diets.

Controlled cortical impact

Pigs were anesthetized, and under aseptic technique, a periosteal block (0.5% bupivacaine; 2 mg/kg; Pfizer) at the cranium was applied. A craniectomy was performed, approximately 20mm in diameter, to expose the underlying dura at the left posterior junction of the coronal and sagittal sutures. Each pig was secured in a controlled cortical impactor device (University of Georgia Instrument Design and Fabrication Shop, Athens, GA), and a 15mm impactor tip was positioned over the intact dura to induce injury with the following parameters: velocity of 4m/s, depth of depression of 9mm, and dwell time of 400ms. These parameters were based on previous studies to generate a moderate TBI [2, 20, 21].

Pre-operatively, TBI pigs received antibiotics (Excede; 5mg/kg intramuscular (IM); Zoetis). Pre-induction sedation and analgesia for TBI surgery was achieved using buprenorphine (0.01 mg/kg IM; Covetrus), midazolam (0.2 mg/kg IM; Heritage), and xylazine (2 mg/kg IM; VetOne). Prophylactic lidocaine (0.5 mL 2% lidocaine; VetOne) was topically applied to laryngeal folds and propofol (to effect, intravenous (IV); Zoetis) was administered to achieve intubation. Anesthesia was maintained with isoflurane (2.0%; Abbott Laboratories) in oxygen. Pig temperature, respiration, and heart rate were monitored every 15 minutes during anesthesia and post-operatively until vitals returned to normal range. Additionally, vitals were monitored every 4 hours for 24 hours, and then twice a day. Post operatively, pigs received buprenorphine (0.01 mg/kg IM; Covetrus) every 8 hours for 24 hours and banamine (2.2 mg/kg IM; Merck) every 12 hours for 24 hours, and then every 24 hours for 72 hours for pain and inflammation maintenance. Healthy control pigs did not receive pre-operative antibiotics or post-operative medications.

Data acquisition

One day post-TBI, pigs were initially sedated using xylazine (2 mg/kg IM; VetOne), ketamine (4 mg/kg IM; company), and midazolam (0.2 mg/kg IM; Heritage). Then mild anesthesia was maintained with inhalational isoflurane (1.5%; Abbott Laboratories) in oxygen in order to keep the pigs sedated while reducing anesthetic agent interference with pig brain neural activity and neurovascular coupling.

Using a GE 32-channel fixed-site Discovery MR750 3.0 Tesla MRI magnet and 8-channel knee coil, T1-weighted anatomical and rs-fMRI data was acquired using the following two sequences: 1.) 3D fast spoiled gradient echo (FSPGR) sequence (repetition time TR=5.5s, echo time TE=2.1ms, flip angle FA=9°, field-of-view FOV=12.8x12.8x6.4cm, slice thickness=1mm, a matrix size of 256x256x112, axial slice plane, and an acquisition time of 10min 57s), and 2.) gradient echo-planar imaging (EPI) sequence (TR=3s, TE=30ms, FA=80°, FOV=12.8x12.8x6.2cm, a matrix size of 96x96x31, coronal slice plane, 305 total volumes, and an acquisition time of 15min 15s).

fMRI data analysis

fMRI data was analyzed using a previously published procedure (see Chapter 5) [9]. Each fMRI dataset was preprocessed to realign images to correct for motion and perform slice-timing correction using Statistical Parametric Mapping (SPM) software [22]. fMRI datasets and T1-weighted anatomical images were skull striped by manual slice-by-slice segmentation. The first five volumes of each fMRI dataset were removed to allow the magnetization to reach a steady state; therefore, 300 total volumes were remaining for rs-fMRI data.

To determine spatial activation maps ($\boldsymbol{\alpha}$) for each individual pig, functional connectivity analysis was performed using two different strategies: individual analysis and group dual regression analysis. For individual analysis, sparse dictionary learning (sDL) was performed for each individual fMRI dataset using the SPArse Modeling Software (SPAMS) toolbox [23] by minimizing the equation

$$\min_{\boldsymbol{D}\in C} \lim_{n\to+\infty} \frac{1}{n}\sum_{i=1}^{n}\left(\min_{\alpha^i}\frac{1}{2}\left\|\boldsymbol{s}^i - D\boldsymbol{\alpha}^i\right\|_2^{\;2} + \lambda\left\|\boldsymbol{\alpha}^i\right\|_1\right) \qquad (6.1)$$

where $\boldsymbol{s}$ is the pig's fMRI data, $\boldsymbol{D}$ is the dictionary or associated time series, λ is a sparsity parameter, and n is the number of atoms or dictionary elements the fMRI data is decomposed into. For this study, n=300 and λ=0.15 was used when solving for all individual and group activation maps ($\boldsymbol{\alpha}$).

For group dual regression analysis, one pig from the control group and one from the TBI group was selected as the template pigs and the other remaining pigs within each group were spatially normalized to the template pig using the first volume of each rs-fMRI dataset to calculate a transformation. The calculated transformation for each pig was then applied to the rest of the volumes of that corresponding pig. Spatial normalization was accomplished using SPM's Old Normalize algorithm [22]. Group datasets were created by temporally concatenating the rs-fMRI time series of the spatially normalized pigs at each voxel; therefore, the control group dataset had 900 volumes (3 pigs with 300 volumes each) and the TBI group dataset had 1500 volumes (5 pigs with 300 volumes each). sDL was then performed on these two group datasets by minimizing Eq. (6.1). From this procedure, group activation maps ($\boldsymbol{\alpha_g}$) were obtained that were then used to perform dual regression, similar to the procedure used for group independent component analysis (ICA) [24], to obtain activation maps for each individual pig ($\boldsymbol{\alpha_i}$). The first regression used $\boldsymbol{\alpha_g}$ and each pig's individual rs-fMRI data ($\mathbf{s_i}$) to determine an individual dictionary ($\boldsymbol{D_i}$) or associated time series using linear least squares to solve the equation $\mathbf{s_i} = \boldsymbol{D_i}\,\boldsymbol{\alpha_g}$. The second regression then used each pig's $\boldsymbol{D_i}$ and $\mathbf{s_i}$ to determine $\boldsymbol{\alpha_i}$ by minimizing Eq. (6.1).

Individual pig activation maps obtained from both methods were thresholded using a Z-score of one, normalized between zero and one, and then spatially normalized to either the corresponding pig's anatomical space for individual analysis or the template pig's anatomical space for group dual regression analysis. For individual analysis, spatial normalization was accomplished using SPM to calculate a spatial transformation between the first rs-fMRI volume of each pig and its corresponding T1-weighted anatomical data; then applying the calculated transformation to the activation maps. For group analysis, the calculated transformation between the template pig's first rs-fMRI volume and its corresponding T1-weighted anatomical data was applied to the activation maps for all pigs within the template pig's group. When applying these transformations, voxel size was reshaped to 1mm cubed, opposed to the 0.5mm cubed voxels of anatomical space, in order to reduce the computational size of the activation map datasets.

Pig reference functional connectivity atlases and activation map analysis

Next, reference pig functional connectivity atlases were created also using the same previously published procedure (see Chapter 5) [9]. First, a standard pig brain atlas [25] was spatially normalized to the T1-weighted anatomical space of each pig. Spatial normalization was accomplished by calculating a spatial transformation using T1-weighted anatomical data provided in the same space as, and associated with, the standard pig brain atlas and the T1-weighted anatomical data acquired for each pig. The calculated transformation was then applied to the atlas, and when applying this transformation, voxel size was again reshaped to 1mm cubed. Using the anatomical regions provided in Table 5.1, five reference functional connectivity atlases were created for each pig: executive control (EX), cerebellar (CERE), visual (VIS), sensorimotor (SM), and default mode (DMN). See the **Discussion** for why the auditory (AUD) network was not considered in this work.

With the activation maps and reference atlases now in the same space, Pearson spatial correlation coefficients and mean ratios (defined as mean activation value within a given atlas divided by the mean activation value of the entire brain) were calculated for each activation map and reference atlas. When performing sDL using a complete or over-complete dictionary to achieve sparseness, redundant representations of the same signal are possible. Therefore, the three activation maps (corresponding to three separate atoms in the learned dictionary) for each fMRI dataset and reference atlas that produced the largest Pearson values were determined and averaged to produce final activation maps. Pearson values and mean ratios were then re-calculated for these final maps and each corresponding reference atlas, as well as for each individual anatomical region comprising each corresponding reference atlas. However, for the CERE atlas, the individual lobes were not examined. Instead, the CERE network is discussed as a whole in conjunction with the SM network, as it has been shown that coordination between these networks is necessary for basic motor tasks to occur [11].

P-values associated with the Pearson values and mean ratios were calculated between the TBI group and the control group for each network as a whole, as well as for each individual anatomical region, using a two-sample t-test assuming the groups had unequal variances. The groups were considered to be significantly different if $p<0.05$; however, since this is a preliminary study and the groups are small ($n=3$ for the control group and $n=5$ for the TBI group), the groups were considered to be trending towards significant difference if $p<0.4$. For each method, a network or anatomical region was only considered significantly different or trending towards significant difference if the p-values for both the Pearson values and mean ratios were below the specified thresholds.

Results

Group difference analysis

All calculated p-values between the TBI and control groups for the Pearson spatial correlation coefficients and mean ratios for four of the examined networks (VIS, EX, SM, and CERE) and their individual anatomical regions are given in Table 6.1. The calculated p-values for the DMN are presented in Table C1 of Appendix C.

For the individual analysis, three of the four networks (75%) discussed in the main text showed either significant differences between the TBI group and the control group or were trending towards significant difference, with the SM network being the only network showing no statistical difference. For the individual anatomical regions, the mean ratios appeared to be more sensitive with 10 of the 13 (77%) individual anatomical regions showing either significant differences or trending towards significant differences, whereas the Pearson values only showed 7 of 13 (54%) of the regions being different. Recall that an individual anatomical region was only considered to be significantly different or trending towards significant difference if the p-values for both the Pearson values and mean ratios were below the specified thresholds. Therefore, for the individual analysis, 6 of the 13 (46%) anatomical regions were determined to be either significantly different or trending towards significant difference.

For the group dual regression analysis, three of the four networks (75%) discussed in the main text were observed to be significantly different or trending towards significant difference; this time with the CERE network being the only network not showing statistical difference. Again, the mean ratios appeared to be more sensitive than the Pearson values with 8 of 13 (62%)

in comparison to 6 of the 13 (46%) individual anatomical regions showing significant differences or trending towards significant differences. However, again only 5 of 13 (38%) individual anatomical regions showed significant difference or trending towards significant difference for both simultaneously.

Individual analysis

When examining the activation maps generated using individual analysis, TBI pigs showed significantly lower Pearson spatial correlation coefficients and mean ratios in comparison to the control pigs for the EX and VIS networks (Figures 6.1a, 6.2a, and Figures C3a-4a of Appendix C); however, no statistical differences were observed for the SM or DMN networks (Figures 6.3a, C1, C2, and C5a). The CERE network also showed a significant decrease in the Pearson values for the TBI groups (Figure 6.3a); however, for the mean ratios only a decreasing trend towards significant difference was observed (Figure C5a). Therefore, the CERE network was only considered to be trending towards significant difference.

When looking at the VIS network more closely by examining the individual anatomical regions within its reference atlas, significantly lower Pearson values and mean ratios were observed in the TBI group for the secondary visual cortex in comparison to the control group (Figures 6.1a and C3a), which is consistent with the trend of the network as a whole. The primary visual cortex was considered to be showing a decreasing trend towards significant difference, as the Pearson values showed a significant decrease and the mean ratios only showed a decreasing trend towards significant difference. The associative visual cortex showed no statistical differences.

Although the EX network as a whole also showed a significant decrease in the TBI group, just the dorsolateral prefrontal, anterior prefrontal, and insular cortices showed decreasing trends towards significant differences, while all other regions showed no statistical differences (Figures 6.2a and C4a).

For the SM network, a decreasing trend towards significant difference was observed for the premotor cortex, and the CERE network was considered to be showing a decreasing trend towards significant difference, as the Pearson values showed a significant decrease and the mean ratios only showed a decreasing trend towards significant difference (Figures 6.3a and C5a). An increasing trend towards significant difference was observed for the Pearson values of the somatosensory associative cortex (Figure 6.3a); however, no statistical difference was observed for the mean ratios (Figure C5a). Therefore, this region wasn't considered to be trending towards significant difference.

Results for the DMN are presented and discussed in Appendix C (Table C1 and Figures C2-3), and boxplots associated with the mean ratios from the individual analysis for the VIS, EX, SM, and CERE networks are presented in Figures C3a-5a.

Group dual regression analysis

When examining the activation maps generated using group dual regression analysis, TBI pigs showed a significant decrease in the VIS network in comparison to the control pigs (Figures 6.1b and C3b). Decreasing trends towards significant differences were also observed for the EX and SM networks (Figures 6.2b-6.3b and C4b-C5b). No statistical difference was observed for the CERE networks (Figures 6.3b and C5b).

Within the VIS network, the primary visual cortex showed a significant decrease in the TBI group in comparison to the control group, and the associative visual cortex also showed a decreasing trend towards significant difference, which is consistent with the trend of the network as a whole (Figures 6.1b and C3b). No statistical differences where observed between the two groups for the secondary visual cortex.

The anterior prefrontal cortex showed a significant decrease, and the dorsolateral prefrontal cortex also showed a decreasing trend towards significant difference within the EX network (Figures 6.2b and C4b), which is consistent with the trend of the whole network. The ventral anterior cingulate cortex also showed a decreasing trend towards significant difference for the Pearson values; however, no statistical difference was observed for the mean ratios. Therefore, this region was considered to have no statistical difference. The primary somatosensory, orbitofrontal, insular, and dorsal anterior cingulate cortices also showed no statistical differences within the EX network.

For the SM network, a decreasing trend towards significant difference was observed for the premotor cortex, which is consistent with the network as a whole (Figures 6.3b and C5b). No statistical differences were observed for the primary motor cortex, somatosensory associative cortex, or the CERE network (Figures 6.3b and C5b). Boxplots associated with the calculated mean ratios for the VIS, EX, SM, and CERE networks for the group dual regression analysis are presented in Appendix C (Figures C3b-5b).

Discussion and Conclusion

Both the individual and group dual regression analysis methods demonstrate the ability to detect functional connectivity disruptions in the pig brain caused by TBI. Disruptions were consistently detected in the VIS and EX networks using both methods, as shown by the reduced Pearson values and mean ratios measured in the TBI group in comparison to the control group (Table 6.1, and Figures 6.1-6.3 and C3-5). However, disruption of the CERE network was only observed using individual analysis, and disruption of the SM network was only observed using the group dual regression analysis. Therefore, further investigation of these two networks may be necessary.

Representative images of these disruptions are displayed in Figure 6.4, which displays two-dimensional activation maps for each network and their corresponding reference atlas overlaid on each pigs' T1-weighted anatomical image. Clear differences between the representative control pig and TBI pig are observed in each network, and it was observed that the TBI pigs in general tend to have noisier, less uniform activations, which is supported quantitatively by the above-discussed three-dimensional Pearson spatial correlation coefficients and mean ratios.

Detected disruptions were also able to be traced back to the individual anatomical regions affected by the TBI. The individual and group dual regression analysis methods showed consistency, with both detecting disruptions in four of the same individual anatomical regions (the primary visual cortex of the VIS network, the dorsolateral prefrontal and anterior prefrontal cortices of the EX network, and the premotor cortex of the SM network). Overall, four of the six individual anatomical regions that differences were observed using the individual analysis matched four of the five regions that differences were observed using the group dual regression analysis, which emphasizes the high level of commonality between the two methods.

Despite the consistency in similarly detected disrupted regions, some differences were also observed. The individual analysis detected disruptions in the secondary visual cortex of the VIS network and in the insular cortex of the EX network, whereas the group dual regression analysis did not. The group dual regression analysis also detected differences within the associative visual cortex of the VIS network, while the individual analysis did not.

Each of the two methods have some theoretical advantages and disadvantages. Due to biological factors, each pig may respond differently to the induced TBI. This may lead to different structural changes in the brain, as well as different functional connectivity disruptions from pig to pig. Individual analysis allows for the study of these individual disruptions caused by TBI. However, when analyzing fMRI data, it is often beneficial to perform a group analysis, like in Chapter 5 [9]. sDL is a data-driven approach for detecting functional networks, and group analysis tends to perform better at detecting networks since the size of the dataset increases when multiple subjects (pigs) are combined into a group dataset, which improves detection of networks that share common features. However, group analysis suffers from the fact that it removes any natural structural differences between the pigs and/or structural differences caused by TBI through the process of spatially normalizing all of the pigs' fMRI datasets to a template brain.

Group analysis is highly beneficial when attempting to find general patterns and trends shared by a cohort of subjects, whereas individual analysis is beneficial when attempting to monitor and/or study an individual's response to an injury or a potential treatment. Although, all surgical procedures and induced TBIs are performed as consistently as possible from pig to pig in this study, it is impossible to remove the natural biological variability in the responses of the pigs to the injury. If the biological variability is low and the disruptions caused by the TBI are relatively consistent, then group dual regression analysis may prove the better method for detecting the functional connectivity disruptions caused by TBI. If the biological variability is large and the disruptions inconsistent across pigs, then individual analysis may prove the better method.

However, both methods demonstrate the feasibility of detecting functional connectivity disruptions caused by TBI, and the ability to detect functional disruptions in the translational pig

TBI model allows for the future study of prognosis analysis for TBI and potential treatments to help restore these disruptions. It also allows for the potential future study of other neurological injuries, such as stroke, and neurological developmental influences, such as nutrition using pig models.

Several pig stroke models have already been reported [5, 6, 26-28], including middle cerebral artery occlusion (MCAO) and lacunar infarct models, and these studies have shown lesioning in the brain effecting regions associated with several networks discussed in this work. MCAO induced ischemic stroke in pigs has been shown to cause large scale brain lesioning with infarcts focused on the temporal and piriform lobes [5]. More specifically, stroke in these animals had a direct effect on the insular cortex, which is associated with the EX network, and on the hippocampus, parahippocampal cortex, and inferior temporal gyrus regions, which are associated with the DMN. Using a lacunar infarction model for ischemic stroke in pigs, injury to the internal capsule and significant motor deficits were observed [6]. A recent fMRI study in humans also demonstrated internal capsule activation being temporally correlated with activation of the primary motor cortex, which is associated with the SM network [29].

The pig has also been utilized as a model to study the effects of nutrition on pre- and postnatal brain development with some recent studies focusing on MRI structural changes [7, 30, 31]. Choline has been demonstrated to be important in human brain development with the young pig model showing deficiency in prenatal choline leading to brain developmental defects [7]. Choline deficient animals showed reduced gray matter formation in the prefrontal cortex, which is associated with both the EX network and DMN. These findings, along with the similar developmental patterning between the pig and humans, makes the pig an excellent model for studying other key nutritional components, such as those for pregnant women, infant formula, and baby food.

In this Chapter, the effects of TBI on the VIS, EX, SM, and CERE networks are discussed in the main text, and this study's difficulties in detecting the DMN are discussed in Appendix C. However, in Chapter 5 [9], a sixth network, the auditory network, was detected in the pig brain. The auditory network was not examined in this work due to the inability to differentiate resting-state from task-based activations due to the constant noise caused by the MRI scanner, which acts as an un-controlled stimulus.

The work presented here does suffer from a few other limitations. One of which comes from the necessity to anesthetize the pigs during MRI scanning. The use of anesthesia is known to interfere with neural activity and neurovascular coupling [32, 33]. Use of a high dose of isoflurane specifically has recently been shown to reduce activation in sensory regions, including the primary and secondary somatosensory cortices and the motor cortex [34, 35]. No statistical differences were observed between the control and TBI groups for any of these anatomical regions in this study, so it is possible that the anesthesia protocol suppressed neural activity in these anatomical regions. Other anatomical regions may also have been affected by the anesthesia protocol, and certain pigs may respond differently to the anesthesia than others due to biological factors.

Although the effects of anesthesia must be considered and a protocol to minimize these effects must be sought, the biggest limitation of this work is the small group sizes ($n=3$ and $n=5$ for the control and TBI groups, respectively). Since this work was a preliminary study, the goal was to test the feasibility of detecting disruptions in functional networks caused by TBI using rs-fMRI. Despite the small group sizes, a significant difference ($p<0.05$) in the VIS and EX networks between the control and TBI groups were observed, as well as in four individual anatomical regions (the primary visual, dorsolateral prefrontal, anterior prefrontal, and premotor cortices). The SM and CERE networks, as well as many other individual anatomical regions, were also observed to be trending towards significant difference ($p<0.4$), and as group sizes increase, these trends may achieve significant difference ($p<0.05$). Nevertheless, this work demonstrates the feasibility of detecting the functional connectivity disruptions caused by TBI using a translational pig model.

References

1. Kinder, H.A., E.W. Baker, and F.D. West, *The pig as a preclinical traumatic brain injury model: current models, functional outcome measures, and translational detection strategies.* Neural regeneration research, 2019. **14**(3): p. 413.
2. Baker, E.W., et al., *Controlled cortical impact severity results in graded cellular, tissue, and functional responses in a piglet traumatic brain injury model.* Journal of neurotrauma, 2019. **36**(1): p. 61-73.
3. Jaber, S.M., S. Sullivan, and S.S. Margulies, *Noninvasive Metrics for Identification of Brain Injury Deficits in Piglets.* Developmental Neuropsychology, 2015. **40**(1): p. 34-39.
4. Sullivan, S., et al., *Improved behavior, motor, and cognition assessments in neonatal piglets.* Journal of neurotrauma, 2013. **30**(20): p. 1770-1779.
5. Platt, S.R., et al., *Development and characterization of a Yucatan miniature biomedical pig permanent middle cerebral artery occlusion stroke model.* Experimental & translational stroke medicine, 2014. **6**(1): p. 5.
6. Tanaka, Y., et al., *Experimental model of lacunar infarction in the gyrencephalic brain of the miniature pig: neurological assessment and histological, immunohistochemical, and physiological evaluation of dynamic corticospinal tract deformation.* Stroke, 2008. **39**(1): p. 205-212.
7. Mudd, A.T., C.M. Getty, and R.N. Dilger, *Maternal dietary choline status influences brain gray and white matter development in young pigs.* Current developments in nutrition, 2018. **2**(6): p. nzy015.
8. Olson, E., et al., *Alterations in daytime and nighttime activity in piglets after focal and diffuse brain injury*. Journal of neurotrauma, 2016. **33**(8): p. 734-740.
9. Simchick, G., et al., *Pig Brains Have Homologous Resting State Networks with Human Brains.* Brain connectivity, 2019(ja).
10. Ustinova, K.I., et al., *Physical therapy for correcting postural and coordination deficits in patients with mild-to-moderate traumatic brain injury.* Physiotherapy theory and practice, 2015. **31**(1): p. 1-7.
11. Iandolo, R., et al., *Neural correlates of lower limbs proprioception: An fMRI study of foot position matching.* Human brain mapping, 2018. **39**(5): p. 1929-1944.

12. Mar, A.C., et al., *The touchscreen operant platform for assessing executive function in rats and mice.* Nature protocols, 2013. **8**(10): p. 1985.
13. Izquierdo, A., et al., *The neural basis of reversal learning: an updated perspective.* Neuroscience, 2017. **345**: p. 12-26.
14. Sullivan, S., et al., *Behavioral deficits and axonal injury persistence after rotational head injury are direction dependent.* Journal of neurotrauma, 2013. **30**(7): p. 538-545.
15. Etkin, A. and T.D. Wager, *Functional neuroimaging of anxiety: a meta-analysis of emotional processing in PTSD, social anxiety disorder, and specific phobia.* American Journal of Psychiatry, 2007. **164**(10): p. 1476-1488.
16. Larson-Prior, L.J., et al., *Modulation of the brain's functional network architecture in the transition from wake to sleep*, in *Progress in brain research*. 2011, Elsevier. p. 277-294.
17. Mattsson, J., et al., *Maturation of the visual evoked response in newborn miniature pigs.* American journal of veterinary research, 1978. **39**(8): p. 1279-1281.
18. Fang, M., et al., *fMRI mapping of cortical centers following visual stimulation in postnatal pigs of different ages.* Life sciences, 2006. **78**(11): p. 1197-1201.
19. Li, Z.-Y., et al., *Rhodopsin transgenic pigs as a model for human retinitis pigmentosa.* Investigative ophthalmology & visual science, 1998. **39**(5): p. 808-819.
20. Kinder, H.A., et al., *Traumatic Brain Injury Results in Dynamic Brain Structure Changes Leading to Acute and Chronic Motor Function Deficits in a Pediatric Piglet Model.* Journal of neurotrauma, 2019(ja).
21. Baker, E.W., et al., *Scaled traumatic brain injury results in unique metabolomic signatures between gray matter, white matter, and serum in a piglet model.* PloS one, 2018. **13**(10).
22. Ashburner, J., et al., *SPM12 manual.* URL: http://www. fil. ion. ucl. ac. uk/spm/doc/spm12 manual. pdf, 2016.
23. Mairal, J., et al., *Online learning for matrix factorization and sparse coding.* Journal of Machine Learning Research, 2010. **11**(Jan): p. 19-60.
24. Palacios, E.M., et al., *Resting-state functional connectivity alterations associated with six-month outcomes in mild traumatic brain injury.* Journal of neurotrauma, 2017. **34**(8): p. 1546-1557.
25. Saikali, S., et al., *A three-dimensional digital segmented and deformable brain atlas of the domestic pig.* Journal of neuroscience methods, 2010. **192**(1): p. 102-109.
26. Baker, E.W., et al., *Induced pluripotent stem cell-derived neural stem cell therapy enhances recovery in an ischemic stroke pig model.* Scientific reports, 2017. **7**(1): p. 1-15.
27. Duberstein, K.J., et al., *Gait analysis in a pre-and post-ischemic stroke biomedical pig model.* Physiology & behavior, 2014. **125**: p. 8-16.
28. Webb, R.L., et al., *Human neural stem cell extracellular vesicles improve recovery in a porcine model of ischemic stroke.* Stroke, 2018. **49**(5): p. 1248-1256.
29. Gawryluk, J.R., et al., *Investigation of fMRI activation in the internal capsule.* BMC neuroscience, 2011. **12**(1): p. 56.
30. Mudd, A.T., et al., *Early-life iron deficiency reduces brain iron content and alters brain tissue composition despite iron repletion: A neuroimaging assessment.* Nutrients, 2018. **10**(2): p. 135.

31. Mudd, A.T., et al., *Dietary sialyllactose influences sialic acid concentrations in the prefrontal cortex and magnetic resonance imaging measures in corpus callosum of young pigs.* Nutrients, 2017. **9**(12): p. 1297.
32. Hamilton, C., Y. Ma, and N. Zhang, *Global reduction of information exchange during anesthetic-induced unconsciousness.* Brain Structure and Function, 2017. **222**(7): p. 3205-3216.
33. Liang, Z., J. King, and N. Zhang, *Intrinsic Organization of the Anesthetized Brain.* The Journal of Neuroscience, 2012. **32**(30): p. 10183-10191.
34. Kawaguchi, N., et al., *Effects of Isoflurane on Brain Functional Connectivity in Common Marmosets.* In Proceedings of the 27th Annual Meeting of ISMRM, Montreal, Canada, 2019.
35. Yin, T., R. Gruetter, and I.O. Jelescu, *Altered bilateral functional connectivity in rat brain under isoflurane and medetomidine anesthesia.* In Proceedings of the 27th Annual Meeting of ISMRM, Montreal, Canada, 2019.

Table 6.1

Networks and Anatomical Regions	Individual			Group Dual Regression		
	Sig	Pearson	Mean Ratio	Sig	Pearson	Mean Ratio
Visual	*	0.004*	0.015*	*	0.010*	0.036*
Primary Visual Cortex	$^{\#}$	0.013*	0.088$^{\#}$	*	0.007*	0.004*
Secondary Visual Cortex	*	0.006*	0.009*	-	0.904	0.982
Associative Visual Cortex	-	0.900	0.453	$^{\#}$	0.253$^{\#}$	0.263$^{\#}$
Executive Control	*	0.013*	0.015*	$^{\#}$	0.072$^{\#}$	0.039*
Primary Somatosensory Cortex	-	0.513	0.088$^{\#}$	-	0.875	0.530
Dorsolateral Prefrontal Cortex	$^{\#}$	0.348$^{\#}$	0.048*	$^{\#}$	0.094$^{\#}$	0.069$^{\#}$
Anterior Prefrontal Cortex	$^{\#}$	0.287$^{\#}$	0.164$^{\#}$	*	0.025*	0.042*
Orbitofrontal Cortex	-	0.928	0.582	-	0.526	0.233$^{\#}$
Insular Cortex	$^{\#}$	0.216$^{\#}$	0.062$^{\#}$	-	0.835	0.924
Ventral Anterior Cingulate Cortex	-	0.612	0.333$^{\#}$	-	0.351$^{\#}$	0.609
Dorsal Anterior Cingulate Cortex	-	0.744	0.067$^{\#}$	-	0.543	0.073$^{\#}$
Sensorimotor	-	0.921	0.317$^{\#}$	$^{\#}$	0.078$^{\#}$	0.103$^{\#}$
Primary Motor Cortex	-	0.522	0.308$^{\#}$	-	0.928	0.609
Somatosensory Associative Cortex	-	0.177$^{\#}$	0.567	-	0.425	0.078$^{\#}$
Premotor Cortex	$^{\#}$	0.055$^{\#}$	0.013*	$^{\#}$	0.174$^{\#}$	0.164$^{\#}$
Cerebellar	$^{\#}$	0.037*	0.222$^{\#}$	-	0.608	0.927

P-values comparing the Pearson spatial correlation coefficients and mean ratios of the control group and the TBI group for each network and each individual anatomical region. The groups were considered significantly different if $p<0.05$ (denoted by *), and they were considered to be trending towards significant difference if $p<0.4$ (denoted by #). A network or anatomical region was only considered significantly different or trending towards significant difference if the p-values for both the Pearson values and mean ratios were below the specified thresholds (‘Sig’ columns).

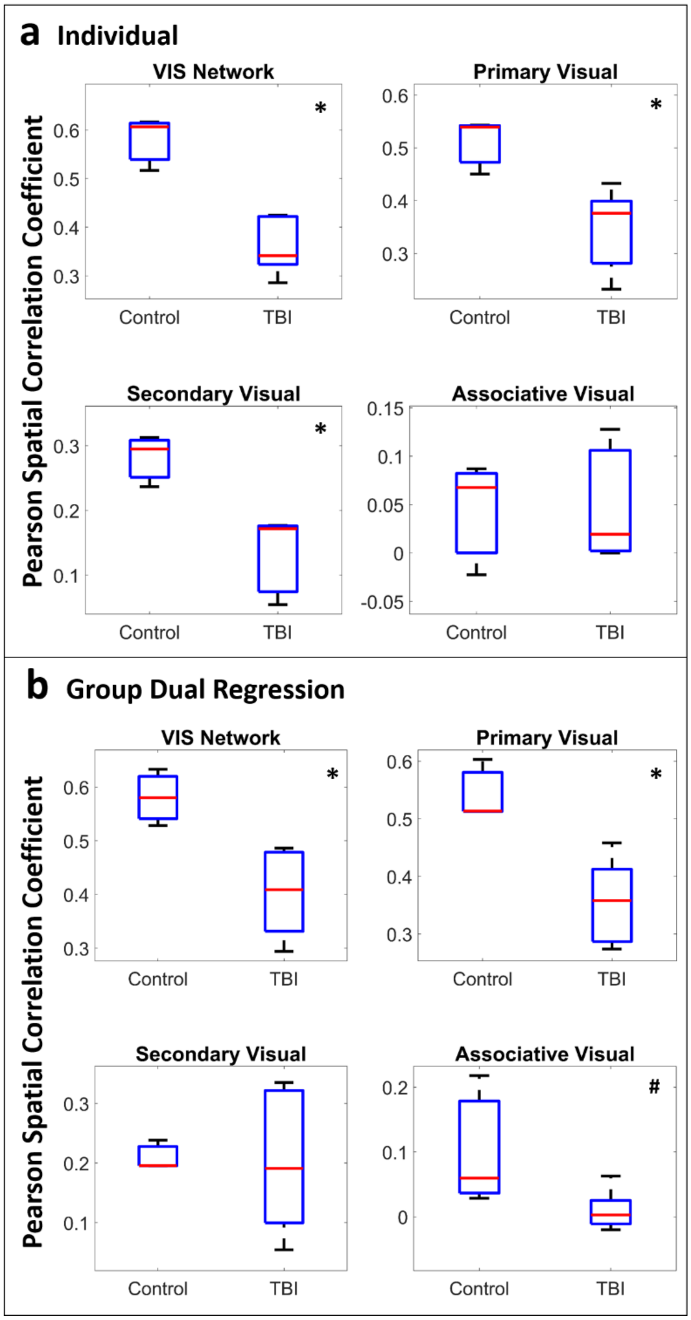

Figure 6.1: Boxplots of Pearson spatial correlation coefficients the visual (VIS) network and its individual anatomical regions obtained using individual analysis (a) and group dual regression analysis (b). An asterisk (*) in the upper right-hand corner indicates significant differences ($p<0.05$) between the control group and TBI group, and a number sign (#) indicates the groups are trending towards significant differences ($p<0.4$).

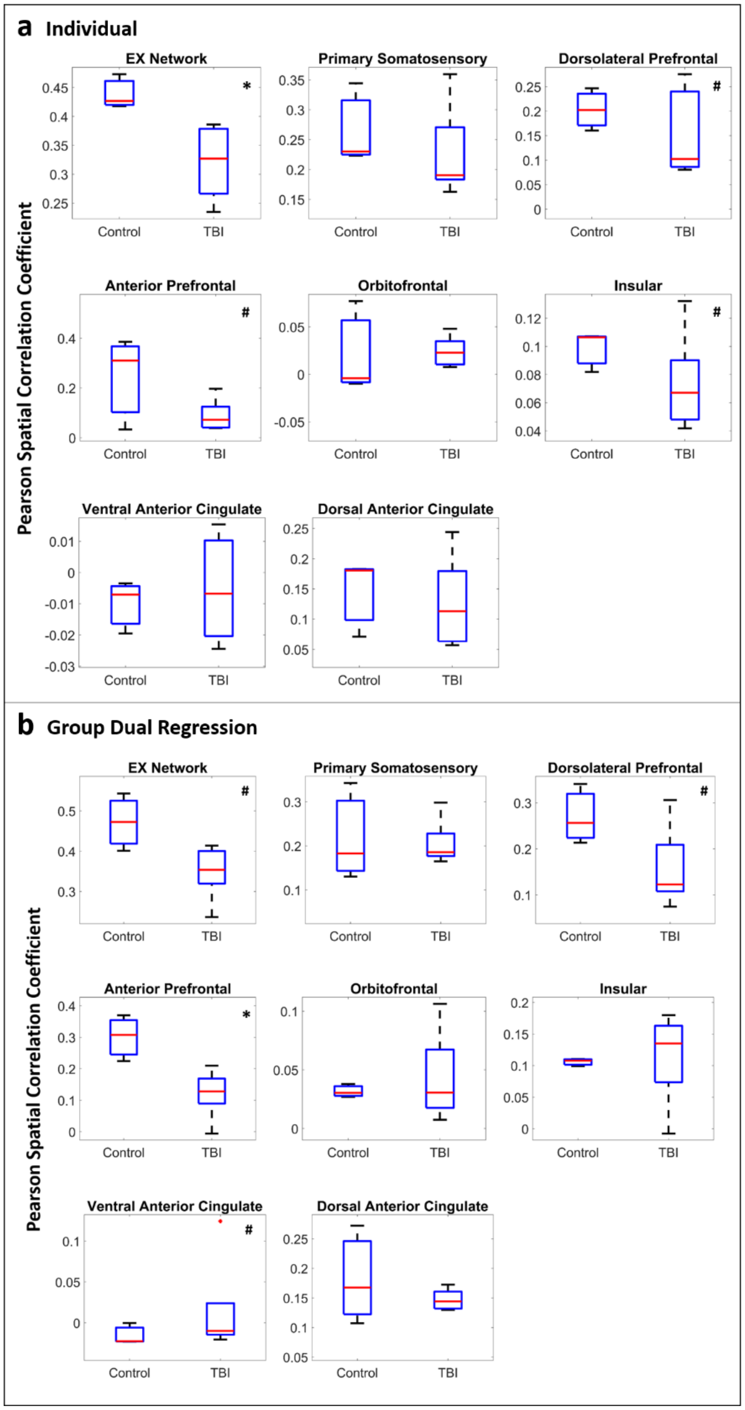

Figure 6.2: Boxplots of Pearson spatial correlation coefficients for the executive control (EX) network and its individual anatomical regions obtained using individual analysis (a) and group dual regression analysis (b). An asterisk (*) in the upper right-hand corner indicates significant differences (p<0.05) between the control group and TBI group, and a number sign (#) indicates the groups are trending towards significant differences (p<0.4).

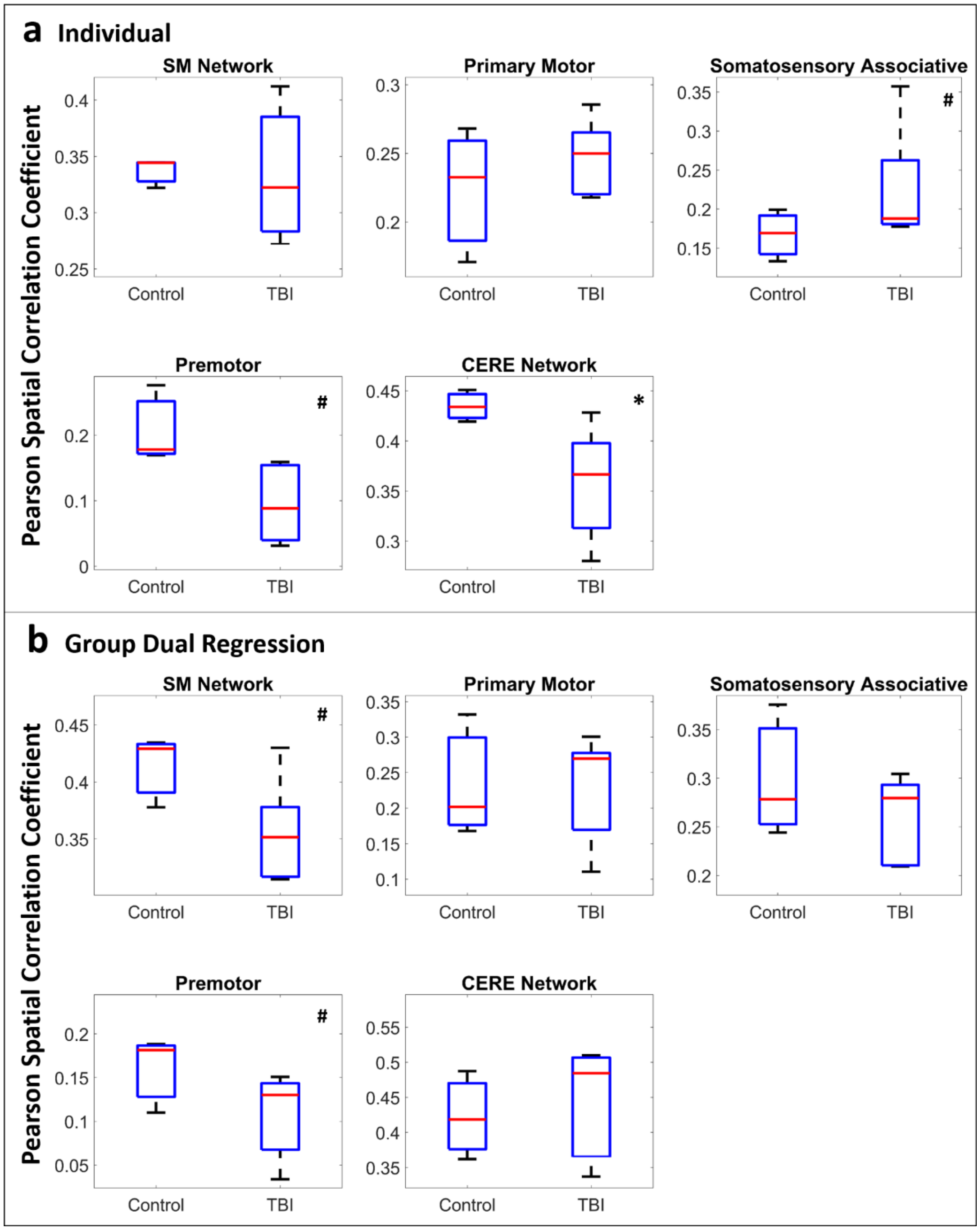

Figure 6.3: Boxplots of Pearson spatial correlation coefficients for the sensorimotor (SM) network and its individual anatomical regions, as well as the cerebellar (CERE) network, obtained using individual analysis (a) and group dual regression analysis (b). An asterisk (*) in the upper right-hand corner indicates significant differences ($p<0.05$) between the control group and TBI group, and a number sign (#) indicates the groups are trending towards significant differences ($p<0.4$).

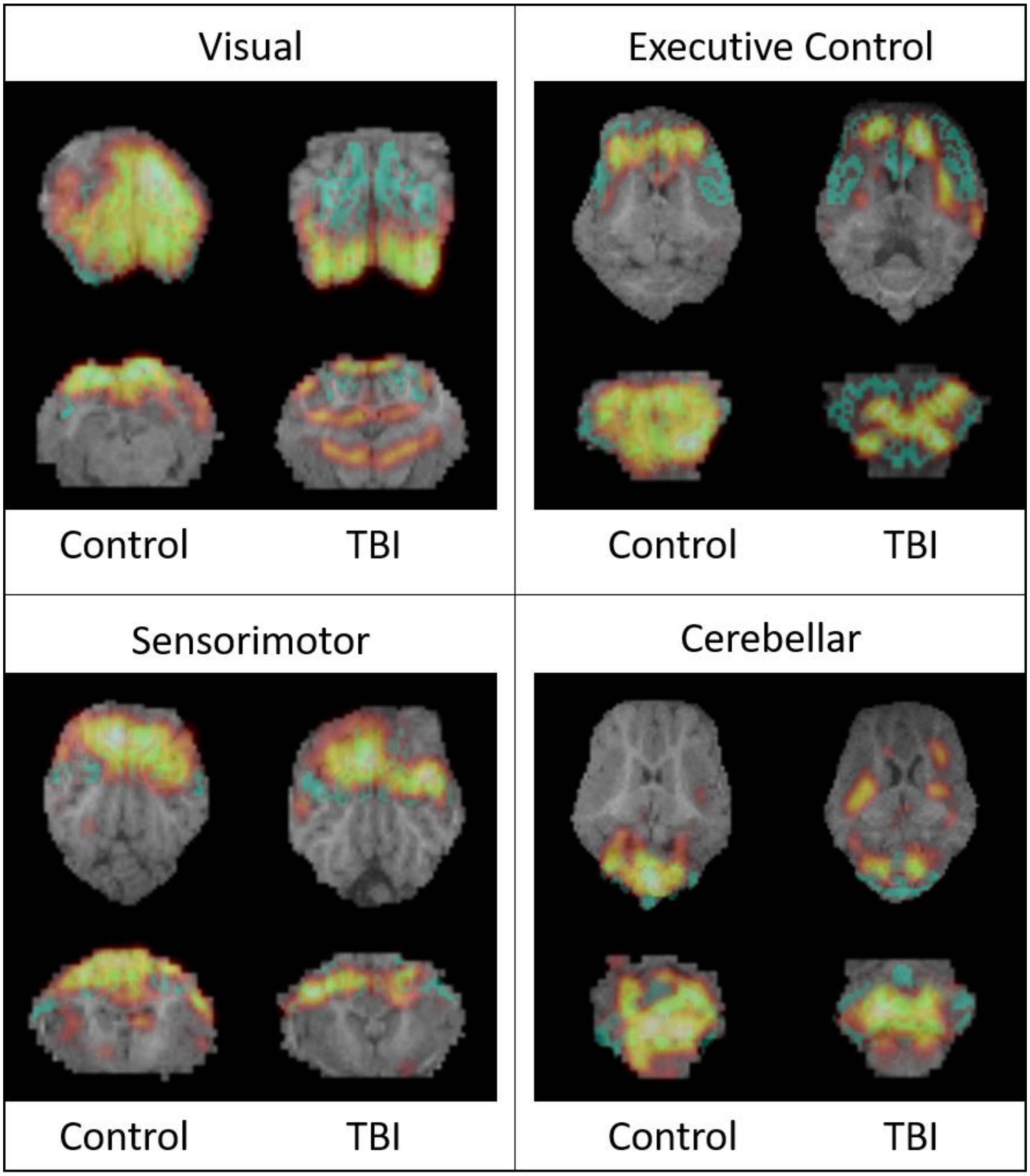

Figure 6.4: Two-dimensional representative images (top: axial plane, bottom: coronal plane) of activation maps (red-yellow) for the visual, executive control, sensorimotor, and cerebellar networks and their corresponding reference atlas (green) overlaid on each pigs' T1-weighted anatomical image. TBI pigs show noisier, less uniform activations in comparison to the control pigs, which is supported quantitatively by the three-dimensional Pearson spatial correlation coefficients and mean ratios (Figures 6.1-6.3 and C3-5).

CHAPTER 7

CONCLUSION

As shown throughout this dissertation, magnetic resonance imaging (MRI) has a wide-range of practical, quantitative capabilities, ranging from the quantification of physical and chemical properties of tissues, such as magnetic susceptibility and triglyceride composition, to the characterization of neural networks and nerve fibers in the brain.

Part 1: Quantification using Chemical Shift Encoded Magnetic Resonance Imaging

Chemical shift encoded (CSE-) MRI is one particularly useful technique that allows one to obtain information about multiple different chemical and physical properties of tissues, such as triglyceride composition, the effective translational spin-spin relaxation rate (R_2^*), and magnetic susceptibility. The ability to accurately determine triglyceride composition, including the number of double bonds per molecule (*ndb*), the number of methylene-interrupted double bonds per molecule (*nmidb*), the fatty acid chain length (*cl*), and the proton density fat fraction (*PDFF*), using chemical shift encoded (CSE-) MRI at a high magnetic field strength of 7T is demonstrated in Chapter 2. In addition, the feasibility of determining small changes in liver iron concentration (LIC) using magnetic susceptibility quantification at a high magnetic field (e.g. 7T) is demonstrated in Chapter 3.

Although the use of high magnetic fields in MRI can be beneficial, as it often allows for higher image resolution and/or better signal-to-noise ratios (SNR), CSE-MRI encounters many disadvantages at higher fields, which make quantification more challenging. Specifically for triglyceride composition quantification, the spins associated with the protons of the different chemical species that make up fatty tissues dephase more quickly after excitation at higher fields leading to faster signal decay and lower SNR. When using methods where an *a priori* spectral model is needed in order to perform this quantification, as discussed in Chapter 2, a more accurate model (e.g. a 9-peak model opposed to a reduced 6-peak model) may be necessary at higher fields, as MR spectral profile broadening decreases and chemical species with similar chemical shifts become more distinguishable from each other. LIC quantification using CSE-MRI also faces challenges at higher magnetic fields. As discussed for triglyceride composition quantification, similar problems related to fatty tissue in the liver arise, and additionally, the magnetic field inhomogeneities due to the perturbations caused by iron leads to faster signal decay and lower SNR.

Therefore, in human studies, it is becoming increasingly popular to study diseases and disorders associated with high or changing fat content and/or liver iron overload at lower field strengths (e.g. 1.5T). However, for pre-clinical, small animal studies, like those discussed in Chapters 2 and 3, higher resolution is necessary, especially in cases where spatial information is important. Despite the challenges that arise in CSE-MRI at higher fields, the work discussed in Chapters 2 and 3 are able to overcome these challenges and draw useful conclusions that can be translated to human studies.

CSE-MRI is primarily used to study non-alcoholic fatty liver disease and liver iron overload, leading to the publication of several human liver fat spectral models. Chapter 2 demonstrates that a material specific model, opposed to a generic human liver model, is necessary to accurately quantify triglyceride composition (*ndb*, *nmidb*, and *cl*) when using estimation methods that assume the spectral model to be known as *a priori* information. Although, the *PDFF* is shown to be independent of the chosen spectral model. This chapter also demonstrates the feasibility of accurately quantifying the spatial distribution of the triglyceride composition, which is important in monitoring activations of brown adipose tissues, beiging of white adipose tissues, and various obesity-related diseases and disorders. This spatial quantification is a benefit of CSE-MRI that magnetic resonance spectroscopy (MRS) lacks, as MRS only provides an averaged triglyceride composition estimation within a localized volume of interest.

Chapter 3 demonstrates that susceptibility quantification using quantitative susceptibility mapping (QSM) may be more robust than the quantification of R_2^* for measuring LIC. However, in this chapter, only an ex vivo mouse model was used. For in vivo applications, QSM may be more sensitive to additional factors, such as blood flow, oxygenation content, and respiratory motion, than R_2^* quantification. Unlike R_2^* though, magnetic susceptibility benefits from being an intrinsic physical property of the tissue that is independent of the magnetic field strength.

Although the feasibility of quantifying LIC in Chapter 3 is demonstrated using a high field strength of 7T, a susceptibility-to-LIC conversion factor of 0.829 ppm/(mg/g wet) is presented, which agrees with previously published QSM derived results obtained at lower field strengths (e.g. 1.5T and 3T). However, all QSM derived conversion factors discussed tend to underestimate the theoretical susceptibility values expected from the iron storage complexes typically found in the human and murine body, hemosiderin and ferritin (1.1-1.6 ppm/(mg/g wet)). Recent work focusing on differentiating Fe^{2+} from Fe^{3+} [1, 2] may provide helpful insight into determining the concentrations of these two iron storage complexes and determining a more accurate theoretical susceptibility value.

Part 2: Studying Pig Brain Functional Connectivity using Magnetic Resonance Imaging

Many neurological injuries, diseases, and developmental influences in humans lead to disruptions or changes in brain functional connectivity. Therefore, the study of functional connectivity and its disruptions may provide useful information to help develop treatments and therapies to restore or improve damaged areas. Functional (f) MRI, which is the most commonly used technique for studying functional connectivity, is a non-invasive medical imaging technique that allows for the mapping of brain functional connectivity by measuring changes in the oxygenation of brain tissue caused by neural signaling.

Due to safety and ethical concerns, many treatments and therapies cannot be tested on human subjects. Therefore, animal surrogates are often used for pre-clinical research. Rodents and non-human primates have been the primary surrogates for studying the brain's functional connectivity. However, rodents have some significant differences in brain anatomy compared to the human brain, and the use of non-human primates is economically challenging. Due to the similar size, structure, composition, and neurodevelopment of the pig brain in comparison to the human brain, the pig serves as a useful large animal model for studying brain connectivity. Although much is known about the pig brain's structural connectivity, little work has been conducted studying the pig's functional connectivity.

Chapters 5 and 6 of this dissertation presented information that better helps understand the pig brain's functional connectivity and the disruptions that can be caused by traumatic brain injuries (TBIs). First, six resting-state networks (RSNs) that highly resemble those found in humans were detected using group functional connectivity analysis (Chapter 5), including the executive control (EX), cerebellar (CERE), visual (VIS), sensorimotor (SM), auditory (AUD), and default mode (DMN) networks. These networks were detected using two separate methods:

independent component analysis (ICA) and sparse dictionary learning (sDL). ICA is currently the most commonly used technique to extract signal components and their corresponding spatial activation maps from fMRI data; however, in this work sDL outperformed ICA when comparing the activation maps of each technique to a pig functional network reference atlas using Pearson spatial correlation coefficients and mean ratios. sDL differs from ICA in that it doesn’t assume the signal components to be independent from each other and that it enforces a sparse representation of the spatial activation maps.

Many RSNs in the human brain are well defined and characterized. However, to the best knowledge of the authors, this was the first study to attempt to characterize RSNs in the pig brain. Therefore, additional evidence of the validity of these networks was provided by performing diffusion tensor imaging (DTI) and measuring various structural connectivity quantities, since functional and structural connectivity have been shown to be positively correlated. DTI allows for the mapping of the white matter nerve tracts in the brain by tracking the diffusion of water molecules along structural pathways. For the RSNs detected in Chapter 5, higher measures of mean diffusivity, fractional anisotropy, nerve fiber length, and nerve fiber density were found for the fibers intersecting with the activated areas associated with these RSNs in comparison to the whole brain.

Although this study was performed with a small sample size (n=12), the establishment of these six RSNs provides a groundwork for the development of a standard pig brain functional network atlas, which can be used to support future translational pig model studies characterizing functional network disruption caused by disease and injury. However, the RSNs presented in this work should likely be better refined using a larger sample before its use as a “ground-truth”.

Chapter 6 seeks to detect and evaluate disruptions in the RSNs established in Chapter 5 using a translational TBI pig model. TBIs were experimentally induced in four-week-old pigs using a controlled cortical impactor, and rs-fMRI data was acquired one day post-TBI. Using two different methods to determine individual pig functional connectivity (individual analysis and group dual regression analysis), disruptions in four of the RSNs (VIS, EX, SM, and CERE) were detected, as shown by reduced Pearson spatial correlation coefficients and mean ratios of a TBI group in comparison to a healthy control group. These disruptions were then successfully traced back to affected individual anatomical regions, with both methods showing a high level of consistency and detecting disruptions in four of the same sub-cortical anatomies.

Results related to the AUD network were not examined in this Chapter due to the inability to differentiate resting-state (rs-) from task-based (tb-) activations due to the constant noise caused by the MRI scanner, which acts as an un-controlled stimulus. However, decreasing trends for this network, including decreasing trends for the auditory cortex and superior temporal gyrus, were observed. Only rs-fMRI was used in this study; however, this trend suggests that it may be possible to detect functional connectivity disruptions or changes caused by TBI, as well as other neural injuries, diseases, and developmental influences, using tb-fMRI.

The AUD and VIS networks have been shown to have the capability of being activated even when the subject is anesthetized [3, 4], enabling the detection of blood oxygen level dependent (BOLD) responses in the fMRI signal and identification of activated regions. Fang et al. [4] has demonstrated the feasibility of detecting changes in the visual cortex in awake, restrained pigs aged from two to six months old by studying functional changes over time using tb-fMRI.

The EX network, which is known to be associated with the sense of touch and with pain [5], and the SM network may also be examined using tb-fMRI and a tactile stimulus. In human studies, it has been shown that pain evokes three responses in the brain: sensory-discriminative, affective-motivational, and cognitive-evaluative [6-8]. The sensory component detects and processes painful stimuli, the affective component is the emotional response to the pain, and the cognitive component is understanding what the pain is and how it affects you. Although anesthesia may suppress the response of a tactile stimulus, it is still possible to detect the BOLD response using fMRI [9, 10]. Therefore, auditory, visual and tactile tb-fMRI, along with rs-fMRI, may provide insight into the functional connectivity disruptions or changes caused by neural injuries, diseases, and developmental influences.

References

1. Dietrich, O., et al., *MR imaging differentiation of Fe 2+ and Fe 3+ based on relaxation and magnetic susceptibility properties.* Neuroradiology, 2017. **59**(4): p. 403-409.
2. Dietrich, O., et al. *Differentiation of Fe2+ and Fe3+ with iron-sensitive MRI*. in *Proc Intl Soc Mag Reson Med*. 2013.
3. Yin, T., R. Gruetter, and I.O. Jelescu, *Altered bilateral functional connectivity in rat brain under isoflurane and medetomidine anesthesia.* In Proceedings of the 27th Annual Meeting of ISMRM, Montreal, Canada, 2019.
4. Fang, M., et al., *fMRI mapping of cortical centers following visual stimulation in postnatal pigs of different ages.* Life sciences, 2006. **78**(11): p. 1197-1201.
5. Smith, S.M., et al., *Correspondence of the brain's functional architecture during activation and rest.* Proceedings of the National Academy of Sciences, 2009. **106**(31): p. 13040-13045.
6. Ison, S.H., et al., *A review of pain assessment in pigs.* Frontiers in veterinary science, 2016. **3**: p. 108.
7. Melzack, R. and K.L. Casey, *Sensory, motivational, and central control determinants of pain: a new conceptual model.* The skin senses, 1968. **1**: p. 423-43.
8. Flor, H. and M.C. Bushnell, *Central imaging of pain.* The Neurobiology of Pain:(molecular and Cellular Neurobiology), 2005: p. 311.
9. Antognini, J.F., et al., *Isoflurane anesthesia blunts cerebral responses to noxious and innocuous stimuli: a fMRI study.* Life sciences, 1997. **61**(24): p. PL349-PL354.
10. Shirai, T., et al., *Pharmacologic Modulation of Noxious Stimulus-evoked Brain Activation in Cynomolgus Macaques Observed with Functional Neuroimaging.* Journal of the American Association for Laboratory Animal Science, 2019.

APPENDIX A

SUPPLEMENTARY MATERIAL – CHAPTER 2

Monte Carlo simulations to determine optimal MRI echo times.

Purpose

To determine optimal echo times (initial echo time TE_i and echo spacing ΔTE) for reducing the biases and variations in the estimations of triglyceride composition (*ndb*, *nmidb*, and *cl*) and *PDFF* arising due to inaccuracies in the relative amplitudes of the 9-peak fat spectral model.

Methods

Optimal echo times were determined using Monte Carlo simulations, in which theoretical MR signals were generated using the following rewritten form of Eq. (2.2)

$$s(t_n) = C_{\mathrm{sys}}[(1 - PDFF) + PDFF \sum_{m=1}^{M} \alpha_m e^{i2\pi f_m t_n}] e^{i2\pi f_B t_n} e^{-R_2^* t_n} \qquad \text{(A1)}$$

where $C_{\mathrm{sys}} = \rho_W + \rho_F$ is a constant associated with each particular MR system.

The 9-peak fat spectral model (Table 2.1) was used in generating the theoretical signals. The chemical shifts of the 9 fat peaks were fixed, but the relative amplitudes of the peaks varied across iterations. At every iteration, the relative amplitudes for the signal model were generated using the theoretical peak amplitudes (Table 2.1) and randomly selected values of *ndb*, *nmidb*, and *cl* from ranges that were deemed to be biologically plausible [1] (Table A1, left column). Each biologically plausible range was divided into one-hundred discrete values for random selection. When solving for triglyceride composition (*ndb*, *nmidb*, and *cl*) and *PDFF*, a 9-peak liver model (model 9 in Table 2.2) [2] was used, resulting in inaccuracies in the relative amplitudes of the fat spectral model. R_2^*, the decomposition parameters ($\rho_\mathrm{W}, \rho_\mathrm{F}$, *ndb, nmidb,* and *cl*), and *PDFF* were all estimated from the theoretical signal at every iteration using the CSE-MRI post-processing methods described in the main text.

All theoretical signals were generated using a B_o of 7T, twelve echoes, and a representative R_2^* of 40 s^{-1}. No noise was added to ensure biases would only arise due to the inaccuracies in the spectral model, and f_B was fixed at zero and not estimated to ensure that inaccuracies in the spectral model would not be associated with static field inhomogeneity.

Simulations were performed for a range of 0.1-3 ms for $\mathrm{TE_i}$ in 0.1 ms increments, a range of 0.05-1 ms in 0.05 ms increments for ΔTE, and representative *PDFF* values of low- (5%), medium- (65%), and high-level (95%), which are representative of typical values found in the liver, brown adipose tissue, and white adipose tissue, respectively.

A total of 1024 iterations were performed for each combination of $\mathrm{TE_i}$, ΔTE, and *PDFF*. The biases in the estimations were evaluated using the magnitude of the average difference between the estimated parameters and their true values, and the variations were evaluated using the standard deviations of the estimated parameters across iterations.

Results and Discussion

Heat maps of the biases and variations in the estimates of *ndb, nmidb, cl,* and *PDFF* are displayed in Figures A1-2. To better understand the dependency of the biases and variations on echo spacing, regardless of B_0, ΔTE is displayed as the phase difference between the water peak and the main fat peak (-3.40 ppm relative to water), i.e., $\Delta\varphi = 2\pi \cdot f \cdot \Delta TE$, where $f = \gamma B_0 \cdot 3.4 \times 10^{-6}$ with γ being the proton gyromagnetic ratio.

Figure A1 presents the biases in the estimates, and it is observed that ΔTEs in the range of approximately 1.0-1.4 π radians and $\mathrm{TE_i}$ values in the range of approximately 0.4-1.5 ms are optimal (area covered by red ovals) for minimizing the biases across all parameters and for all examined *PDFF*s. Although the biases depend more strongly on *Δ*TE, some TE_i dependence is observed within the optimal *Δ*TE range, as well as a slight dependence on the true *PDFF*.

Similar patterns observed in the biases are also observed in the variations of the estimates. The variations are also minimized for the same *Δ*TE range as the biases (Figure A2). However, unlike the biases, the variations are relatively independent of TE_i within this optimal *Δ*TE range, except for the *PDFF* estimate for a true *PDFF* of 65% (Figure A2h). The variations in *ndb, nmidb*, and *cl* are also relatively independent of the true *PDFF*, and the variations in the estimates of *PDFF* are larger for moderate true *PDFF*s (65%, Figure A2h) and minimal at extremely low and high true *PDFF*s (5% and 95%, Figure A2d,l). However, for all combinations of true *PDFF* and echo times, the bias and variability in the estimation of *PDFF* is always comparatively small in relation to the true value. The bias and variability is almost always less than 1%.

Very short *Δ*TEs and *Δ*TEs leading to phase differences approaching 2π between the water resonance peak and the main fat resonance peak tend to result in larger biases and variations in all estimates (Figures A1-2). Only *Δ*TEs of less than 1.0 ms (approximately 2π at 7T) were examined in this work to avoid possible artifactual solutions that may arise in the field map estimation due to the periodicity (1/*Δ*TE) of the solution [3].

Although this study examines the biases and variations caused by inaccuracies in the relative amplitudes of the fat spectral model, optimal *Δ*TEs for maximizing parameter SNR and reducing the variance in the estimates arising due to noise have previously been reported [4, 5]. Berglund *et al.* [4] defined a range of approximately 0.43-1.52 π radians to be optimal, while Peterson *et al.* [5] defined an optimal range of approximately 0.87-1.74 π radians. These ranges for *Δ*TE are larger than the optimal range of 1.0-1.4 π radians defined in this work. However, neither of these studies examined the influence of TE_i on the estimates. Berglund *et al.* set TE_i to be equal to *Δ*TE, while Peterson *et al.* used a fixed TE_i of 1.3 ms. These studies were also performed at lower field strengths (1.5T and 3T) and used differing R_2^* values ($20s^{-1}$ and $50s^{-1}$) and numbers of echoes (32 for Berglund *et al.* and 8 for Peterson *et al.*, respectively). All of which may influence the estimates [6].

The biologically plausible triglyceride parameter ranges used in generating the theoretical signals, which was defined by Hong *et al.* [1], may underestimate true biological variability, as Hamilton *et al.* [7] has reported values outside of these ranges for white adipose tissue (*ndb* = 3.3 and *nmidb* = 1.0). Simulations using larger ranges were conducted, which affected the absolute values of the biases and variations. However, the results of these simulations showed nearly identical patterns to those observed in Figures A1-2, and therefore, are not presented here.

The biases generated in the estimations of the triglyceride parameters and *PDFF* by the above methodology arise due to error propagation coming from the R_2^* estimate. In the phantom and in vivo experiments in the main text, errors or biases arising in the estimation of the field map using the graphcut method are also expected to influence the triglyceride parameter and *PDFF* estimations due to error propagation. The effects of field map error propagation were examined by introducing a constant field map bias into the simulation; however, different patterns were observed for varying degrees of field map bias. Therefore, it is difficult to determine a single fixed range of optimal echo times since this adds another dependent variable or dimensionality to the optimization. The results presented here correspond to those observed with no or relatively small field map bias. Future work may include additional analysis to determine optimal echo times for reducing the bias in the field map estimate and comparing these results to those presented here.

References

1. Hong, C.W., et al., *MRI proton density fat fraction is robust across the biologically plausible range of triglyceride spectra in adults with nonalcoholic steatohepatitis.* Journal of Magnetic Resonance Imaging, 2018. **47**(4): p. 995-1002.
2. Hamilton, G., et al., *In vivo characterization of the liver fat (1)H MR spectrum.* NMR Biomed, 2011. **24**(7): p. 784-90.
3. Hernando, D., et al., *Robust water/fat separation in the presence of large field inhomogeneities using a graph cut algorithm.* Magn Reson Med, 2010. **63**(1): p. 79-90.
4. Berglund, J., H. Ahlstrom, and J. Kullberg, *Model-based mapping of fat unsaturation and chain length by chemical shift imaging--phantom validation and in vivo feasibility.* Magn Reson Med, 2012. **68**(6): p. 1815-27.
5. Peterson, P. and S. Mansson, *Simultaneous quantification of fat content and fatty acid composition using MR imaging.* Magn Reson Med, 2013. **69**(3): p. 688-97.
6. Hernando, D., J.H. Kramer, and S.B. Reeder, *Multipeak fat-corrected complex R2* relaxometry: theory, optimization, and clinical validation.* Magn Reson Med, 2013. **70**(5): p. 1319-31.
7. Hamilton, G., et al., *MR properties of brown and white adipose tissues.* J Magn Reson Imaging, 2011. **34**(2): p. 468-73.

Table A1

Biologically Plausible Ranges for the Triglyceride Parameters [1] and 9-Fat Peak Relative Amplitudes (%)

Triglyceride Parameters			**Water-Fat Chemical Shifts (ppm)**								
ndb	**nmidb**	**cl**	**-3.80**	**-3.40**	**-3.10**	**-2.68**	**-2.46**	**-1.95**	**-0.50**	**0.49**	**0.59**
[1.90, 2.7]	[0.30, 0.90]	[17.35, 17.55]	[8.70, 8.94]	[58.75, 65.55]	[5.80, 5.96]	[3.88, 9.50]	[5.80, 5.96]	[0.58, 1.79]	[3.86, 3.97]	[0.97, 0.99]	[3.67, 5.36]

Triglyceride parameter ranges that were deemed to be biologically plausible [1] and their corresponding biologically plausible 9-peak relative amplitudes (%) calculated from the theoretical peak amplitudes given in Table 2.1.

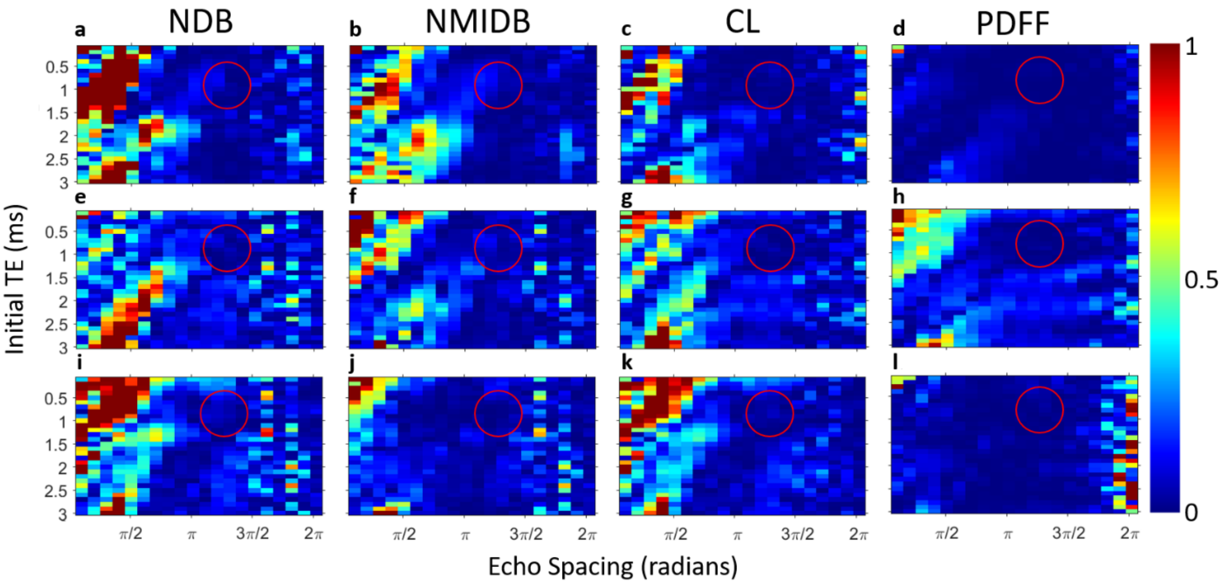

Figure A1: Monte Carlo results for representative *PDFF*s of 5% (first row, a-d), 65% (second row, e-h), and 95% (third row, i-l) displaying scaled average biases in the estimations of *ndb* (first column), *nmidb* (second column), *cl* (third column), and *PDFF* (fourth column) caused by inaccuracies in the relative amplitudes of the 9-peak fat spectral model and echo time selection. To minimize bias across all parameters and representative *PDFF*s, optimal echo spacings were determined to be approximately 1.0-1.4 π radians, and optimal TE_i values were determined to be approximately 0.4-1.5 ms (area covered by red ovals). Echo spacing is given in radians, which represents the phase difference between the water resonance peak and the main fat resonance peak located at -3.40 ppm. Each column was scaled between zero and one for comparison across parameters; therefore, values tending towards zero are associated with low bias and values tending towards one are associated with high bias in comparison to other values in the same column.

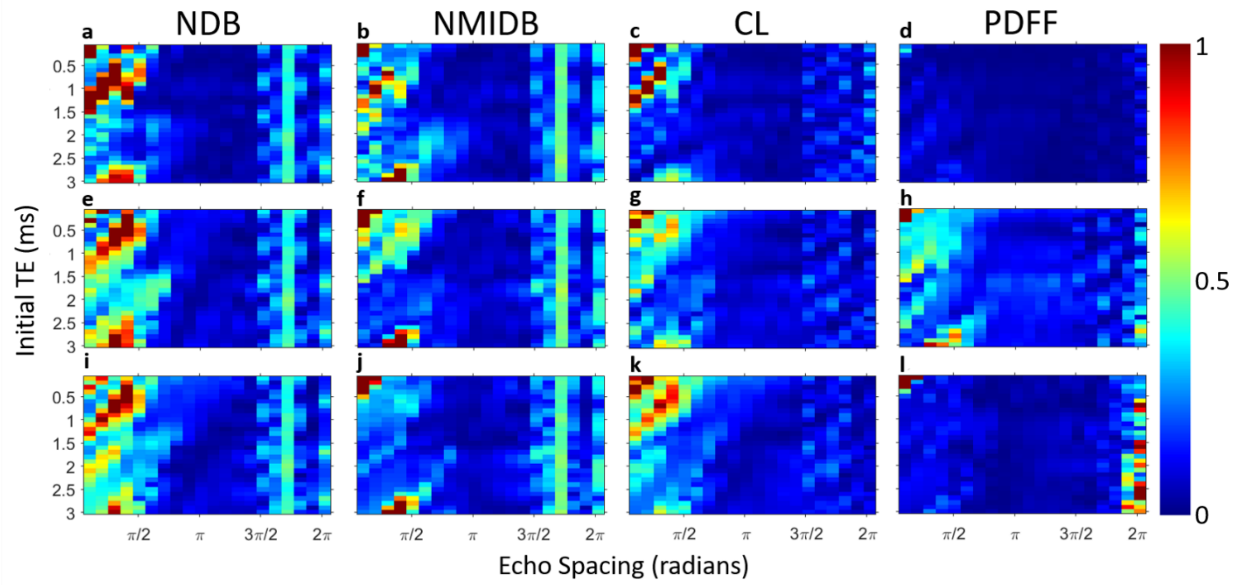

Figure A2: Monte Carlo results for representative *PDFF*s of 5% (first row, a-d), 65% (second row, e-h), and 95% (third row, i-l) displaying scaled standard deviations of the estimations of *ndb* (first column), *nmidb* (second column), *cl* (third column), and *PDFF* (fourth column) caused by inaccuracies in the relative amplitudes of the 9-peak fat spectral model and echo time selection. The optimal echo times determined for reducing the average bias in the estimations across all parameters (Figure A1) were also determined to be optimal for reducing the standard deviations of the estimations. Echo spacing is given in radians, which represents the phase difference between the water resonance peak and the main fat resonance peak located at -3.40 ppm. Each column was scaled between zero and one for comparison across parameters; therefore, values tending towards zero are associated with small standard deviations and values tending towards one are associated with large standard deviations in comparison to other values within the same column.

APPENDIX B

SUPPLEMENTARY MATERIAL – CHAPTER 5

Sparse Dictionary Learning Parameter Optimization

Sparse dictionary learning (sDL) was performed by minimizing Eq. (5.1) in the main text, which includes two free parameters: the number of atoms (n) and the sparsity parameter (λ). First, n was optimized using a fixed λ of 0.15, while n was varied between 10 and 400. Then for the optimally determined value of n, λ was optimized by varying its value between 0.001 and 1.0.

Optimization of the parameters was performed using the following procedure. For each variable parameter value, activation maps were generated, and the activation maps that produced the maximum Pearson spatial coefficients with each reference pig RSN atlas were determined. The Pearson values were then normalized (divided by the maximum) across the variable parameter and summed across the six RSNs. The parameter value that produced the maximum normalized Pearson sum was considered optimal.

Figure B1a and c show the normalized Pearson sum values and the normalized Pearson values for each individual RSN, respectively, as a function of n. The optimal value of n was determined to be 292 (Figure B1a), and for this value, all RSNs produce maximal or near maximal Pearson values (Figure B1c). When performing sDL, it is typical to use a complete or over-complete dictionary matrix, or in other words, n is generally equal to or greater than the length of the time series being decomposed. The overall length of the time series for the group dataset is 3592; however, since similar RSN fluctuations are expected across pigs, a complete dictionary matrix is considered as n=292, which is the length of the shortest time series associated with the pig whose last eight volumes were removed due to motion.

Figure B1b and d show the normalized Pearson sum values and the normalized Pearson values for each individual RSN, respectively, as a function of λ. The optimal value of λ was determined to be 0.15 (Figure B1b); although, a value of 0.5 performed almost equally as well. For λ=0.15, five of the six RSNs produce maximal or near maximal Pearson values, while the sensorimotor RSN produces a relatively low Pearson value (Figure B1d). This is also the case for λ=0.5, where only the auditory RSN is the lone RSN to produce a relatively low Pearson value. Since the normalized Pearson value, as well as the absolute Pearson value, of the sensorimotor RSN for λ=0.15 was greater than the values of the auditory RSN for λ=0.5, the optimal value for λ was still considered to be 0.15. By choosing the smaller λ value, the activation maps have less of a sparsity constraint.

RSN Individual Anatomy Analysis

Using the averaged sDL activation maps (RSNs), Pearson spatial coefficients and mean ratio values were determined for each anatomical component given in Table 5.1 for each RSN. The volumetric percentage of each anatomical component in relation to its corresponding RSN volume was also determined from the reference pig RSN atlas. The results of this analysis are given in Table B1. Individual anatomies (lobules, nuclei, and peduncles) of the cerebellum were not examined in this work.

When comparing anatomies of a similar RSN, a high Pearson correlation value and a high mean ratio indicates good correlation between the anatomy and RSN. However, a low Pearson value does not necessarily indicate a poor correlation between the anatomy and the RSN if the anatomy is small and the mean ratio is large. Only if both the Pearson and mean ratio values are small, then the anatomy is considered poorly correlated.

For the visual, sensorimotor, and auditory networks, all anatomies tend to correlate well with their corresponding RSN map, and for the executive control network, all anatomies tend to correlate well, except for the ventral anterior cingulate cortex (VACC-EX). In the default mode network, the anterior prefrontal (APC-DMN), orbitofrontal, and parahippocampal (PHC-DMN) cortices all produce poor correlations with the default mode RSN.

Further structural connectivity analysis of these poorly correlated anatomies was performed by measuring the mean diffusivity (*MD*), fractional anisotropy (*FA*), fiber length (*FL*), and fiber density (*FD*) of the fibers intersecting with each anatomical volume from the reference RSN atlas (Figure B2), as well as for the empirically determined activation volume from the averaged sDL maps that was found within each anatomical region. A ratio of the averages of these measurements (average from activation volume divided by average from reference atlas) was also determined (Figure B3). Further discussion of the poorly correlated anatomies and their structural connectivity measures are given in the main text (Chapter 5: Discussion).

Table B1: RSN Anatomy Statistics

RSN	Pearson	Mean Ratio	Percentage
Executive Control			
Primary Somatosensory Cortex	0.23	4.00	38.2
Dorsolateral Prefrontal Cortex	0.29	10.1	9.66
Anterior Prefrontal Cortex	0.30	8.91	13.2
Orbitofrontal Cortex	0.06	6.75	0.81
Insular Cortex	0.14	2.86	29.1
Ventral Anterior Cingulate Cortex	0.00	0.19	1.56
Dorsal Anterior Cingulate Cortex	0.25	9.63	7.52
Visual			
Primary Visual Cortex	0.42	6.72	56.8
Secondary Visual Cortex	0.30	5.85	36.8
Associative Visual Cortex	0.10	4.85	6.39
Sensorimotor			
Primary Motor Cortex	0.18	4.79	21.2
Somatosensory Associative Cortex	0.32	5.31	54.6
Premotor Cortex	0.15	3.71	24.2
Auditory			
Superior Temporal Gyrus	0.16	7.29	20.3
Auditory Cortex	0.40	8.87	79.7
Default Mode			
Hippocampus	0.20	5.75	12.7
Anterior Prefrontal Cortex	0.03	0.80	20.7
Orbitofrontal Cortex	0.00	0.00	1.28
Inferior Temporal Gyrus	0.11	3.03	15.1
Ventral Posterior Cingulate Cortex	0.07	9.19	0.53
Dorsal Posterior Cingulate Cortex	0.14	3.31	18.7
Retrosplenial Cingular Cortex	0.06	5.59	0.48
Anterior Entorhinal Cortex	0.13	4.45	9.33
Parahippocampal Cortex	0.05	1.14	21.2

Pearson spatial coefficients and mean ratio values calculated using the averaged sDL activation maps and each anatomical component, and the volumetric percentage of each anatomical component in relation to its corresponding RSN volume, as determined from the reference pig RSN atlas.

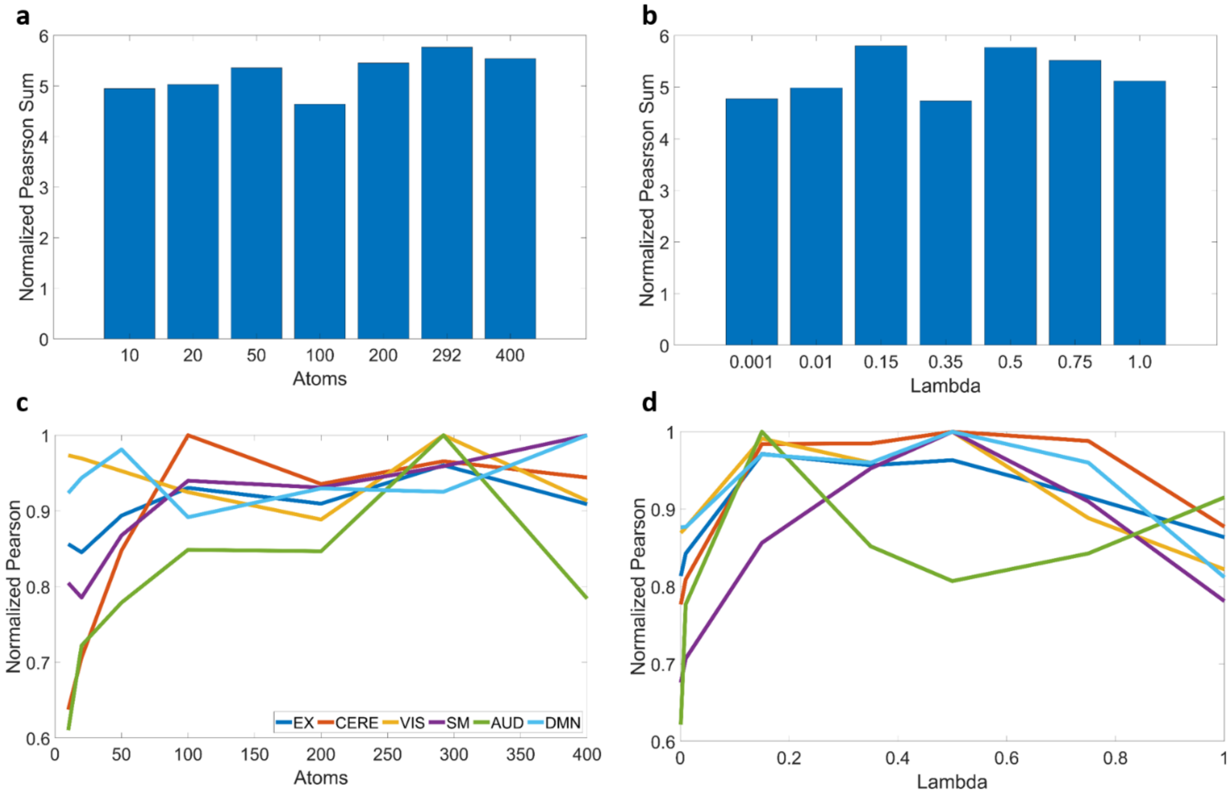

Figure B1: Normalized Pearson sum as a function of the number of atoms using a fixed sparsity parameter of 0.15 (a) and as a function of lambda using a fixed number of atoms of 292 (b). The number of atoms and lambda value that produced the maximum normalized Pearson sum was considered optimal, and these values were determined to be 292 and 0.15, respectively. Normalized Pearson values for each individual RSN are also given as a function of the number of atoms (c) and lambda (d).

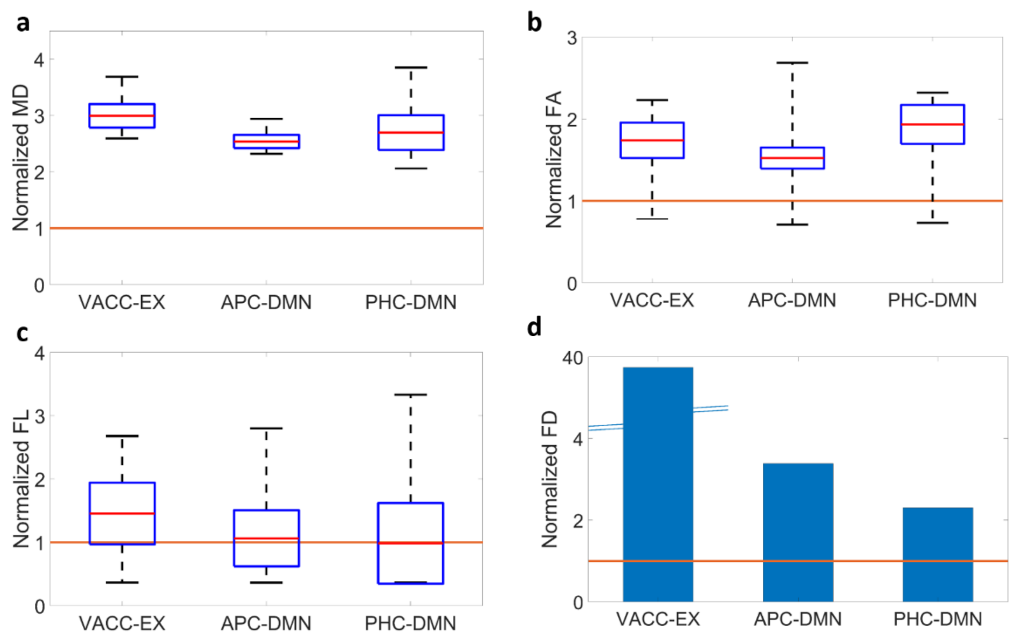

Figure B2: Normalized *MD* (a), *FA* (b), *FL* (c), and *FD* (d) measurements for the fibers intersecting with three anatomical volumes from the reference atlas. The lower and upper whiskers of the boxplots represent the minimum and maximum measurements, respectively. The central red line in each box represents the mean of the measurements, and the box represents one standard deviation from the mean. All measurements were normalized by their respective whole brain averages, represented as the brown line across the three anatomies.

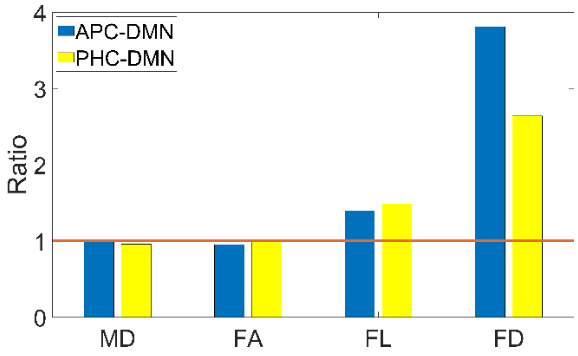

Figure B3: Ratios of the average structural connectivity measures determined for fibers intersecting with the activation volume from the averaged sDL maps that was found within each anatomical region divided by the average measures for fibers intersecting with the corresponding anatomical volume from the reference RSN atlas.

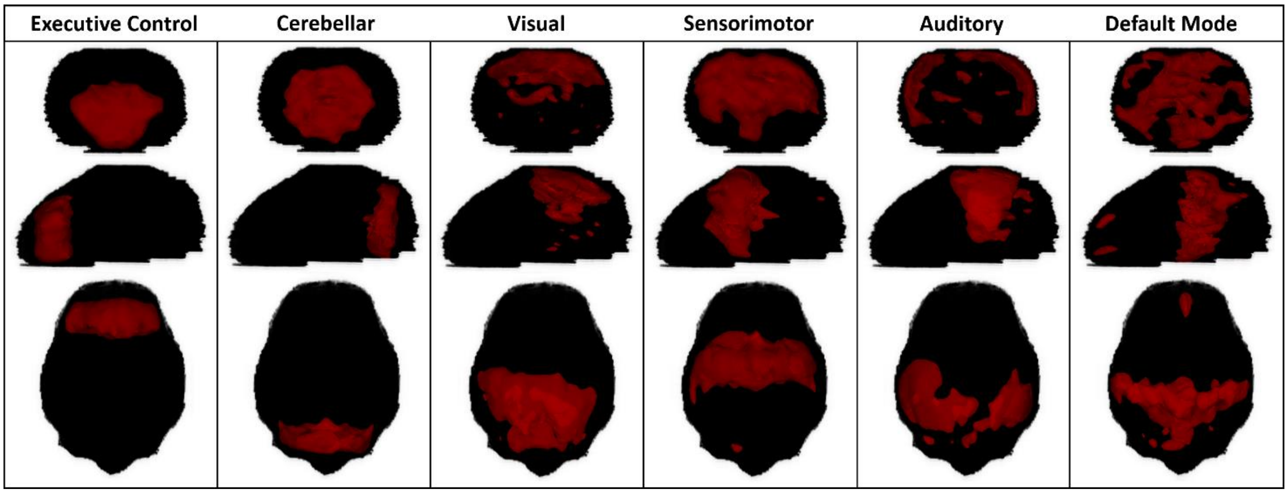

Figure B4: Three-dimensional projections of the averaged sDL activation maps for six RSNs. Coronal (top), sagittal (middle), and axial (bottom) views are projections from the front, left, and top of the brain, respectively.

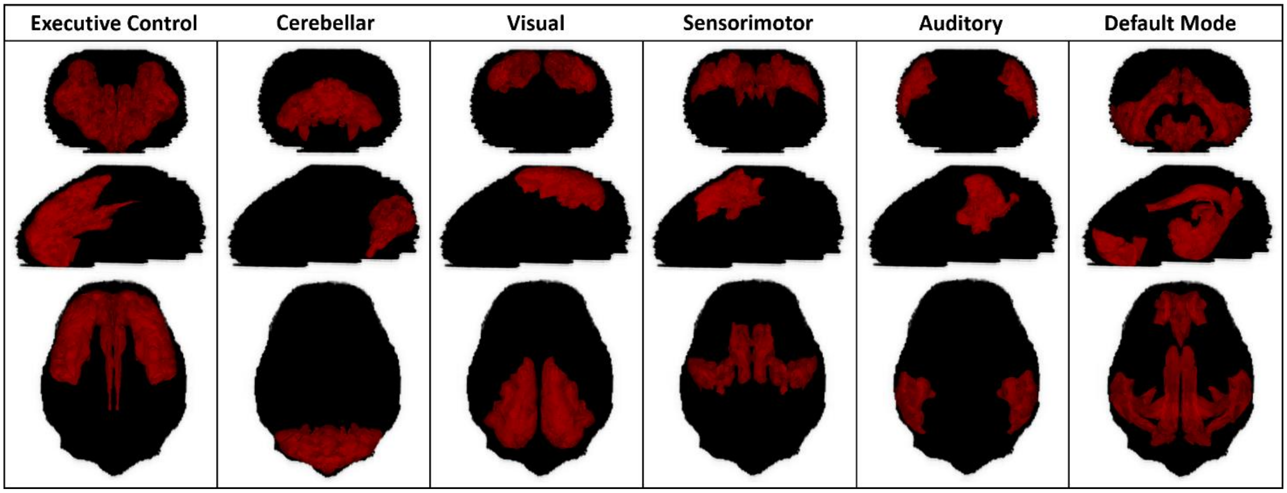

Figure B5: Three-dimensional projections of the pig reference RSN atlas for six RSNs. Coronal (top), sagittal (middle), and axial (bottom) views are projections from the front, left, and top of the brain, respectively.

APPENDIX C

SUPPLEMENTARY MATERIAL – CHPATER 6

Resting-State Default Mode Network Results and Discussion

Individual analysis results

When examining the Pearson spatial correlation coefficients and mean ratios for the activation maps generated from the individual analysis, the traumatic brain injury (TBI) group of pigs did not show statistical difference from the control group for the default mode network (DMN; Table C1 and Figures C1a-2a). When examining the individual anatomical regions within the DMN reference atlas, only the inferior temporal gyrus showed a decreasing trend towards significant difference for the TBI group in comparison to the control group, while all other anatomical regions showed no statistical differences.

Three other anatomical regions (the ventral posterior cingulate, dorsal posterior cingulate, and parahippocampal cortices) were observed to be significantly different or trending towards significant difference based on the p-values associated with the Pearson values; however, these regions did not show statistical differences for the p-values associated with the mean ratios (Table C1). Therefore, they were not considered to be significantly different or trending towards significant difference.

For the control group, which isn't expected to have any major functional connectivity differences and no functional connectivity disruptions caused by TBI, the Pearson values and mean ratios for the DMN as a whole are significantly lower than the values obtained for the visual (VIS), executive control (EX), sensorimotor (SM), and cerebellar (CERE) networks

(Figures C1a-2a and 6.1a-6.3a). Pearson values and mean ratios for the control group's DMN network fall within the ranges of [0.12, 0.21] and [1.7, 2.3], respectively, while the other four networks have values within ranges of [0.32, 0.62] and [3.5, 6.0] for the individual analysis of the control group. The Pearson values for the DMN are below typical values reported in the literature related to resting-state network (RSN) detection [1-4].

Group dual regression analysis results

When examining the Pearson spatial correlation coefficients and mean ratios for the activation maps generated from the group dual regression analysis, the TBI group of pigs again did not show statistical difference from the control group for the default mode network (Table C1 and Figures C1b-2b). However, when examining the individual anatomical regions within the DMN reference atlas, the anterior prefrontal and orbitofrontal cortices showed decreasing trends towards significant differences for the TBI group in comparison to the control group, while the hippocampus and parahippocampal cortex showed increasing trends towards significant difference. The dorsal posterior cingulate cortex was observed to be trending towards significant decrease based on the p-values associated with the Pearson values; however, this region did not show statistical differences for the p-values associated with the mean ratios. Therefore, it was not considered to be significantly different or trending towards significant difference.

Similar to the individual analysis, the Pearson values and mean ratios for the control group obtained using the group dual regression analysis for the DMN as a whole are significantly lower than the values obtained for the VIS, EX, SM, and CERE networks (Figures C1b-2b and 6.1b-6.3b). The Pearson values and mean ratios for the control group's DMN network fall within the ranges of [0.17, 0.25] and [1.8, 2.2], respectively, while the other four networks have values within ranges of [0.37, 0.63] and [3.2, 5.8]. Again, the Pearson values for the DMN are below typical values reported in the literature related to RSN detection.

Discussion

The low Pearson values and mean ratios observed for the DMN, as well as the lack of consistency between the individual and group dual regression analysis methods, suggests that both analysis methods are having difficulties detecting the DMN. Differences between the control group and TBI group were not observed for either method, and although the group dual regression analysis detects differences within more individual anatomical regions of the DMN reference atlas than the individual analysis, it is likely that the network as a whole was not accurately detected for either method, which influences the individual anatomical region results.

There are multiple reasons why detection of the DMN is challenging and may be inaccurate, some of which are discussed in Chapter 5 [4]. One reason relates to the young age of the pigs (4-weeks-old). Studies have demonstrated that there is limited evidence of DMN activity in the human infant brain, whereas children aged 9-12 years and older show more consistent DMN activity [5]. Therefore, the DMN may not have been fully developed in the pigs used in this study. Anesthesia is also another confounding factor, as many anesthetic agents are known to interfere with neural activity and neurovascular coupling [6, 7]. Recently, isoflurane specifically has been shown to cause reduced functional connectivity in the DMN in humans [8], and therefore, the use of isoflurane in this study may have caused reduced DMN activity. Another issue arises in the creation of the pig reference DMN functional connectivity atlas using a preexisting standard pig brain atlas. In humans, only the medial area of the anterior prefrontal cortex is associated with the DMN [9]; however, the standard pig brain atlas [10] does not segment the anterior prefrontal cortex into smaller sub-cortical regions. Therefore, a perfectly accurate atlas is unable to be created, and this imperfect reference atlas is used in the analysis when attempting to detect the DMN.

Mean Ratio Boxplots

The boxplots associated with the calculated mean ratios for the individual and group dual regression analysis methods for the VIS, EX, SM, and CERE networks are presented in Figures C3-5.

References

1. Brookes, M.J., et al., *Investigating the electrophysiological basis of resting state networks using magnetoencephalography.* Proceedings of the National Academy of Sciences, 2011: p. 201112685.
2. Smith, S.M., et al., *Correspondence of the brain's functional architecture during activation and rest.* Proceedings of the National Academy of Sciences, 2009. **106**(31): p. 13040-13045.
3. Lois, G., J. Linke, and M. Wessa, *Altered functional connectivity between emotional and cognitive resting state networks in euthymic bipolar I disorder patients.* PLoS One, 2014. **9**(10): p. e107829.
4. Simchick, G., et al., *Pig Brains Have Homologous Resting State Networks with Human Brains.* Brain connectivity, 2019(ja).
5. Broyd, S.J., et al., *Default-mode brain dysfunction in mental disorders: a systematic review.* Neuroscience & biobehavioral reviews, 2009. **33**(3): p. 279-296.
6. Hamilton, C., Y. Ma, and N. Zhang, *Global reduction of information exchange during anesthetic-induced unconsciousness.* Brain Structure and Function, 2017. **222**(7): p. 3205-3216.
7. Liang, Z., J. King, and N. Zhang, *Intrinsic organization of the anesthetized brain.* Journal of Neuroscience, 2012. **32**(30): p. 10183-10191.
8. Kawaguchi, N., et al., *Effects of Isoflurane on Brain Functional Connectivity in Common Marmosets.* In Proceedings of the 27th Annual Meeting of ISMRM, Montreal, Canada, 2019.
9. Buckner, R.L., J.R. Andrews-Hanna, and D.L. Schacter, *The brain's default network.* Annals of the New York Academy of Sciences, 2008. **1124**(1): p. 1-38.
10. Saikali, S., et al., *A three-dimensional digital segmented and deformable brain atlas of the domestic pig.* Journal of neuroscience methods, 2010. **192**(1): p. 102-109.

Table C1

Networks and Anatomical Regions	Individual			Group Dual Regression		
	Sig	**Pearson**	**Mean Ratio**	**Sig**	**Pearson**	**Mean Ratio**
Default Mode	-	0.567	0.444	-	0.608	0.880
Hippocampus	-	0.761	0.603	#	0.203$^{\#}$	0.162$^{\#}$
Anterior Prefrontal Cortex	-	0.659	0.489	#	0.322$^{\#}$	0.338$^{\#}$
Orbitofrontal Cortex	-	0.736	0.534	#	0.272$^{\#}$	0.282$^{\#}$
Inferior Temporal Gyrus	#	0.322$^{\#}$	0.141$^{\#}$	-	0.556	0.568
Ventral Posterior Cingulate Cortex	-	0.273$^{\#}$	0.920	-	0.860	0.856
Dorsal Posterior Cingulate Cortex	-	0.015*	0.413	-	0.398$^{\#}$	0.647
Retrosplenial Cingular Cortex	-	0.753	0.663	-	0.929	0.967
Anterior Entorhinal Cortex	-	0.636	0.705	-	0.507	0.443
Parahippocampal Cortex	-	0.327$^{\#}$	0.804	#	0.200$^{\#}$	0.196$^{\#}$

P-values comparing the Pearson spatial correlation coefficients and mean ratios of the control group and the TBI group for the default mode network and each individual anatomical region. The groups were considered significantly different if $p<0.05$ (denoted by *), and they were considered to be trending towards significant difference if $p<0.4$ (denoted by #). A network or anatomical region was only considered significantly different or trending towards significant difference if the p-values for both the Pearson values and mean ratios were below the specified thresholds (‘Sig’ columns).

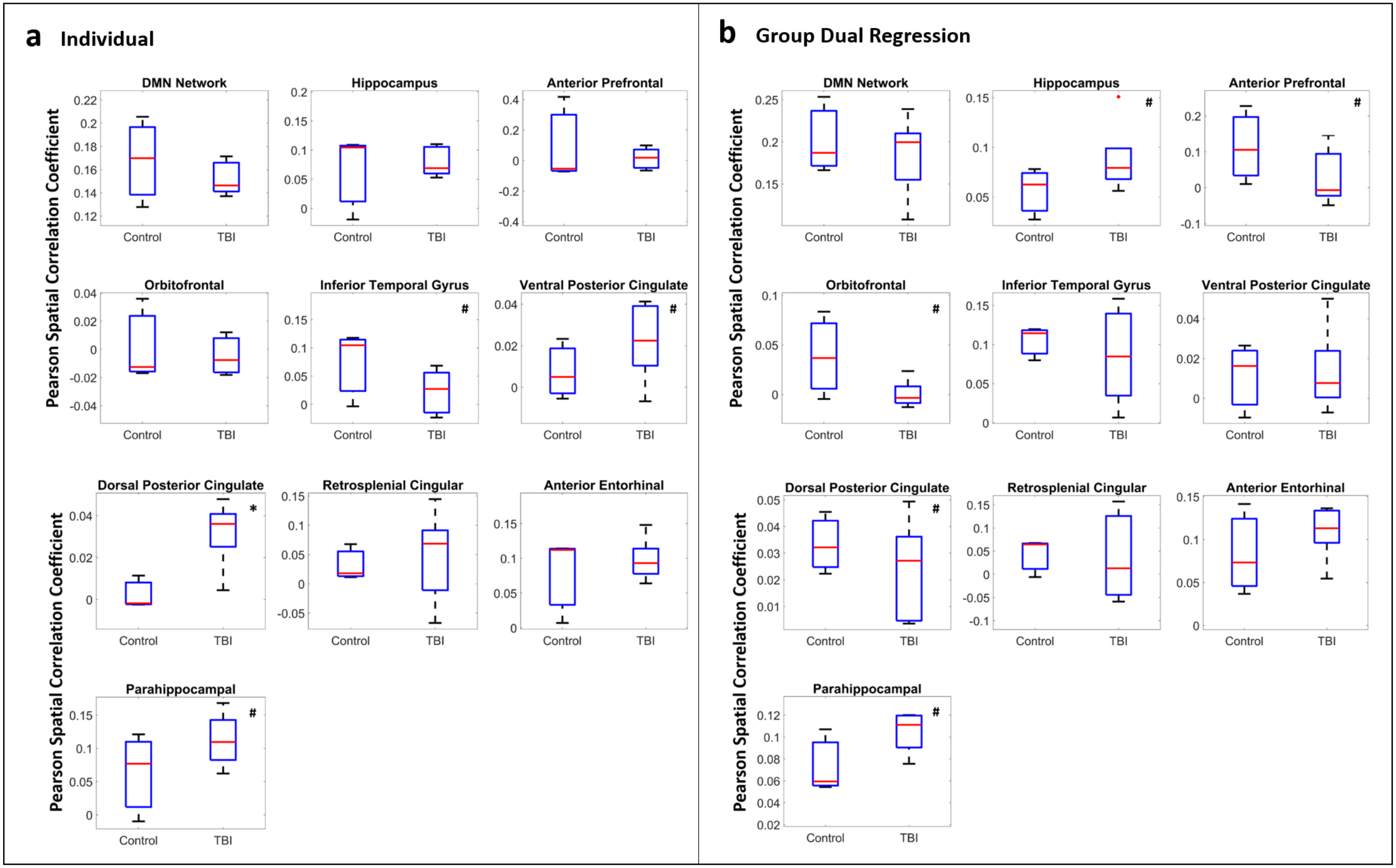

Figure C1: Boxplots of the Pearson spatial correlation coefficients for the default mode (DMN) network and its individual anatomical regions obtained using individual analysis (a) and group dual regression analysis (b). An asterisk (*) in the upper right-hand corner indicates significant differences ($p<0.05$) between the control group and TBI group, and a number sign (#) indicates the groups are trending towards significant differences ($p<0.4$).

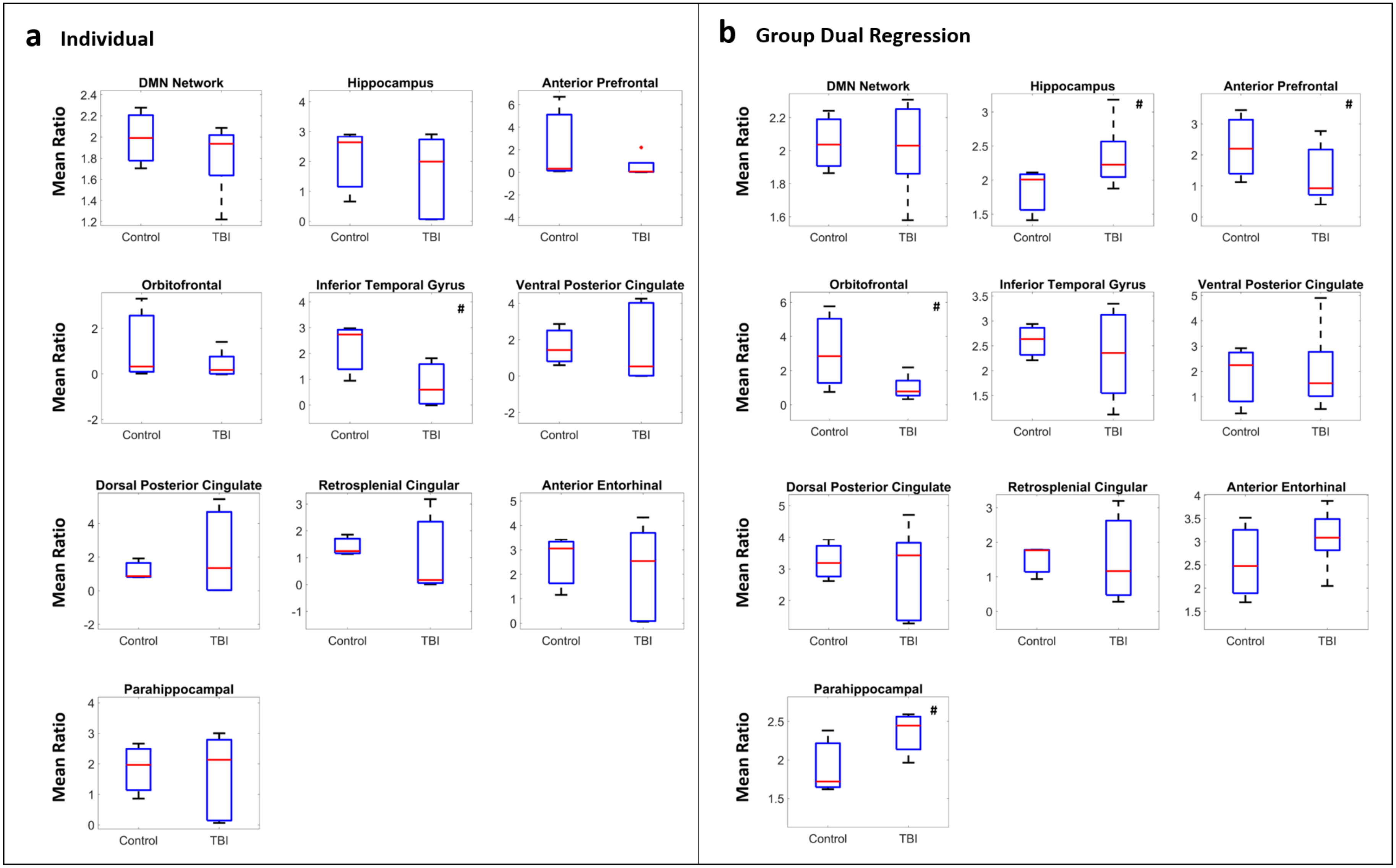

Figure C2: Boxplots of the mean ratios for the default mode (DMN) network and its individual anatomical regions obtained using individual analysis (a) and group dual regression analysis (b). An asterisk (*) in the upper right-hand corner indicates significant differences ($p<0.05$) between the control group and TBI group, and a number sign (#) indicates the groups are trending towards significant differences ($p<0.4$).

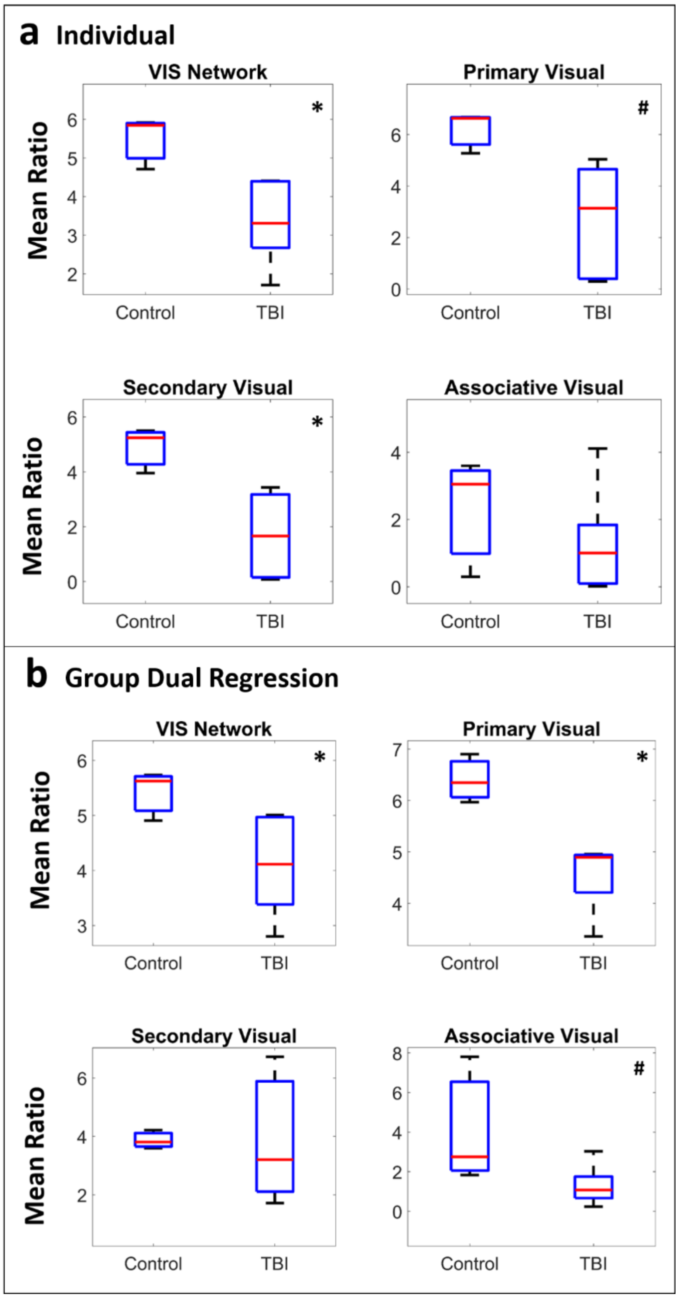

Figure C3: Boxplots of the mean ratios for the visual (VIS) network and its individual anatomical regions obtained using individual analysis (a) and group dual regression analysis (b). An asterisk (*) in the upper right-hand corner indicates significant differences ($p<0.05$) between the control group and TBI group, and a number sign (#) indicates the groups are trending towards significant differences ($p<0.4$).

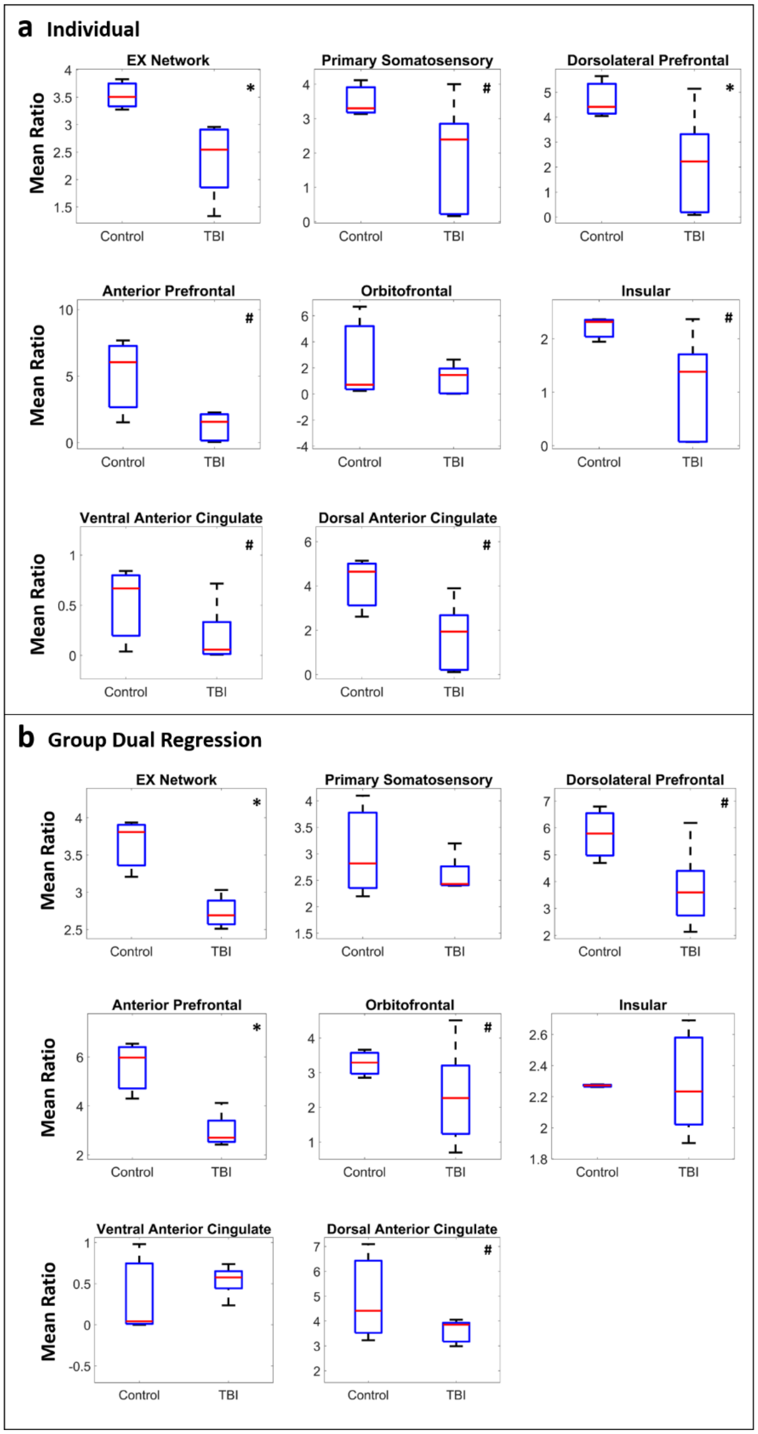

Figure C4: Boxplots of the mean ratios for the executive control (EX) network and its individual anatomical regions obtained using individual analysis (a) and group dual regression analysis (b). An asterisk (*) in the upper right-hand corner indicates significant differences ($p<0.05$) between the control group and TBI group, and a number sign (#) indicates the groups are trending towards significant differences ($p<0.4$).

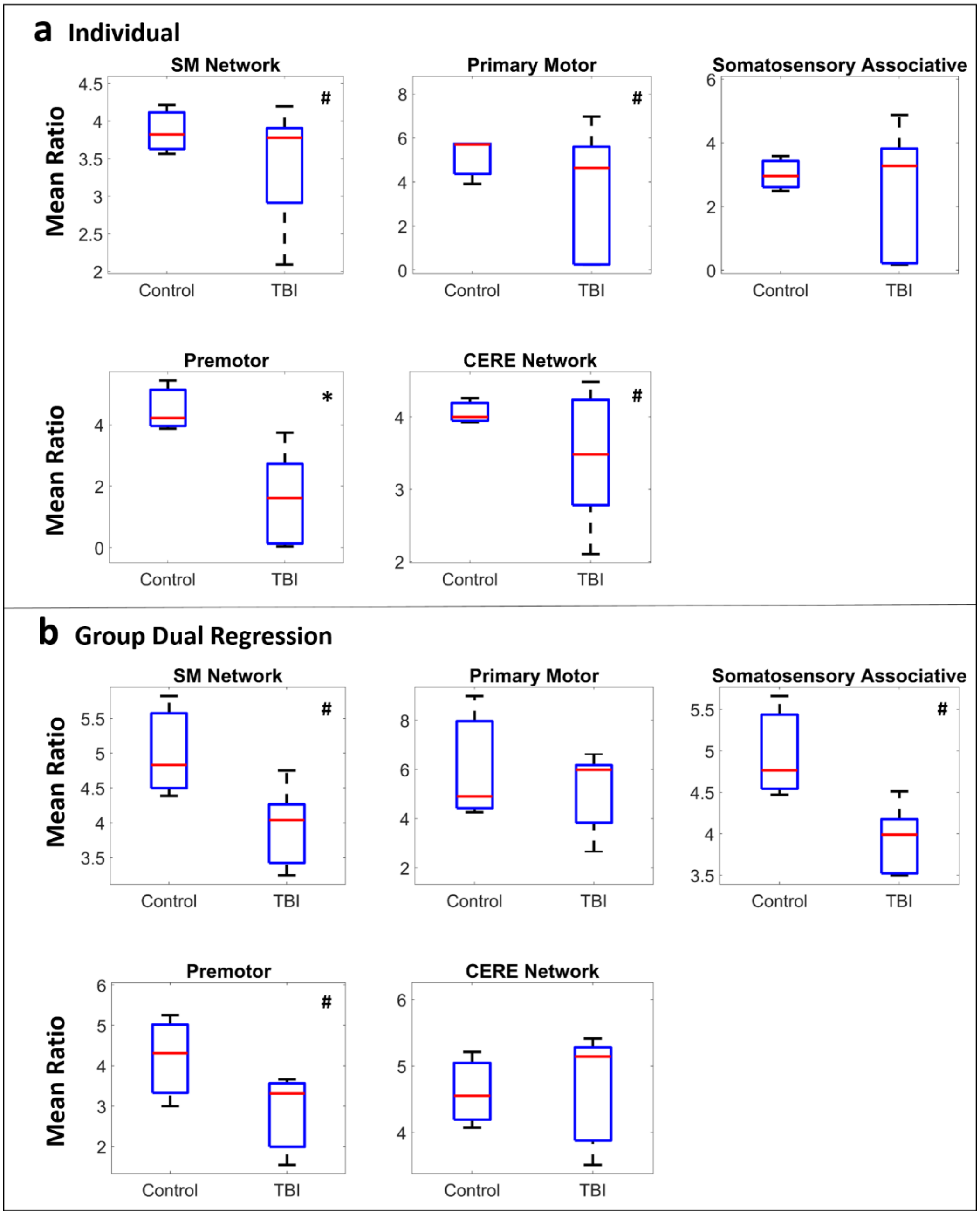

Figure C5: Boxplots of the mean ratios for the sensorimotor (SM) network and its individual anatomical regions, as well as the cerebellar (CERE) network, obtained using individual analysis (a) and group dual regression analysis (b). An asterisk (*) in the upper right-hand corner indicates significant differences ($p<0.05$) between the control group and TBI group, and a number sign (#) indicates the groups are trending towards significant differences ($p<0.4$).